Prediction of Particle Sizes of Gas-Atomized Metal Powders

Dissertation zur Erlangung des akademischen Grades

(Dissertation to achieve the academic degree)

„Doktor der montanistischen Wissenschaften“

vorgelegt von (submitted by):

Martin Dopler

Betreuer/in (Advisor): Ao.Univ.-Prof.DI.Dr.techn. Christian Weiß

Lehrstuhl/Institut (Chair/Institute): Process Technology and Industrial Environmental Protection

EIDESSTATTLICHE ERKLÄRUNG

Ich erkläre an Eides statt, dass ich die vorliegende Arbeit selbständig und ohne fremde Hilfe verfasst, andere als die angegebenen Quellen und Hilfsmittel nicht benutzt und die den benutzten Quellen wörtlich und inhaltlich entnommenen Stellen als solche erkenntlich gemacht habe.

AFFIDAVIT

I declare in lieu of oath, that I wrote this thesis and performed the associated research myself, using only literature cited in this volume.

_____

Martin Dopler, 31st of May 2017, Leoben

Foreword

After having worked in process development of metal powder production for more than 15 years, I took my 2nd attempt to write a Ph.D. thesis at The Chair of Process Technology and Industrial Environmental Protection at University of Leoben. As a completion to my practical knowledge (and also in order not to disclose any company data), this work is a theoretical overview of the phenomena around gas atomization of melts. The practical use for the reader of this work lies in the possibility to predict the influence of process parameters on particle sizes and – to a certain extent – also on particle shape.

I started this work from a personally difficult situation, and I want to express my sincere gratitude to Prof. Christian Weiss for his scientific and moral support.

I also wish to thank Prof. Bruno Buchmayr for further suggestions, Prof. Josef Draxler for the computational code to calculate spheroidisation and for not stopping to encourage me to finish this work, and to Prof. Markus Lehner and the whole staff at the Chair of Process Technology for the warm reception and support of any kind. Finally, I wish to thank my family for encouraging me and for tolerating my moods in times of poor progress.

Liquid Atomisation is an exciting and versatile field of investigation!

Abstract

This thesis presents a mathematical model to estimate results of the metal powder production process via gas atomization.

The melt breakup process is divided into several steps: Primary breakup (sheet or jet breakup) is described by Linear Stability Analysis with the aim to identify the parameters governing the liquid disintegration process. Apart from gas velocity and melt throughput, these are mainly process parameters such as gas and melt temperatures, gas pressure as well as gas and melt properties.

Primary breakup is followed by ligament and primary droplet formation. The possibility of a further breakup into secondary droplets can be estimated by model equations expressing the characteristic times of particle formation – secondary breakup time and spheroidization time compete with acceleration time (relative velocity decay), cooling/solidification time and oxidation time. Fast solidification and oxidation of the particles lower the probability of producing a fine, spherical product.

For evaluation, the model equations are applied to three commonly used gas atomization systems: free fall (or open jet), prefilming and confined direct nozzle. In the first case, melt iron is atomized by hot air, for the other two examples, aluminium was chosen to be atomized by cold air and helium. Calculations are compared to atomization trials published by several authors.

Despite the limitations of the model (oxidation is not included, only the axial decline of the gas velocity field at the nozzle exit is considered neglecting two-dimensional effects), the calculations are in good agreement with the atomization results, while the deviations can be well explained.

Kurzfassung

Ziel dieser Arbeit ist die Entwicklung eines mathematischen Modells zur Vorhersage der Pulvereigenschaften bei der gasgestützten Zerstäubung von Metallschmelze.

Der Flüssigkeitszerfall kann in folgende Schritte unterteilt werden: Der Primärzerfall (Film- oder Strahlzerfall) wird anhand der linearen Stabilitätsanalyse beschrieben mit dem Ziel, die den Zerfall dominierenden Parameter zu herauszuarbeiten. Insbesondere sind dies – abgesehen von Gasgeschwindigkeit und Schmelzedurchsatz – Prozessparameter wie Gasdruck und -temperatur bzw. Schmelzetemperatur sowie die physikalischen Eigenschaften von Gas und Flüssigkeit.

Die aus dem Primärzerfall resultierenden Ligamente zerfallen zu sogenannten Primärtropfen. Die Wahrscheinlichkeit eines weiteren Zerfalls zu Sekundärtropfen kann im vorliegenden Modell anhand von Gleichungen abgeschätzt werden, mit denen die für die verschiedenen Vorgänge charakteristischen Zeiten berechnet werden: Zerfallszeit, Sphäroidisierungszeit, „Beschleunigungszeit“ (die Abnahme der Relativgeschwindigkeit zwischen Gas und Tropfen), Abkühl- bzw. Erstarrungszeit bzw. Oxidationszeit. Rasche Erstarrung und Oxidation verringern die Wahrscheinlichkeit, ein feines und sphärisches Pulver zu erhalten.

Zur Evaluierung wurde das Modell auf die drei üblichen Gaszerstäubungssysteme – Freifalldüse, Prefilming-Düse und Direkt-Confined Düse – angewendet. Im ersten Berechnungsfall wurde Eisenschmelze mit heißer Luft zerstäubt, in den beiden anderen Fällen wurde Aluminiumschmelze mit kalter Luft bzw. Helium zerstäubt. Die Berechnungen wurden mit den Zerstäubungsergebnissen bekannter Literaturstellen verglichen.

Trotz der Einschränkungen des Modells (der Einfluss der Oxidation wurde nicht berücksichtigt, außerdem wurde lediglich der Abfall der axialen Gasgeschwindigkeitskomponente in die Berechnungen miteinbezogen) stimmen die Berechnungen gut mit der Praxis überein bzw. konnten die Abweichungen gut beschrieben werden.

Table of Contents

List of Symbols

Arabic Symbols

a (0°C)	[m/s]	gas sonic velocity at reference conditions (0°C, 1 bar abs)
a(T)	[m/s]	gas sonic velocity
A*	[m^2]	narrowest cross section
a*	[m/s]	sonic velocity in the narrowest cross section
a_0	[m/s]	sonic velocity (reservoir gas)
a_1	[m/s]	sonic velocity at ambient conditions
A_{cone}	[m^2]	cone surface area
A_{drop}	[m^2]	melt droplet surface area
A_{jet}	[m^2]	melt jet surface area
A_{nozzle}	[mm^2]	gas cross section
$c_{D,L}$	[-]	drag coefficient
$c_{p,gas}$	[J/kgK]	specific heat enthalpy of the gas at constant pressure
$c_{p,melt}$	[J/kgK]	specific heat enthalpy of the metal in melt state
$c_{p,sol}$	[J/kgK]	specific heat enthalpy of the metal in solid state
d	[mm]	melt nozzle diameter, inner diameter
D	[mm]	gas nozzle diameter, outer diameter
d_{32}	[µm]	sauter mean diameter
D_{cone}	[mm]	diameter of the melt cone at breakup
d, d_{drop}, d_{50}	[µm]	droplet diameter
D_L	[µm]	ligament diameter
$d_{prim,res}$	[µm]	residueing primary droplet diameter
d_{sec}	[µm]	resulting droplet diameter
$d_{sec,bag}$	[µm]	secondary droplet diameter due to bag breakup
$d_{sec,shear}$	[µm]	secondary droplet diameter due to shear breakup
e_{gas}	[J/kg]	energy needed for isothermic compression of the gas
e_{powder}	[J/kg]	surface energy of the powder
GLR	[kg_{gas}/kg_{melt}]	gas-to-liquid ratio
h_F	[mm]	half sheet thickness
h_{Fmean}	[mm]	mean half sheet thickness
k_{max}	[1/m]	maximum wave number
l_L	[µm]	length of the ligament
Ma_{Koria}	[-]	maximum Mach number following Koria's calculations
Ma_{max}	[-]	maximum Mach number
m_{drop}	[kg]	melt droplet mass
m'_{gas}	[kg/h]	gas consumption
m'_{melt}	[kg/h]	melt production rate
m_{Mol}	[g/mol]	molecular weight

p^*	[bar]	pressure in the narrowest cross section
p^*	[bar abs]	critical pressure
p_0	[bar, bar abs]	gas reservoir pressure
$p_{0,crit}$	[bar]	minimum pressure to achieve critical conditions
p_1	[bar, bar abs]	ambient pressure
p_{gas}	[bar]	operating gas pressure
$p_{gas,abs}$	[bar abs]	absolute gas pressure
Q	[W]	heat (radiated or convected)
Q_{BB}	[%]	bag breakup percentage
Q_{SB}	[%]	shear breakup percentage
Re_L	[µm]	Reynolds number of ligament
$R_{m,gas}$	[J/kgK]	specific gas constant
S	[K]	Sutherland constant
S_m	[m^2/kg]	specific surface area
T^*	[°C]	critical temperature
T_0	[K]	Sutherland reference temperature
T_0	[°C]	gas reservoir temperature
T_1	[°C]	ambient temperature
t_{cool}	[µs]	cooling time of the melt droplet
T_{drop}	[°C]	droplet temperature
T_{evap}	[°C]	evaporation point of the melt
T_{gas}	[K]	operating gas temperature
t_{lig}	[µs]	ligament breakup time
T_{melt}	[K]	melt temperature
ΔT_{melt}	[°C]	melt temperature loss
t_{secBU}	[µs]	breakup time of the droplet
t_{sheet}	[µs]	sheet breakup time
T_{sol}	[K]	solidification temperature of the metal
t_{sol}	[µs]	solidification of the droplet
t_{sph}	[µs]	spheroidisation time of the droplet
$t_{sph,Rao}$	[µs]	spheroidisation time of the droplet following the model of Rao
$t_{We>1}$	[µs]	time the droplet Weber number is larger than 1
$t_{We>16}$	[µs]	time the droplet Weber number is larger than 16
v^*	[m/s]	gas velocity in the narrowest cross section
$v_{cone-gas}$	[m/s]	relative velocity between melt cone and gas
v_{gas}	[m/s]	gas velocity
V'_{gas}	[m^3/h]	gas volume flow
v_{jet}	[m/s]	melt jet velocity
$v_{lig-gas}$	[m/s]	relative velocity between ligament and gas
V'_{melt}	[m^3/h]	melt volume flow
v_{rel}	[m/s]	relative velocity
v_{sheet}	[m/s]	sheet velocity
x	[mm]	distance from gas nozzle exit
x_{BU}	[mm]	breakup length of the jet or cone

Greek symbols

α_{lig}, α_{jet}, α_{cone}	[W/m^{2}K]	heat transfer coefficient of the ligament, jet, cone
Δh_{fus}	[kJ/kg]	enthalpy of fustion
Δh_{gas}	[J/kg]	energy needed for heating the gas to operating temperature
Δh_{melt}	[J/kg]	energy needed for melting and heating melt to operating temperature
α, β	[°]	gas inclination angles
ε	[-]	emissivity
η_0	[kg/ms]	dynamic viscosity of the gas at reference temperature
η_{gas}	[kg/ms]	actual dynamic viscosity of the gas
$\eta_{gas,1}$	[kg/ms]	dynamic viscosity of the ambient gas
η_{melt}	[Pas]	dynamic viscosity of the melt
κ	[-]	ratio of specific heats
λ_{gas}	[W/mK]	thermal conductivity of the gas
$\lambda_{gas,1}$	[W/mK]	conductivity of the ambient gas
λ_{max}	[µm]	maximum wave length
λ_{melt}	[W/mK]	thermal conductivity of the metal in molten state
λ_{solid}	[W/mK]	thermal conductivity of the metal in solid state
ν_{gas}	[m^2/s]	kinematic viscosity of the gas
ν_{melt}	[m^2/s]	kinematic viscosity of the melt
ρ^*	[kg/m^3]	critical density
ρ_0	[kg/m^3]	gas reservoir density
ρ_1	[kg/m^3]	ambient gas density
ρ_{gas} (0°,1bar)	[kg/m^3]	gas density at reference conditions (0°C, 1 bar abs)
ρ_{gas}(p,T)	[kg/m^3]	actual gas density
ρ_{melt}	[kg/m^3]	density of the metal in molten state
ρ_{solid}	[kg/m^3]	density of the metal in solid state
σ	[N/m]	surface tension ot the melt
σ_B	[W/m^{2}K^4]	Stefan-Boltzmann constant
ω_{max}	[1/s]	maximum growth rate

nondimensional numbers

Mach number	$Ma = \frac{gas\ velocity}{sonic\ velocity} = \frac{v_{gas}}{a}$
Prandtl number	$Pr = \frac{viscous\ diffusion\ rate}{thermal\ diffusion\ rate} = \frac{\eta_{gas} c_{p,gas}}{\lambda_{gas}}$
droplet Weber number	$We_{drop} = \frac{droplet\ kinetic\ energy}{droplet\ surface\ energy} = \frac{\rho_{gas} d_{drop} v_{rel}^2}{\sigma}$
sheet Weber number	$We_{sheet} = \frac{sheet\ kinetic\ energy}{sheet\ surface\ energy} = \frac{\rho_{gas} h_F v_{rel}^2}{2\sigma}$
jet (cone, ligament, droplet) Reynolds number	$Re_{jet} = \frac{jet\ (\dots)\ kinetic\ energy}{jet\ (\dots)\ viscous\ energy} = \frac{\rho_{gas} d_{jet} v_{jet}}{\eta_{gas}}$
Nusselt number	$Nu = \frac{heat\ transfer\ due\ to\ convection}{heat\ transfer\ due\ to\ conduction} = \frac{\alpha d}{\lambda_{gas}}$

1. Introduction

1.1. Contemporary Challenges in Metal Powder Production

The production of metal powders is a conservative business. Compared to the production lines of a car factory or in electronics industries, metal powders are produced in a dirty, dusty, hot and somehow stone-age environment. Most of the powder production plants via gas atomization are based on processes invented during the first two decades of the 20th century.

Figure 1.1: Titanium parts manufactured by 3D printing methods (© Dominik Hammerer)

There are several reasons for this fact:

- ⇨ On the one hand, capital costs for powder production plants are high (several millions of Euros), so the will to take risks is low.
- ⇨ At the same time, new powder production plants are built with the will to satisfy the urgent needs of specific customers requiring specific product properties, so the available time for industrial research and development in this field is short.
- ⇨ Finally, the requirements on metal powders are tricky to achieve – any change in the "history" of the particles produced results in a change of powder properties (not only particle size distribution, but flowability, reactivity, pressing and sintering behaviour, etc.). Hence, powder producers hesitate to change processes, because the impacts on the customers (who are used to the "old" powder production processes), are unclear.

With the beginning of the 21st century, new manufacturing processes related to powder metallurgy (which are embraced by the term "additive manufacturing") have become ready for production.

Due to the nature of these processes, also the requirements on the powders in use have become higher with regards to particle size distribution, shape, purity and oxygen content. On the one hand, these properties rely on their production conditions related to gas atomization which are: melt and gas temperature, gas-to-liquid ratio, oxygen concentration, humidity, etc. On the other hand, also the post-processing steps are important – screening and classifying, homogenization (e.g. of several batches), passivation, filling. Even transport (segregation) and storage (atmosphere, humidity, etc.) can be important.

Hence, for powder producers it is indispensable to understand the influences of the production conditions on product properties.

Table 1.1: Development of Powder Metallurgy; taken from [KLA1984]

Date	Development	Origin
3000 B.C.	"Sponge iron" for making tools	Egypt, Africa, India
1200	Cementing platinum grains	South America (Incas)
1781	Fusible platinum-arsenic alloy	France, Germany
1790	Production of platinum-arsenic chemical vessels commercially	France
1822	Platinum powder formed into solid ingot	France
1826	High-temperature sintering of platinum powder compacts on a commercial basis	Russia
1829	Wollaston method of producing compact platinum fromplatinum sponge (basis of modern P/Mtechnique)	England
1830	Sintering compacts of various metals	Europe
1859	Platinum fusion process	
1870	Patent for bearing materials made from metal powders (forerunner of self-lubricating bearings)	United States
1878-1900	Incandescent lamp filaments	United States
1915-1930	Cemented carbides	Germany
Early 1900's	Composite metals	United States
Early 1900's	Porous metals and metallic filters	United States
1920's	Self-lubricating bearings (used commercially)	United States
1940's	Iron powder technology	Central Europe
1950's and 1960's	P/Mwrought and dispersion-strengthened products, including P/Mforgings	United States
1970's	Hot isostatic pressing, P/Mtool steels, and superplastic superalloys	United States
1980's	Rapid solidification and injection molding technology	United States
1994	Direct metal laser sintering (DMLS) process presented (EOS)	Germany
2006	Laser Sinterung of Titanium and Aluminium	Germany

1.2. Introduction to Gas Atomization Processes

Gas atomization is a widely used technique for the production of metal powders. The (metal) melt is brought into contact with a pressurized gas expanding at high velocities and – due to interfacial forces between the two fluids – the liquid metal is divided into small parts (ligaments, droplets) which then solidify – metal powder!

The documented history of gas atomization goes back to the year 1873, when William Marriott disclosed a patent entitled "Improvements in the manufacture of salts and oxides of lead, and in apparatus therefor" [MAR1873]: A dropping stream of liquid lead is atomized by a gas mixture to produce e.g. a plate of lead oxide (figure 1.2).

Since then, a vast number of gas atomization methods has been invented of which the most frequently used are:

- ⇨ Open (free) jet atomization
- ⇨ Confined (“close-coupled”) atomization
- ⇨ Back pressure atomization

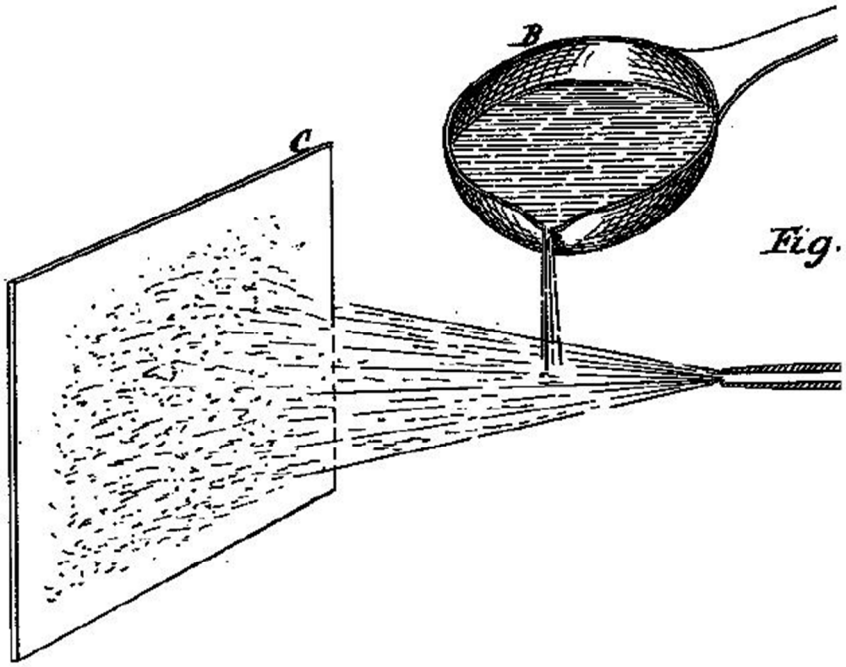

Figure 1.2: Atomization of lead, patent filed in 1873 [MAR1873]

1.2.1. Open (Free) Jet Atomization

Free jet atomizers are easy to build and operate, as there is no direct contact between the hot melt nozzle and the mostly cold gas nozzles (figure 1.3a). Hence, freezing or thermal stresses are no issue for plant operation. The contact between gas and liquid is moderate and unforced, so the efficiency is low and the powders are comparatively coarse. Despite the bad energy conversion, many atomizers are still built in that manner, as the advantages are evident. To increase primary surface, some attempts have been made to convert the melt jet into a sheet and by this means improve atomizer performance (figure 1.3b-d).

1.2.2. Confined ("Close-Coupled") Atomization

To improve energy conversion, "direct" and "prefilming" atomizers were invented at the beginning of the 20th century (figure 1.4). Those two systems are usually referred to as "close-coupled nozzles". Due to the forced contact between the two fluids (building a "closed couple"), energy conversion is better. As the gas is commonly colder than the solidification temperature of the melt, freezing at the nozzle tip cause operating issues.

1.2.3. Back Pressure Atomization, Internal Mixing Atomization

To intensify contact between gas and liquid, back pressure and internal mixing atomizers (figure 1.5) started being used for spraying applications some 50 years ago. Back pressure leads to a higher interfacial pressure between gas and liquid [DOP2008] and therefor increases atomizer

performance. Due to engineering and operating problems such as nozzle freezing or liquid throughput control, only a few metal melt atomizers are operated with internal mixing nozzles [YUL1994].

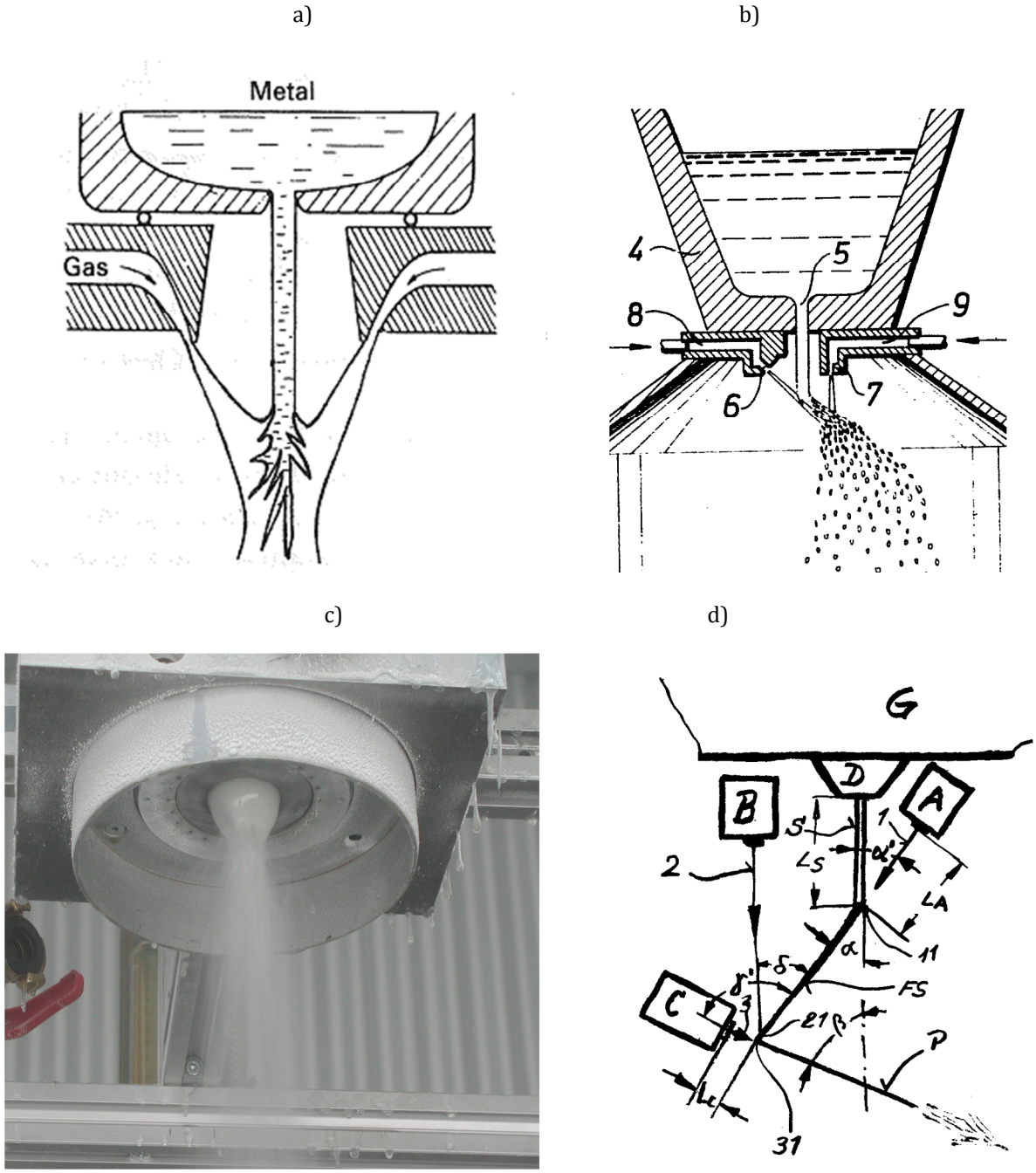

Figure 1.3: a) open jet atomization [KLA1984]; b) asymmetric atomization of steel [HEL1970]; c) open sheet atomization of corn syrup [STE2004]; d) 3-stage open sheet atomization [TOR2000]

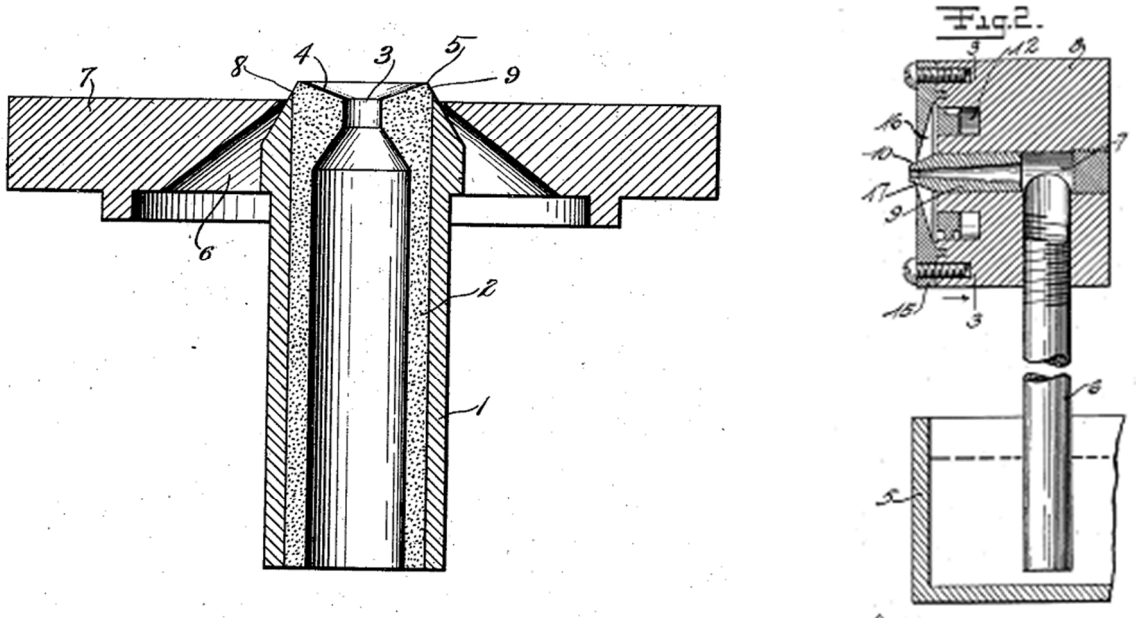

Figure 1.4: Confined nozzles: Prefilming nozzle (left picture) [HAL1919] and "direct" confined nozzle (right) [HAL1917]: the rotating and circumferential gas stream creates a pressure field such that the liquid is aspirated vertically upwards into the nozzle

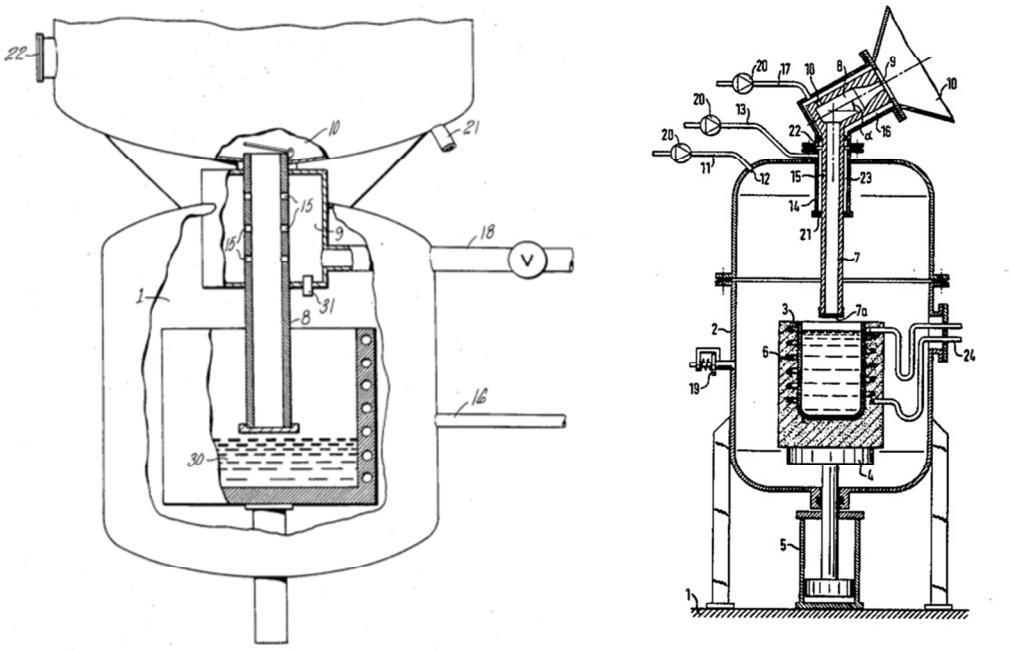

Figure 1.5: Internal mixing atomization presented by Basczcuk [BAS1989] (left picture) and Wentzell [WEN1984] (right picture): increasing the pressure in the vessel leads to a higher melt throughput

1.2.4. Other Industrial Atomization Methods (Examples)

For specific industrial applications, various atomization methods have been developed, for which we give some important examples

- ⇨ Centrifugal Atomization (figure 1.6, left picture): the melt is poured on a rapidly rotating disk and develops into a thin film which disintegrates into ligaments and droplets as soon as it reaches the edge of the disk. If necessary, gas jets are applied on the particles to guarantee cooling and solidification. In an alternative application of this principle, a rotating electrode is melt by a heat source (electric arc or plasma), and the layer of liquid melt is also disintegrated by centrifugal forces (figure 1.6, right picture)

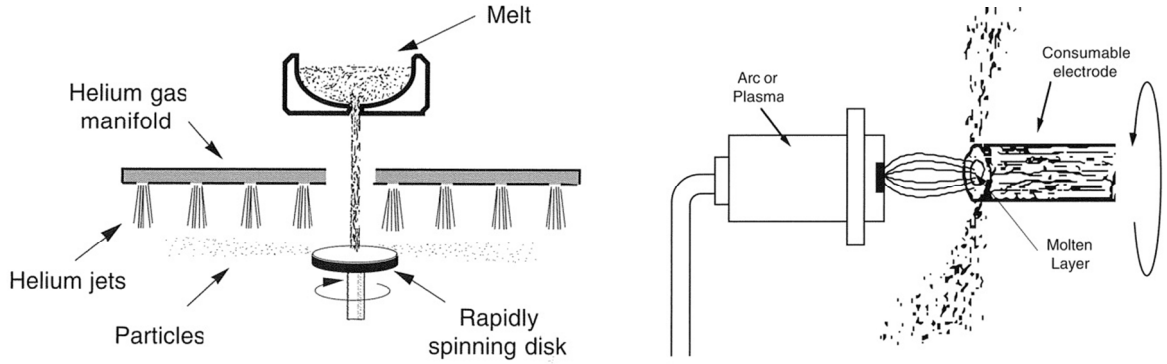

Figure 1.6: Centrifugal atomization (left picture) and rotating electrode atomization (right picture), taken from [LAW1992]

- ⇨ Plasma atomization technology (figure 1.7, left picture): a metal wire (e.g. from titanium) is fed into the system and disintegrated by a number of plasma torches producing very pure and spherical powder [APC2015]
- ⇨ Spray forming processes (e.g. Osprey process): spray forming uses the effect of rapid solidification of the atomization process to produce parts with elevated mechanical properties due to their microstructure – the atomized particles are deposited upon a suitable collecting surface, for example on a rotating tube as shown in figure 1.7, right picture [BRO1990]

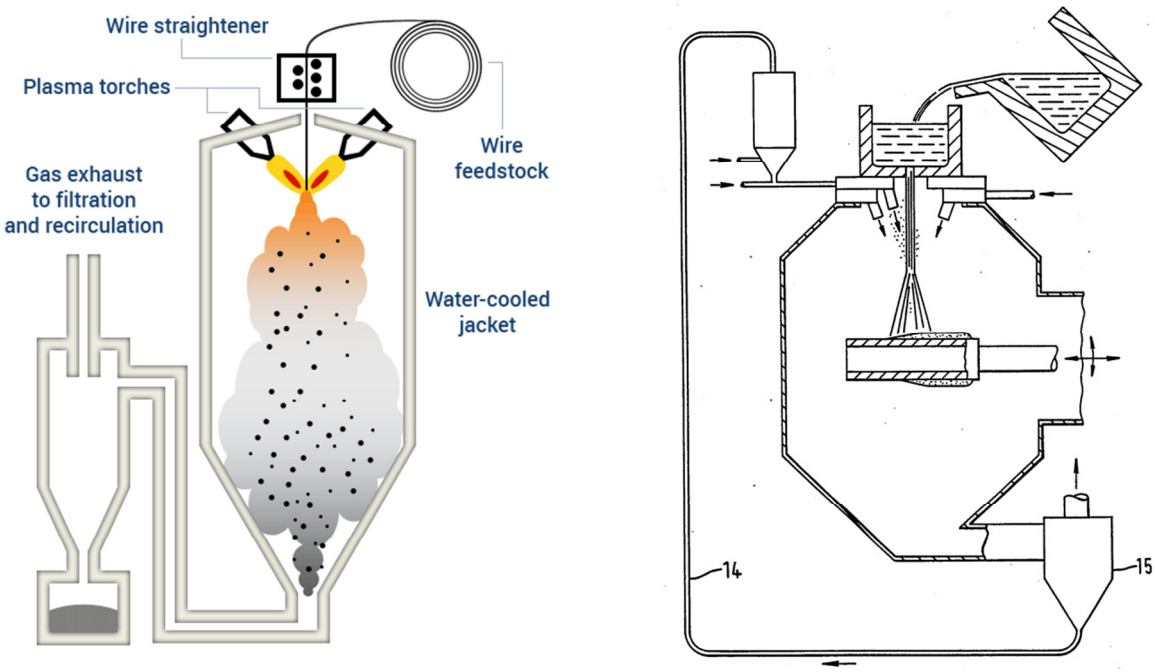

Figure 1.7: Plasma atomization of titanium wire [APC2015] (left picture) and spray deposition process ("Osprey Process") [BRO1990] (right picture)

1.3. Energy Efficiency in Melt Atomization

Independent on which atomization concept is used, we have to accept that the energy efficiency of gas atomization processes is low:

Usually, the energy needed to produce fine particles is seen to be the surface energy created by the process:

$$e_{powder} = \sigma S_m \tag{1.1}$$

In practice, we consume energy to pressurize the gas to atomization pressure, to heat the gas to atomization temperature and to heat and melt the liquid metal:

$$e_{gas} = R_{m,gas} T_1 ln\left(\frac{p_{gas}}{p_1}\right) \tag{1.2}$$

$$\Delta h_{gas} = \int_{T_1}^{T_{gas}} c_{p,gas}(T,p)dT \tag{1.3}$$

$$\Delta h_{melt} = \int_{T_1}^{T_{sol}} c_{p,sol}(T,p)dT + \Delta h_{fus} + \int_{T_{sol}}^{T_{melt}} c_{p,melt}(T,p)dT \tag{1.4}$$

Energy efficiency for atomization processes is often expressed as the ratio between the theoretical surface energy e_{powder} and the effective energy needed to perform the atomization process, $e_{atomization}$:

$$\eta_{atomization} = \frac{e_{powder}}{e_{atomization}} = \frac{\sigma S_m}{e_{gas} + \Delta h_{gas} + \Delta h_{melt}} \tag{1.5}$$

To understand the impact of this formula on gas atomization problems, we introduce realistic numbers to estimate energy efficiency of gas atomisation processes. Two typical process examples (the ones we will be discussing in chapter 3) are shown in table 1.2 and we see how disastrous energy conversion of gas atomization processes really is.

Table 1.2: Energy efficiency of gas atomization processes

metal melt		**aluminium**	**steel**
melt superheat	[°C]	215	215
atomization gas temperature	[°C]	20	400
atomization gas pressure	[bar]	16,6	10
GLR (gas to liquid ratio)	[-]	8,49	1,10
specific surface area	[m^2/kg]	200	20
surface tension	[N/m]	0,9	1,87
surface energy	[kJ/kg]	0,18	0,0374
gas compression energy	[kJ/kg]	236	194
gas heating energy	[kJ/kg]	0	382
melting energy	[kJ/kg]	1342	1013
total energy	[J/kg]	3349	1647
energy efficiency	**[-]**	**0,0054%**	**0,0023%**

Knowing that the annual production e.g. of aluminium powder is several hundred thousands of tons [UNA1998], we understand that any optimization of powder production process via gas atomization can lead to a major contribution in a reduction of energy consumption.

1.4. Empirical Correlations to Predict Particle Sizes in Melt Atomization

The attempts to predict particle size in gas atomization with one single equation are numerous and – in most cases – related to specific atomization problems, while it is difficult to find correlations which are applicable to different atomizers operated with various materials (given the complexity of the problem, this is not surprising!). A good overview of these attempts was done in 1988 by Mehrotra [MEH1988], and, 3 years later, by Aller and Losada [ALL1991].

However, the first attempt – commonly cited – was done by by Nukiyama and Tanasawa. In a series of reports (1937-1940), translated to English by the Canadian Department of National Defence in 1950, they discussed droplet size distributions of fuel sprays at various conditions for the nozzle shown in figure 1.8. Their empirical equation relates the Sauter diameter d_{32} to materials' properties and operating conditions as follows (SI units):

$$d_{32} = 0{,}585\sqrt{\frac{\sigma}{v_{rel}^2 \rho_{melt}}} + 53{,}2\left(\frac{\eta_{melt}^2}{\sigma \rho_{melt}}\right)^{0{,}225}\left(\frac{\dot{V}_{melt}}{\dot{V}_{gas}}\right)^{1{,}5} \qquad (1.6)$$

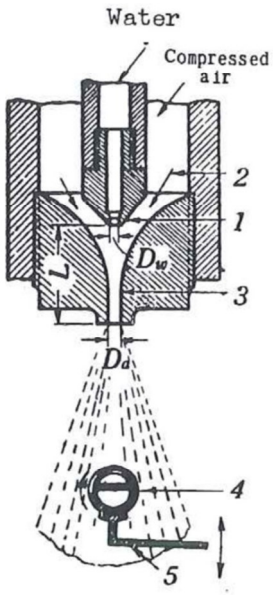

Figure 1.8: Nukiyama and Tanasawa atomizer [NUK1937]: 1=water nozzle, 2=air nozzle, 3=convergent air orifice, 4=tubular shutter, 5=micro-traveller

The first term is corresponding to the Weber number built with melt density (also used by Lubanska 35 years ago) and is influenced by relative gas velocity. The second term introduces gas-to-liquid ratio and becomes less important in case of higher gas-to-liquid ratios, higher liquid densities, lower viscosities. As the range of liquids used is narrow, the practical use of this equation is low. In figure 1.9, results using this equation are shown for different materials at typical atomization conditions (v_{rel}=a/2, GLR=0,25…6 kg_{gas}/kg_{liq}). The Sauter mean diameter d_{32} is decreasing with increasing gas to liquid ratio (GLR) and converging to a value defined by the first term of the equation. For typical melts (tin, copper) the influence of the second term is low, while for water and slag the influence of the second term is more important. Figure 1.9 suggests that materials like tin or copper are easier to atomize than water, which is clearly wrong. Nevertheless the results for water droplets given by this equation are in the right order of magnitude.

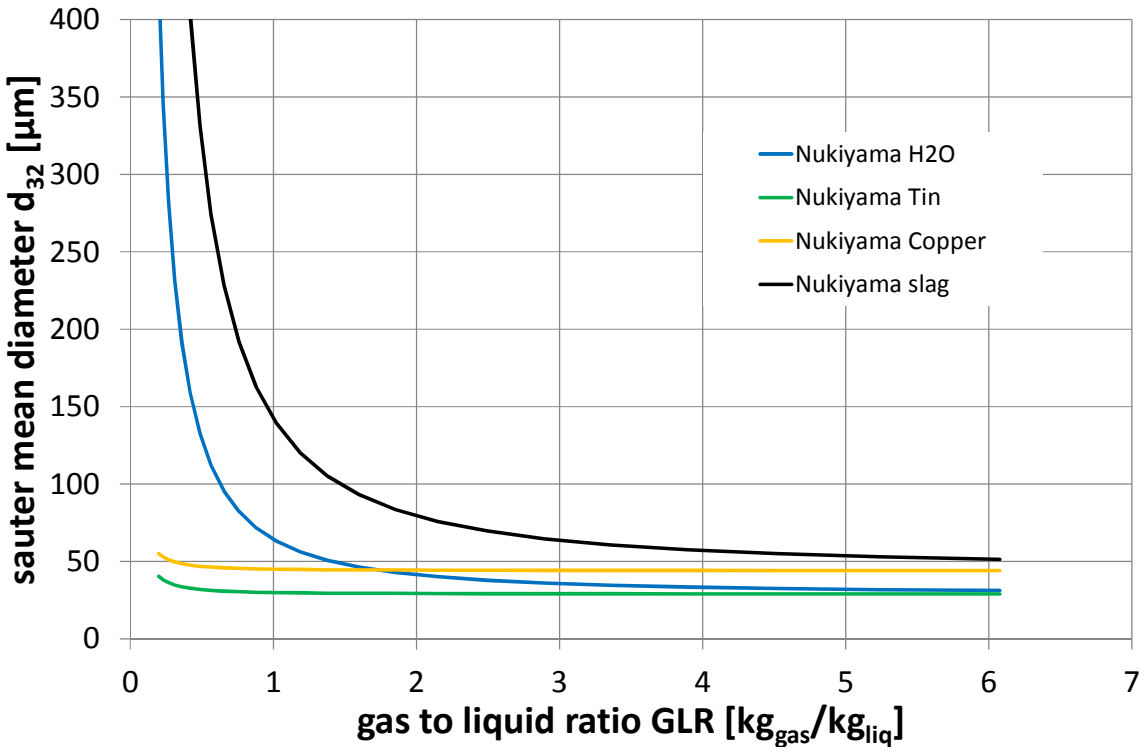

Figure 1.9: Prediction of Sauter mean diameter following the equation of Nukiyama and Tanasawa for various liquids

Understanding the importance of kinetic energy of gas atomization, Wigg [WIG1964] did spray experiments with wax, but he also analysed spray data of other researchers finding the following equation for mean particle sizes for twin fluid atomization:

$$d_{50} = 20 v_{melt}^{0,5} \dot{m}_{melt}^{0,1} d_{gas}^{0,1} \sigma^{0,2} \rho_{gas}^{-0,3} v_{rel}^{-1} \left(1 + \frac{\dot{m}_{liq}}{\dot{m}_{gas}}\right)^{0,5} \tag{1.7}$$

The value of this equation lies in the idea that the influence of any possible factor – depending on the atomization system – can be assessed by atomization trials determining the fit exponent for the factor.

Wigg's equation was empirically modified by Lubanska [LUB1970], who did atomization trials with different open jet arrangements and varying liquid properties and derived a correlation between particle mass median diameter, Weber number and gas and liquid viscosities for different liquid metals such as iron, tin or low melting point alloys.

$$\frac{d_{50}}{d} = K \left(\left(1 + \frac{\dot{m}_{liq}}{\dot{m}_{gas}}\right) \frac{\nu_{melt}}{\nu_{gas}} \frac{\sigma}{\rho_{melt} v_{rel}^2 d} \right)^{0,5} = K \left(\left(1 + \frac{\dot{m}_{liq}}{\dot{m}_{gas}}\right) \frac{\nu_{melt}}{\nu_{gas}} \frac{1}{We_{Lub}} \right)^{0,5} \tag{1.8}$$

In equation (1.8), the Weber-Number is composed with the liquid density, the liquid delivery tube diameter d and the velocity of the gas at the atomization point, while K is a factor to be determined for any particular nozzle arrangement (lying between 40 and 50).

Results for Lubanska's equation:

In figure 1.10 (left picture), the influence of the gas to liquid ratio on particle sizes is shown for different materials according to the Lubanska equation. Values for nozzle diameter and relative velocity are 3,17 mm and 166 m/s (which is 50% of sonic velocity a). The curves show the typical shape of a strong decrease of particle sizes at low gas to liquid ratios, while there is almost negligible decrease at high gas to liquid ratios. According to the Lubanska equation, water and tin are the easiest materials to atomize, while iron and – outstanding – slag, are more difficult to be divided into tiny particles. Figure 1.10 (right picture) shows the influence of gas velocity on particle size for liquid aluminium (again: d=3,17mm). As expected, it is advisable to increase gas velocity for finer powder.

Figure 1.11, (left picture) describes the influence of gas properties on particle size according to Lubanska's equation. Higher velocities (sonic velocity increases with gas temperature) lead to finer particles. At higher temperatures, melt viscosity is lower, which also has a positive effect on particle sizes. Helium with a sonic velocity of 1520 m/s at 400°C leads to the finest powder. Drawback of Lubanska's model is the disregard of the gas density, so the influence of gas properties might be overrated here. The right picture shows the influence of nozzle diameter on particle sizes – according to Lubanska, there is a decrease by factor $d^{0,5}$.

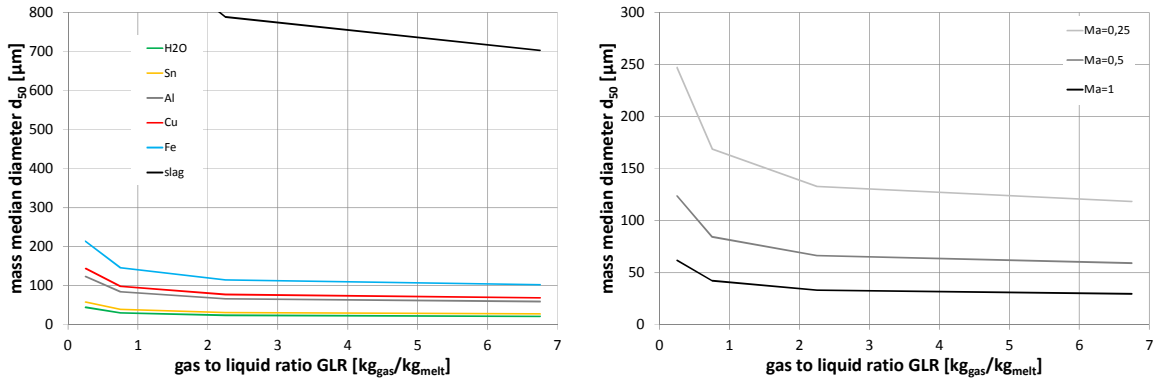

Figure 1.10: Influence of gas to liquid ratio on particle size for different materials (air at Ma=0,5; d_{nozzle}=3,17mm) (left picture); influence of Mach number on particle size for aluminium, d_{nozzle}=3,17mm) (right picture)

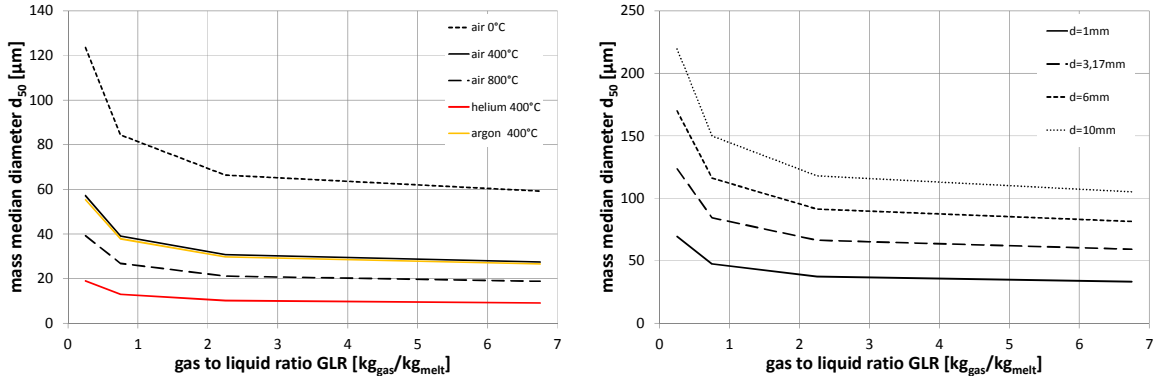

Figure 1.11: Influence of gas properties on particle size (left picture); influence of nozzle diameter on particle size; melt = aluminium (right picture)

A generalization of Lubanska's equation was suggested by Rao et al. [RAO1981]:

$$\frac{d_{50}}{d} = k\left[\left\{\left(1+\frac{\dot{m}_{melt}}{\dot{m}_{gas}}\right)\frac{\nu_{melt}}{\nu_{gas}}\right\}^{0,5}\left\{\frac{\sigma}{\rho_{liq}v_{rel}^2 d}\right\}^{0,5}\right]^m \tag{1.9}$$

With two measurement points, parameters k and m can be determined and the equation can be optimized for different nozzle configurations.

A similar approach was chosen by Tornberg [TOR1991], who applied a force balance on an open melt jet hit by a gas jet at 90° (see figure 1.12). Also here, two system constants (A and B) need to be determined for a specific nozzle arrangement by atomization trials (equation 1.10).

$$d_{50} = \sqrt{\frac{A\sigma}{\rho_{melt}\frac{\dot{m}_{gas}}{\dot{m}_{melt}}v_{gas}\left(1-B\eta_{melt}d_{jet}\right)}} \tag{1.10}$$

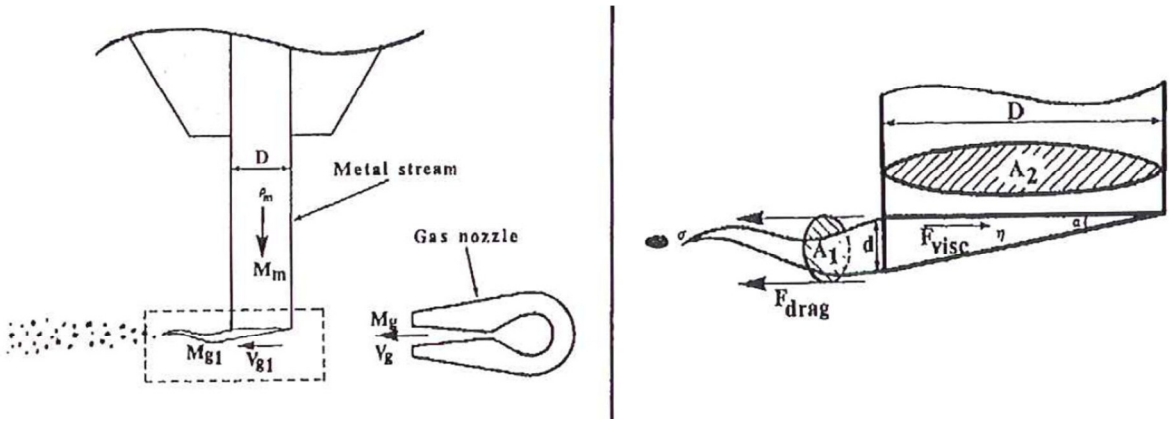

Figure 1.12: Tornberg's nozzle arrangement for the prediction of particle size.

1.5. Scope of this Work

This work shall lead to an improved understanding of the gas atomization process by analysing the different steps starting with primary breakup and ending with frozen particles.

As the equations described in chapter 1.4 are far from a "universal" equation to predict particle sizes in twin fluid atomization, the present work tries to take account of the complexity of the process with its many influences and geometrical variations and shall be a step to a better prediction of particle sizes.

Following a concept first presented by Dombrowski and Johns [DOM1963], ligaments are formed from the bulk liquid due to the gas flowing with a velocity relative to the liquid. These ligaments break down into primary droplets, which – under certain conditions – undergo secondary breakup. At the same stage, the droplets are accelerated, they cool and freeze and try to spheroidise (figure 1.13).

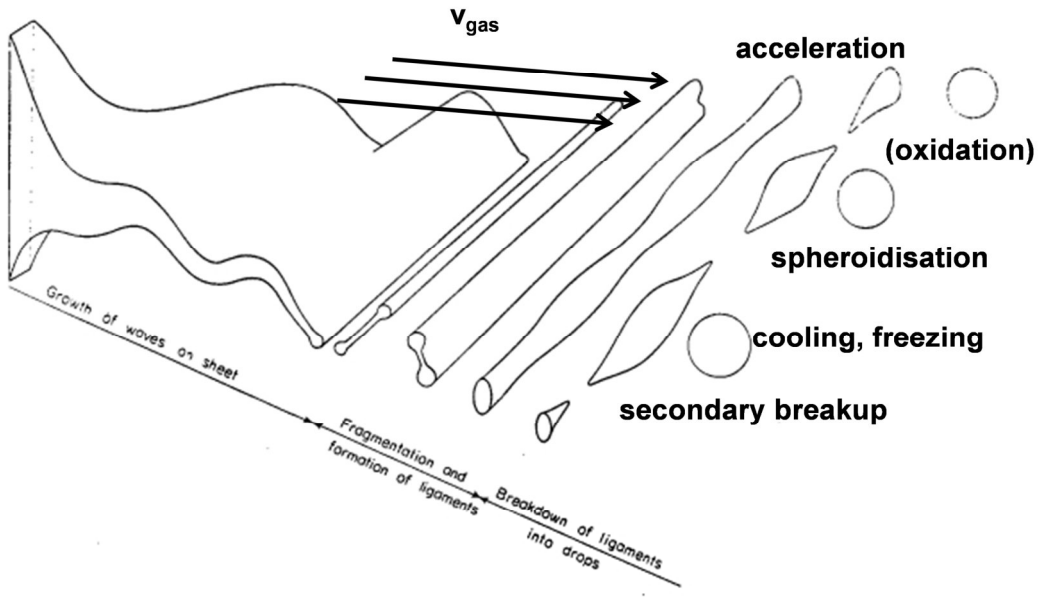

Figure 1.13: Primary breakup of a disintegrating liquid sheet according to Dombrowski and Johns [DOM1963]; the melt flows into the same direction as the gas, at much lower velocity

Based on the idea of a stepwise process of atomization and droplet formation, it becomes clear that a fundamental description of liquid bulk atomization has to start with a primary instability calculation of the deforming gas/liquid interface.

A flow sheet for this conception and all further steps can be seen in figure 1.15. The necessary theoretical background comprises the gas velocity due to nozzle flow (chapter 2.1.), the primary breakup (chapter 2.2.), ligament breakup (chapter 2.3.) and the secondary breakup behavior of the droplets formed (chapter 2.4.).

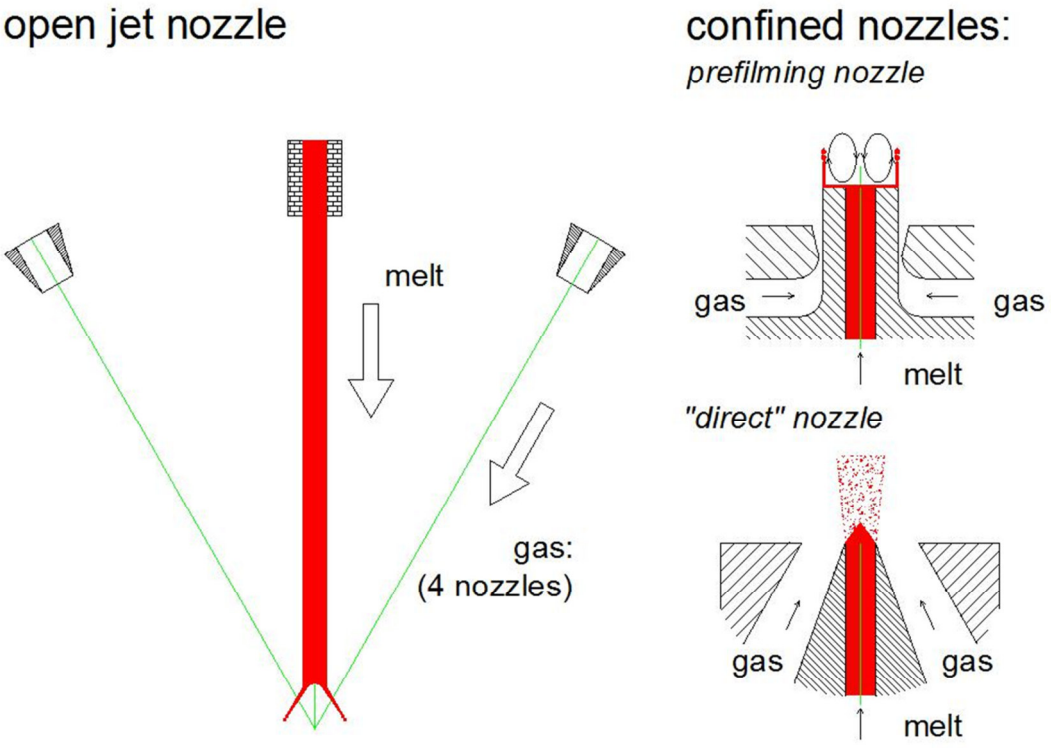

Figure 1.14: Melt atomization systems considered in this study

In a second section, the theoretical concept will be applied on technologically relevant atomization systems as shown in figure 1.14. The first atomizer case study introduces a typical "open jet" atomization problem, in the second case study, a prefilming nozzle according to Ünal [ÜNA1987] will be described. For comparison, a "direct" confined atomizer is described using comparable operating parameters (atomizer case study 3).

In a final chapter, still existing limitations of the calculation concept are discussed and suggestions for further work are provided.

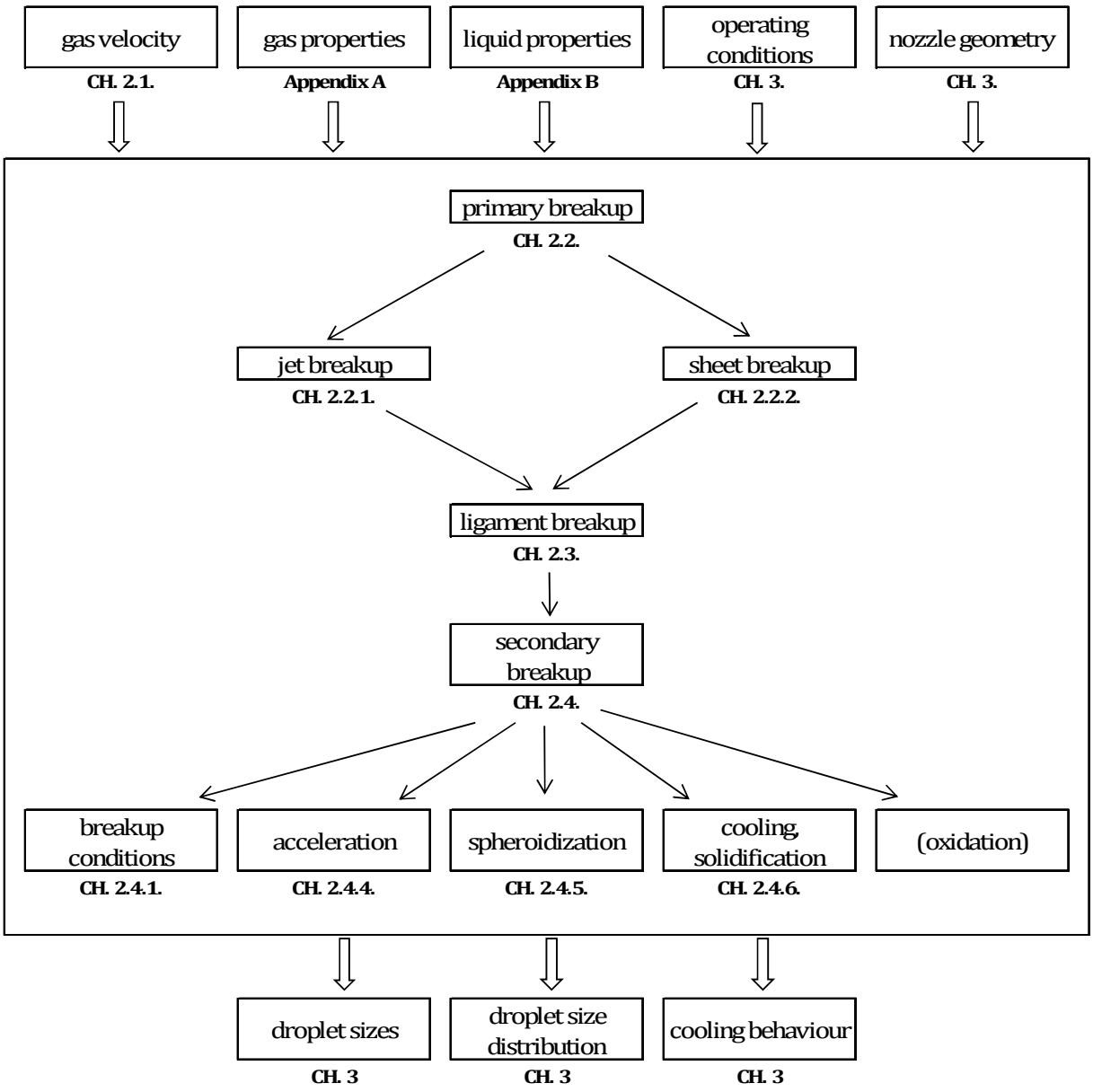

Figure 1.15: Flowsheet to describe the calculation concept and the necessary theoretical background in the planned investigation of gas-induced melt atomization processes

2. Model Approach

2.1. Estimation of the Gas Velocity

2.1.1. Introduction to Nozzle Flow

A pressure difference between a gas reservoir (reservoir pressure p_0) and ambiance (pressure p_1), those two connected by a nozzle, results in a gas flow from the place with higher pressure to the one with lower pressure. In case the pressure ratio p_0/p_1 exceeds the critical pressure ratio (see equation 2.1 and table 2.1), we expect sonic velocity in the narrowest cross section of the nozzle.

The critical pressure ratio is:

$$\frac{p_{0,crit}}{p_1} = \left(1 + \frac{\kappa-1}{2}\right)^{\frac{\kappa}{\kappa-1}} \qquad (2.1)$$

Table 2.1: Critical pressure ratio for 1- and 2-atomic gases

	gas	κ [-]	$p_{0,crit}/p_1$
1-atomic gases	Helium, Argon	1,67	2,055
2-atomic gases	Air, Nitrogen	1,4	1,893

Depending on the shape of the nozzle (convergent, convergent-divergent) and the pressure ratio p_0/p_1, we distinguish between underexpanded, ideal and overexpanded nozzle flow. A detailed overview of these circumstances and their effects on gas atomization can be found e.g. in [SCHR2003] or [HEC1998].

In standard gas atomization nozzles, the operating gas pressures are much higher than the critical pressure ratio and convergent nozzles are used, so underexpanded flow is expected. In this case, the pressure in the narrowest gas section is dissipated downstream from the nozzle exit the way shown in figure 2.1 (taken from [HEC1998]).

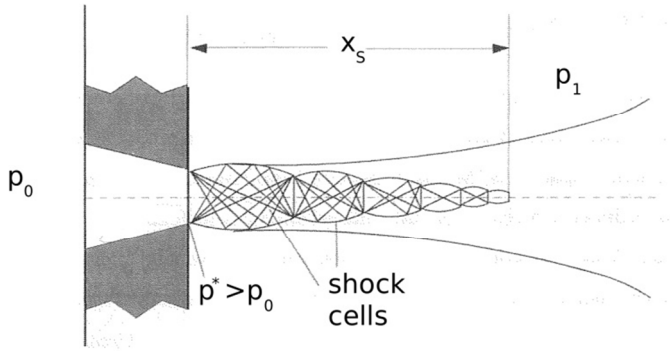

Figure 2.1: Underexpanded nozzle flow; x_S is the length of the supersonic core; p_0 is the gas reservoir pressure, p_1 is the ambient pressure, p* is the pressure in the narrowest cross section

Within the supersonic core, state variables are strongly fluctuating. The length x_S of the supersonic core is proportional to the narrowest diameter and depending on pressure ratio and nozzle shape. A convergent-divergent nozzle operating at design conditions (pressure ratio, gas temperature) is expected to result in longer supersonic cores. This was shown e.g. by Mates and Settles [MAT2005], who studied supersonic core lengths for different nozzle configurations by Schlieren photography. As an example, the centerline Mach number for a convergent and a convergent-divergent nozzle at varying pressure ratios is shown in figure 2.2.

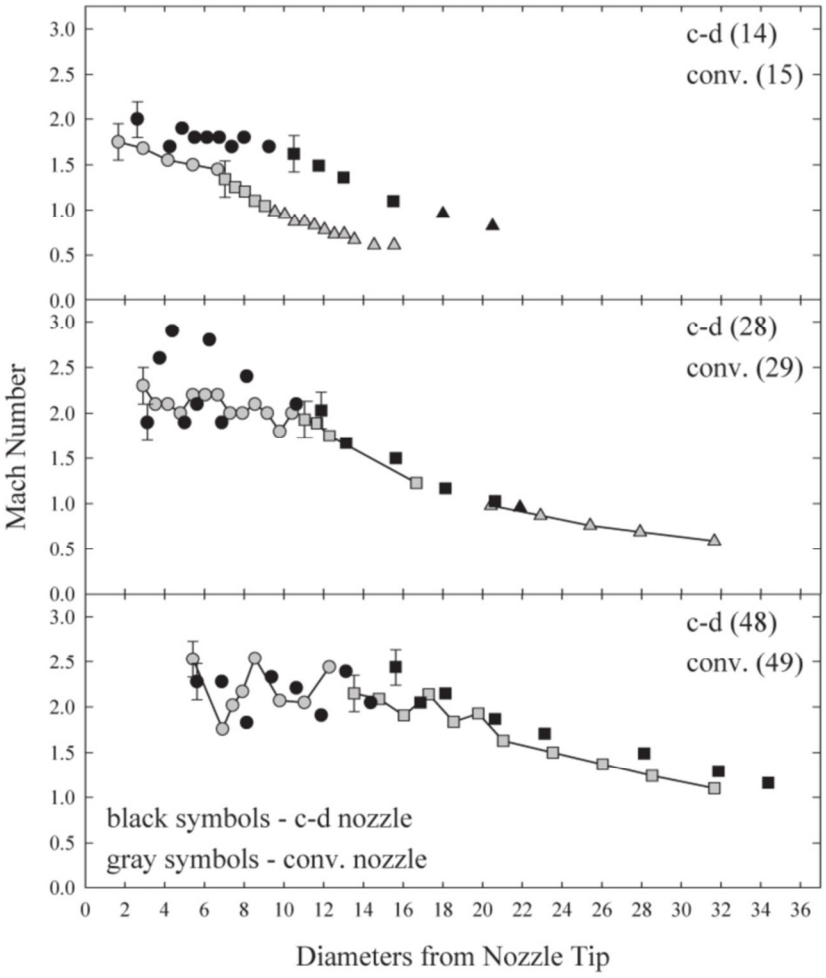

Figure 2.2: Centerline Mach numbers for a convergent-divergent and convergent nozzle, p_0/p_1 values in parantheses. At design pressure ratio (upmost picture), the benefit of the convergend-divergent nozzle design is convincing [MAT2005]

Outside the supersonic core, isobaric conditions are reached. Gas is entrained from the surrounding and the velocity is strongly decreasing. Velocity profiles are shown exemplarily in figure 2.3 for an initial Mach number Ma=1,5. The length of the supersonic core is about 9 nozzle diameters. After 20 nozzle diameters, maximum gas velocity is less than 50% of the initial velocity U_P.

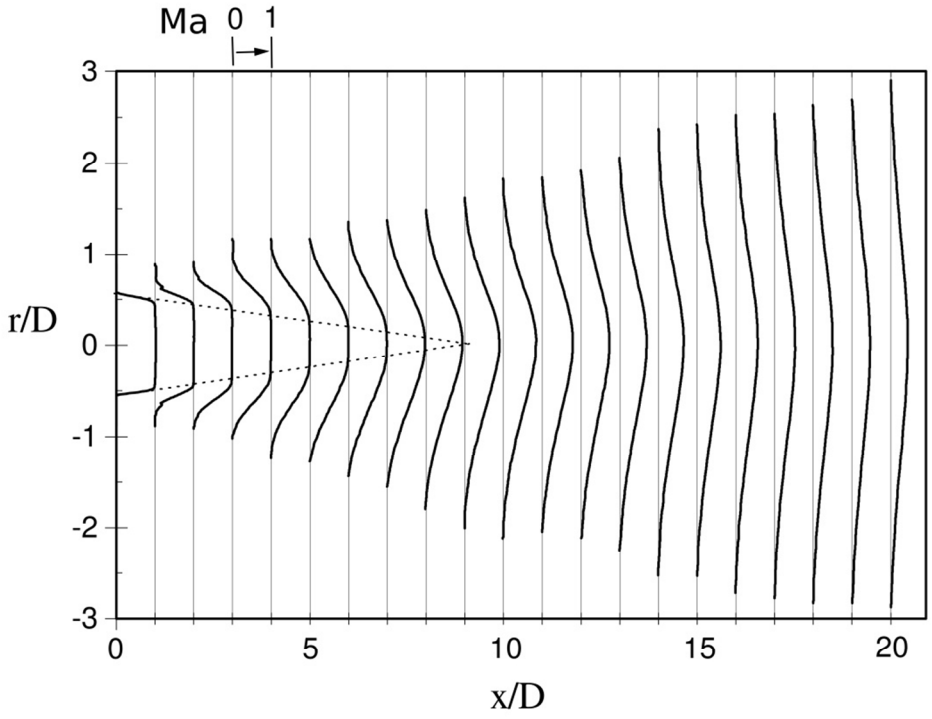

Figure 2.3: Velocity profiles of a supersonic jet expanding from a nozzle with diameter D [MUR2000]

2.1.2. Velocity decay after nozzle exit

The velocity decay after nozzle exit was the subject of numerous investigations, [AND55, FRI97, BER99, SEE1973, KOR1984, GRA1991] their results being introduced in figure 2.4. These data all show a strong decay after nozzle exit, and the dependence on the ratio x/D (distance x from nozzle exit/nozzle diameter) shows the same shape. Differences could be that e.g. Bergmann did use a multijet nozzle expecting that the jets' flows are supported by one another, or also that Anderson's experiments were done at elevated temperatures – a lower gas density leads to a stronger velocity decay.

We also have to distinguish between coaxial jets and flat jets - Schlichting [SCHL1956] describes the increase of the jet width for flat and round jets as directly proportional to distance x from nozzle exit, while the maximum velocity is decreasing with $x^{0,5}$ for flat jets and with x for axisymmetric jets (see table 2.2.).

Table 2.2: Velocity decrease of a flat and axisymmetric jets according to Schlichting

	width	maximum velocity
Flat Jet	x	$x^{-0,5}$
Axisymmetric Jet	x	x^{-1}

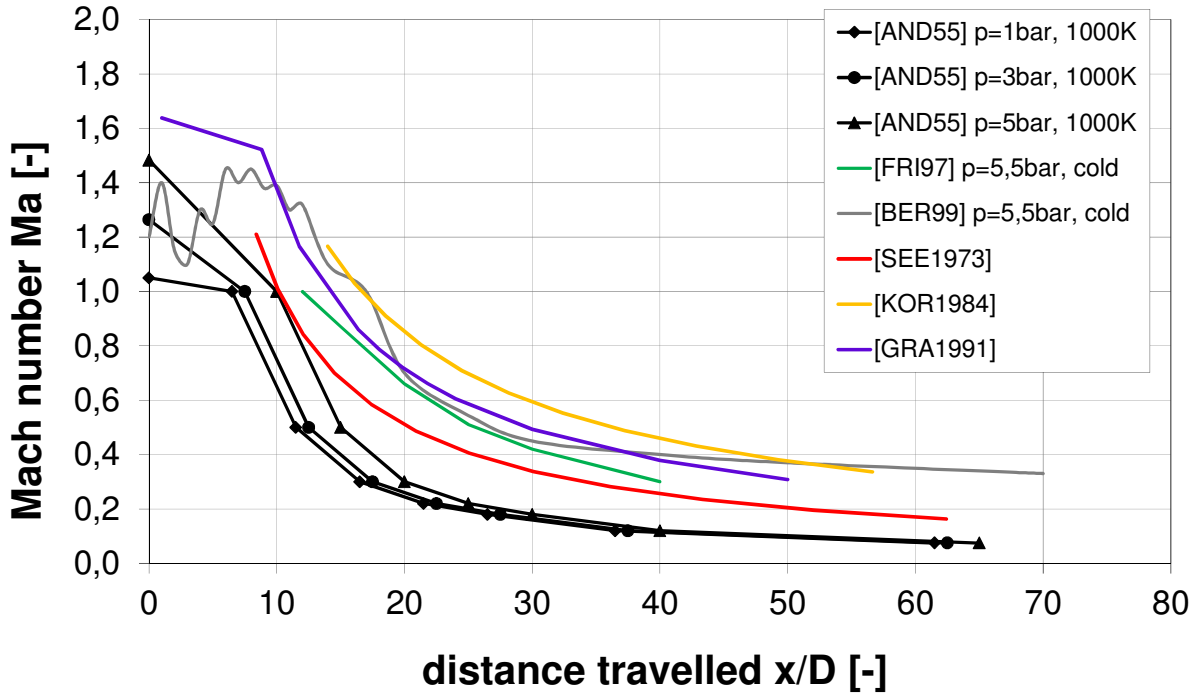

Figure 2.4: Gas jet velocity decay from nozzle tip as a function of the distance travelled following different authors

2.1.3. Graf's model for calculating velocity decay

A whole set of equations for the flow calculation of an expanding gas jet was presented by Graf et al. [GRA1991]:

Gas velocity in critical nozzle flows is defined as:

$$v^* = \sqrt{2\frac{\kappa}{\kappa-1}R_m T_0\left[1-\left(\frac{p_1}{p_0}\right)^{\frac{\kappa-1}{\kappa}}\right]} \tag{2.2}$$

With A* being the narrowest cross section (exit cross section for convergent nozzles, laval nozzle cross section for convergent/divergent nozzles), gas consumption is defined as:

$$\dot{m}_{gas} = A^*\left(\frac{2}{\kappa+1}\right)^{\frac{\kappa+1}{2(\kappa-1)}}\frac{p_0}{\sqrt{R_m T_0}} \tag{2.3}$$

Maximum Mach number is defined by:

$$Ma_{max} = \sqrt{\frac{2}{\kappa-1}\left[\left(\frac{p_0}{p_1}\right)^{\frac{\kappa-1}{\kappa}}-1\right]} \tag{2.4}$$

Momentum conservation in atomization direction tells us that

$$\dot{m}_{gas} v_{gas} = const \tag{2.5}$$

Secondary gas is entrained by the high speed gas stream which leads to a velocity decay. The velocity profile shows a Gaussian distribution, so the mean velocity at the position x/D is:

$$\bar{v}_{x/D} = \frac{v_{max,x/D}}{2} \tag{2.6}$$

At the same position x/D, entrained gas mass can be calculated from:

$$\dot{m}_{gas} v_{gas} = \dot{m}_{gas,x/D} \frac{v_{max,x/D}}{2} \tag{2.7}$$

Graf then adapted Koria's relation [KOR1984] to calculate maximum gas velocity, in nondimensional terms written as:

$$Ma_{Koria} = \frac{v_{gas}}{a_{gas}} = 3{,}63 \left(\frac{p_0}{p_1}\right)^{0{,}753} \left(\frac{x}{D}\right)^{-0{,}92} \tag{2.8}$$

a_{gas} and v_{gas} are the sonic velocity and the gas velocity at the position x, which can be calculated from Mach number and sonic velocity in the gas reservoir a_0:

$$a_{gas}^2 = a_0^2 - \left(\frac{\kappa-1}{2}\right) v_{gas}^2 \tag{2.9}$$

$$v_{gas} = \sqrt{\frac{Ma^2 a_0^2}{1+Ma^2\left(\frac{\kappa-1}{2}\right)}} \tag{2.10}$$

Thermodynamic conditions as a function of Mach number can be calculated as follows:

$$\frac{p_0}{p} = \left(1 + \frac{\kappa-1}{2} Ma^2\right)^{\frac{\kappa}{\kappa-1}} \tag{2.11}$$

$$\frac{\rho_0}{\rho} = \left(1 + \frac{\kappa-1}{2} Ma^2\right)^{\frac{1}{\kappa-1}} \tag{2.12}$$

$$\frac{T_0}{T} = 1 + \frac{\kappa-1}{2} Ma^2 \tag{2.13}$$

Maximum Mach number as a function of nondimensional distance from nozzle exit (equations 2.4 and 2.8) can also be presented in a diagram from which values for Mach number can be extracted graphically (see figure 2.5).

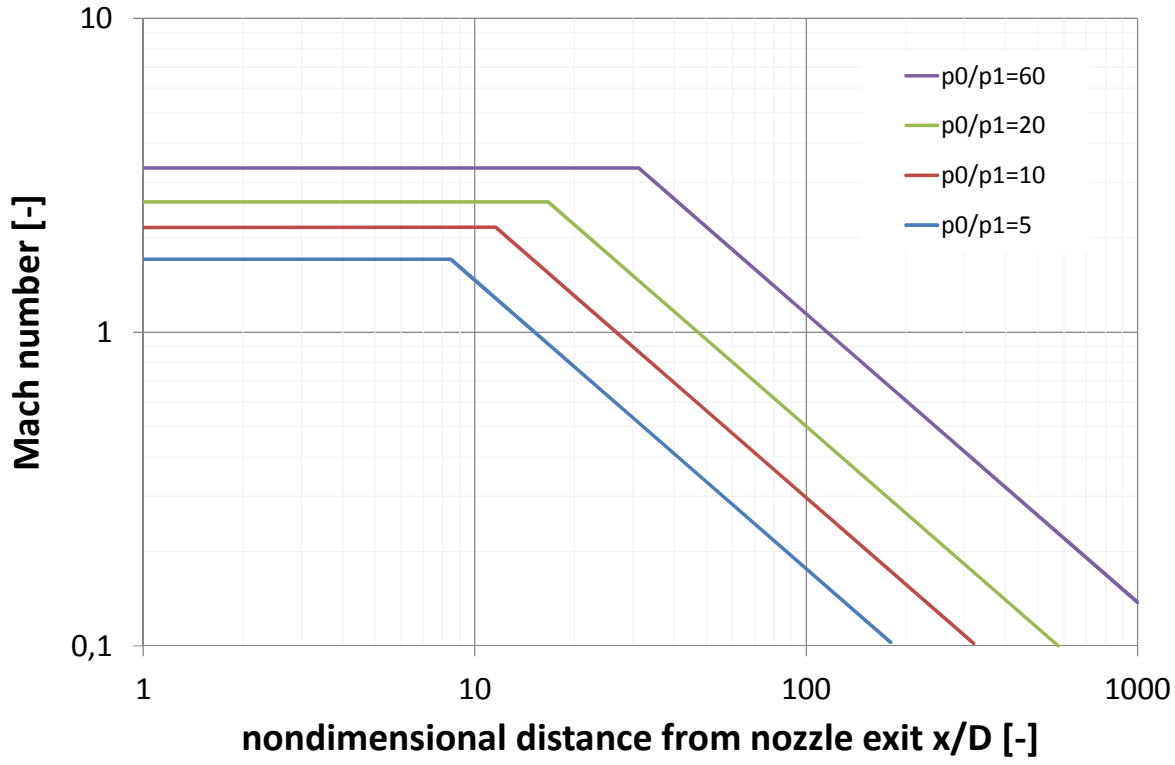

Figure 2.5: Gas Mach number as a function of nondimensional distance from the exit of a convergent nozzle [GRA1991]

2.1.4. Velocity Decay after Primary Breakup

From the point where gas hits the melt stream, which is then accelerated, the prediction of gas velocity decay becomes even more unclear. For confined nozzles, this is the case right after nozzle exit, for open jet configurations, gas jet suffers from decay as described above.

Kutkin et al. measured gas and melt velocities for a confined nozzle at varying gas nozzle diameters and could show an influence of the nozzle diameter on velocity profile. As they did not disclose exact operating conditions, their study is only of historical value for us (see figure 2.6).

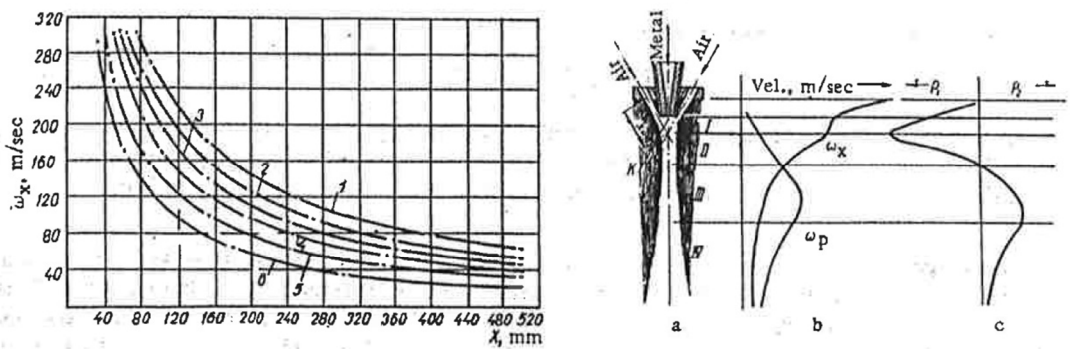

Figure 2.6: Gas and particle velocities at the nozzle exit of a confined nozzle with different gas nozzle diameters [KUT1971]

Liang and Lavernia [LIA1993] suggested the following equation to estimate gas velocity at distance x from nozzle exit:

$$v_{gas}(x) = v_o exp\left(-\frac{x-x_i}{x_s-x_i}\right) \quad (2.14)$$

$v_{gas}(x)$ is the gas velocity at the distance x from nozzle exit, x_i describes the length of the (super)sonic core, and x_s is a geometry related nozzle parameter.

This relation was simplified by Grant et al. [GRA1993] to the following form:

$$v_{gas}(x) = v_o exp\left(-\frac{x}{\lambda_V}\right) \quad (2.15)$$

With $\lambda_V = 3{,}04 * 10^{-4} * v_0^{1,24}$ (2.16)

Main advantage of this equation is the presence of only one parameter (v_0), and in Delplanque et al., its value is described as follows [DEL2000]: *"This correlation is generally suitable for the conditions that are present during close-coupled atomization of molten metals. Although the value of the exponent may vary somewhat, depending on atomizer design, it has been reported to provide an acceptable accuracy*."

2.2. Primary Breakup

According to a concept first presented by Dombrowski and Johns [DOM1963], the primary break-up process can be divided in 3 stages (see also [LAW1985]):

1. The formation and growth of a wave with a particular wave length λ_{max} and wave number $k_{max}=2\pi/\lambda_{max}$
2. Fragmentation and formation of ligaments and
3. The breakdown of ligaments into droplets (Rayleigh droplet formation)

This process is shown in figure 1.4. In a possible 4th stage, secondary breakup of the droplets may occur. Conditions for secondary droplet breakup and its outcomes are discussed in chapter 2.4.

With regards to atomization problems, it is obvious to distinguish between jet and sheet breakup.

2.2.1. Jet Breakup

According to the importance in many processes, primary breakup of liquid jets has been the subject of numerous scientific activities – above all in the field of fuel injector optimization, several working groups have increased the theoretical and practical understanding of primary and secondary jet breakup (see e.g. [FAE1995,LIN1998, VIL2007].

A first classification of jet breakup conditions was established in the year 1936 by Ohnesorge [OHN1936], who analyzed the jet breakup of different liquids such as water, glycerol or oil at

varying conditions. The breakup regime was identified to depend on two nondimensional numbers, the Reynolds number Re and a "viscous group" Z, nowadays named the "Ohnesorge number" Oh:

Liquid Reynolds Number:

$$Re_L = \frac{d\rho_L u_{rel}}{\eta_L} \tag{2.17}$$

Ohnesorge Number:

$$Oh = \frac{\eta_L}{\sqrt{d\rho_L \sigma}} = \frac{\sqrt{We_L}}{Re} \tag{2.18}$$

Liquid Weber Number:

$$We_L = \frac{d\rho_L u_{rel}^2}{2\sigma} \tag{2.19}$$

Three breakup regimes (Rayleigh breakup, wind-induced breakup, atomization) were described by Ohnesorge, supplemented some 40 years later, by Reitz [REI1978]], who distinguished between first-wind and second-wind-induced breakup (figure 2.7).

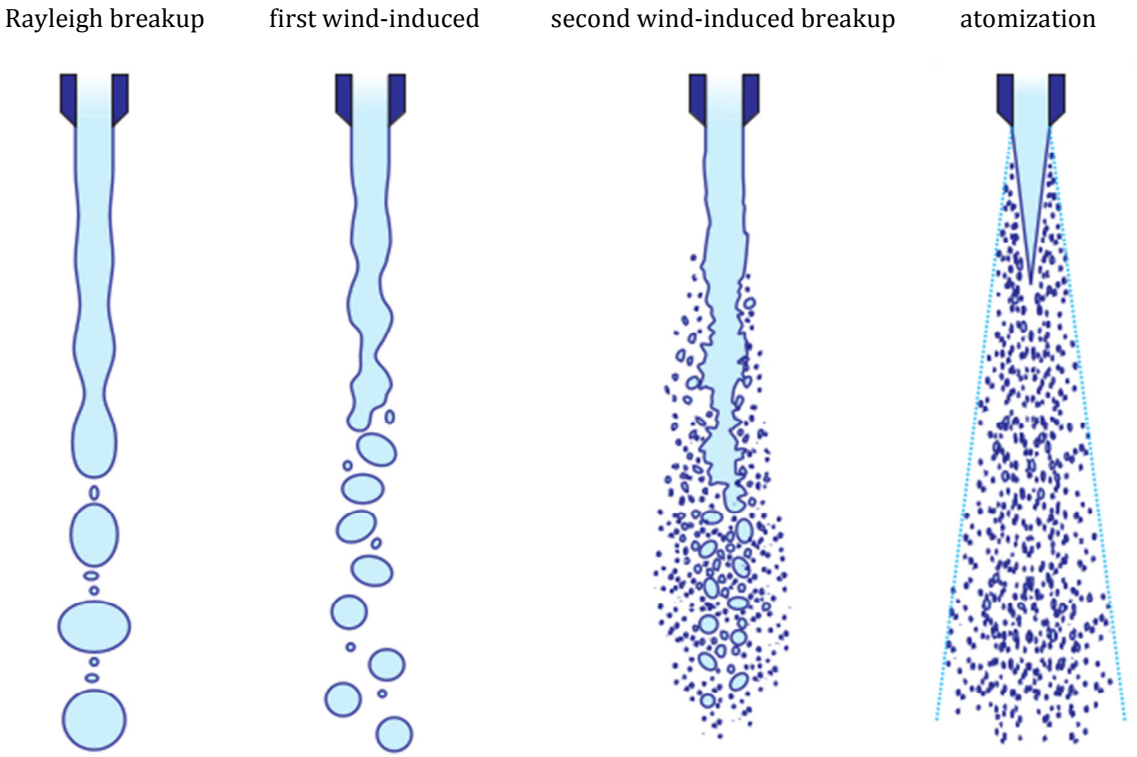

Figure 2.7: Jet breakup regimes according to Reitz (picture taken from [SCHN2003])

Reitz [REI1978] also introduced the influence of the density ratio into this problem claiming that, with increasing gas densities, smaller Reynolds and Ohnesorge Numbers are needed to achieve the limits between Rayleigh Breakup, wind-induced breakup and atomization (see figure 2.8). A detailed description of these breakup regimes is given in table 2.3. [LIU2000]. Within the current context, it should be emphasized we are normally working in the atomization regime (We_{air}>40,3 or Oh>100$Re_L^{-0,92}$).

Table 2.3: Jet breakup regimes as described in [LIU2000]

Regime	Predominant Breakup Mechanism	Criteria
Rayleigh Jet Breakup	Surface Tension Force	$We_{gas}<0,4$ or $We_{gas}<1,2+3,41Oh^{0,9}$
First Wind-Induced Breakup	Surface Tension Force, Dynamic Pressure of Surrounding Air	$1,2+3,41Oh^{0,9}<We_{gas}<13$
Second Wind-Induced Breakup	Dynamic Pressure of Surrounding Air	$13<We_{gas}<40,3$
Atomization	Unknown, but plausibly: Aerodynamic Interaction, Turbulence, Cavitation, Bursting Effect	$We_{gas}>40,3$ or $Oh\geq100Re_L^{-0,92}$

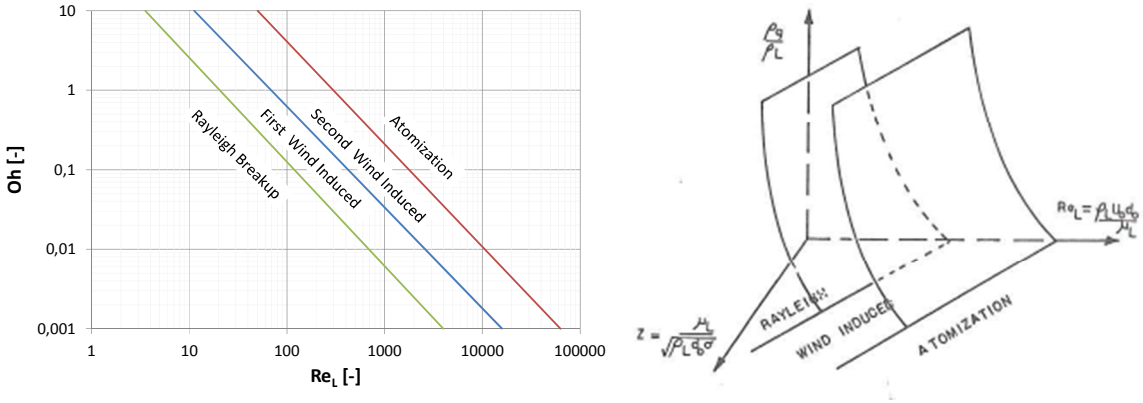

Figure 2.8: Ohnesorge diagram for a liquid jet (left); influence of gas density on breakup regime boundaries [REI1978]

Linear stability analysis of the jet surface

With the method of linear stability analysis, the growth behavior of a small perturbation in an – apart from the perturbation – stationary flow can be described. In the case of unstable conditions (the forces of the gas exercised on the melt have to be high enough), waves grow on the surface and ligaments are shed from the waves. The temporal evolution of this process is shown in figure 2.9. The complexity and accuracy of the dispersion relation is a result of the simplifications which are made and – of course – depending on the boundary conditions.

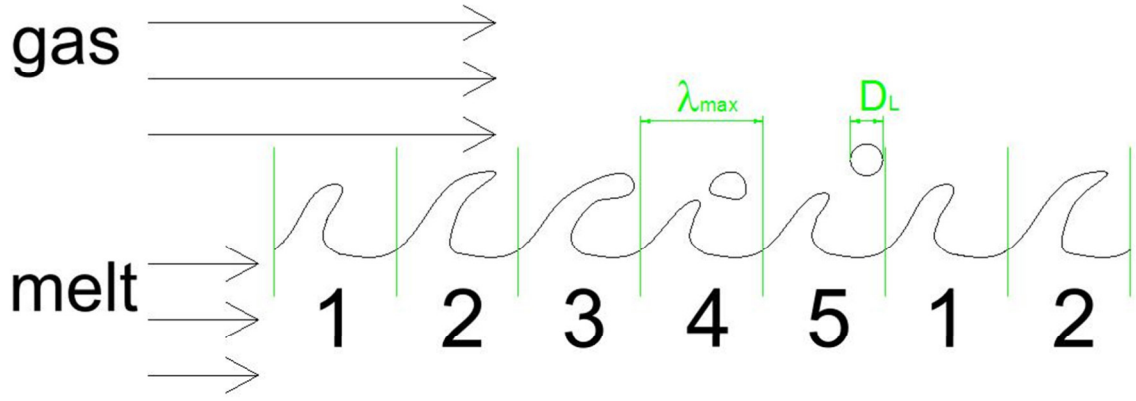

Figure 2.9: Temporal evolution of the surface waves in time steps from 1 to 5; cylindrical ligaments are shed from the surface at a frequency ω_{max} and at a wavelength $\lambda_{max} = 2\pi/k_{max}$: at time step 4, a cylindrical ligament is separated from the liquid continuum. To accomplish continuous conditions, the mass of all ligaments shed from the surface at the same has to be equal to melt production rate.

Bradley considered the 2-dimensional parallel flow of a gas and an infinitely deep liquid as shown in figure 2.10. As the size of the waves is two orders of magnitude smaller than the jet diameter, this is a reasonable simplification. The coordinate system is moving with the bulk liquid, so only a relative velocity $v_{rel}=v_{gas}-v_{melt}$ needs to be included in the model. Compressibility of the gas is included in the calculations, in [BRA1973a] with the limit of Ma≤0,9. The wave growth of perturbations of the liquid jet surface is studied starting from the Navier-Stokes equations in the general form:

$$\nabla v_i = 0 \tag{2.20}$$

$$\rho \frac{\partial v_i}{\partial t} = -\nabla p + \Delta v_i \tag{2.21}$$

(with i=melt phase or gas phase)

A spectrum of infinitesimal disturbances of the form

$$\mu = \mu_0 e^{ikx+\omega t} \tag{2.22}$$

is imposed on the initially steady surface. In Eq. (2.22) μ_0 is the initial wave amplitude and $k = 2\pi/\lambda$ is the wave number while $\omega = \omega_r + i\omega_i$ is the complex growth rate. The most unstable disturbance ω_{max} has the largest value of ω_r, and is expected to be responsible for the formation of ligaments shed from the jet surface. Hence, the goal is to obtain a dispersion relation $\omega=\omega(k)$ from which this most unstable disturbance can be deduced.

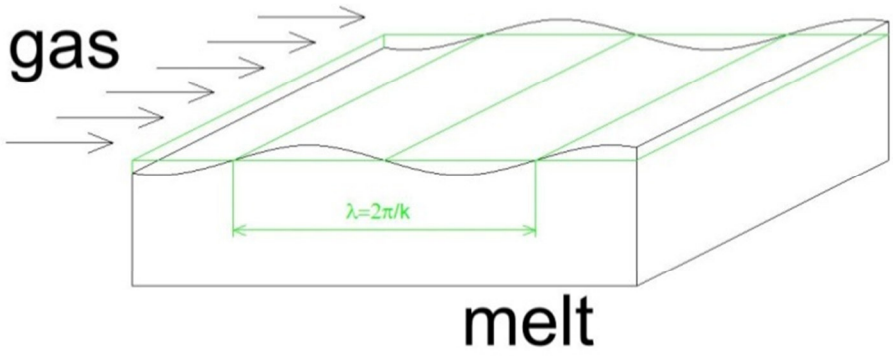

Figure 2.10: Bradley's model of wave formation on the surface

Bradley found the following set of relations to fulfill the conditions described with equations 2.20 – 2.22:

For the growth rate ω as a function of the wave number k:

$$\omega = -\nu_{melt}k^2 + \left(\nu_{melt}^2 k^4 - \frac{k\sigma}{\rho_{melt}}(k-k_1)(k-k_2)\right) \tag{2.23}$$

With

$$k_1, k_2 = \frac{\rho_{gas} v_{rel}^2}{2\sigma(1-M^2)^{\frac{1}{2}}} \pm \left(\frac{\rho_{gas}^2 v_{rel}^4}{4\sigma^2(1-M^2)} - \frac{\rho_{melt} g}{\sigma}\right)^{\frac{1}{2}} \tag{2.24}$$

As k has to be real and positive (otherwise no wave growth will occur), the relative velocity v_{rel} has to be large enough to satisfy the following relation:

$$v_{rel}^4 > \frac{4\sigma(1-M^2)\rho_{melt}g}{\rho_{gas}^2} \tag{2.25}$$

Hence, the minimum relative velocity to ensure wave growth can be estimated (for "normal" metals, it lies somewhere between 10 and 30 m/s).

Finally, the maximum wave number k_{max} with the corresponding value of ω_{max} is to be calculated with the following relation:

$$\frac{8{\nu_{melt}}^2\sigma k^5}{\rho_{melt}} - \frac{9\sigma^2k^4}{\rho_{melt}^2} + \frac{12\rho_{gas}U^2\sigma k^3}{\rho_{melt}^2(1-M^2)^{0,5}} - \frac{4\rho_{gas}^2U^4k^2}{\rho_{melt}^2(1-M^2)} = 0 \tag{2.26}$$

The fastest growing wavelength is:

$$\lambda_{max} = 2\pi/k_{max} \tag{2.27}$$

The growth factor ω as a function of the wave number k is shown in figure 2.11 for different materials. The higher the growth factor and the higher the wave number, the easier the material is to be atomized (particles will be smaller for similar conditions). According to figure 2.11, tin and aluminium are easier to atomize than copper or iron. Increasing melt viscosity leads to a slight decrease in both growth factor and maximum wave number. Increasing surface tension has got the same, but stronger effect. Increasing melt density only decreases growth factor but does not affect maximum wave number.

According to this model, gas temperature does not affect the breakup process, as gas velocity and gas density are only occurring in the group $\rho_{gas}{v_{rel}}^2$. On the other side, particle size is indirectly proportional to ambient pressure. Finally, an increase in gas velocity (Mach number) leads to a better atomization result.

For this calculation and all further ones, melt properties are assumed to be constant with temperature (for further explanation, see Appendix B) with the exception of slag, where the influence of temperature on viscosity is very strong and therefore necessary to be considered.

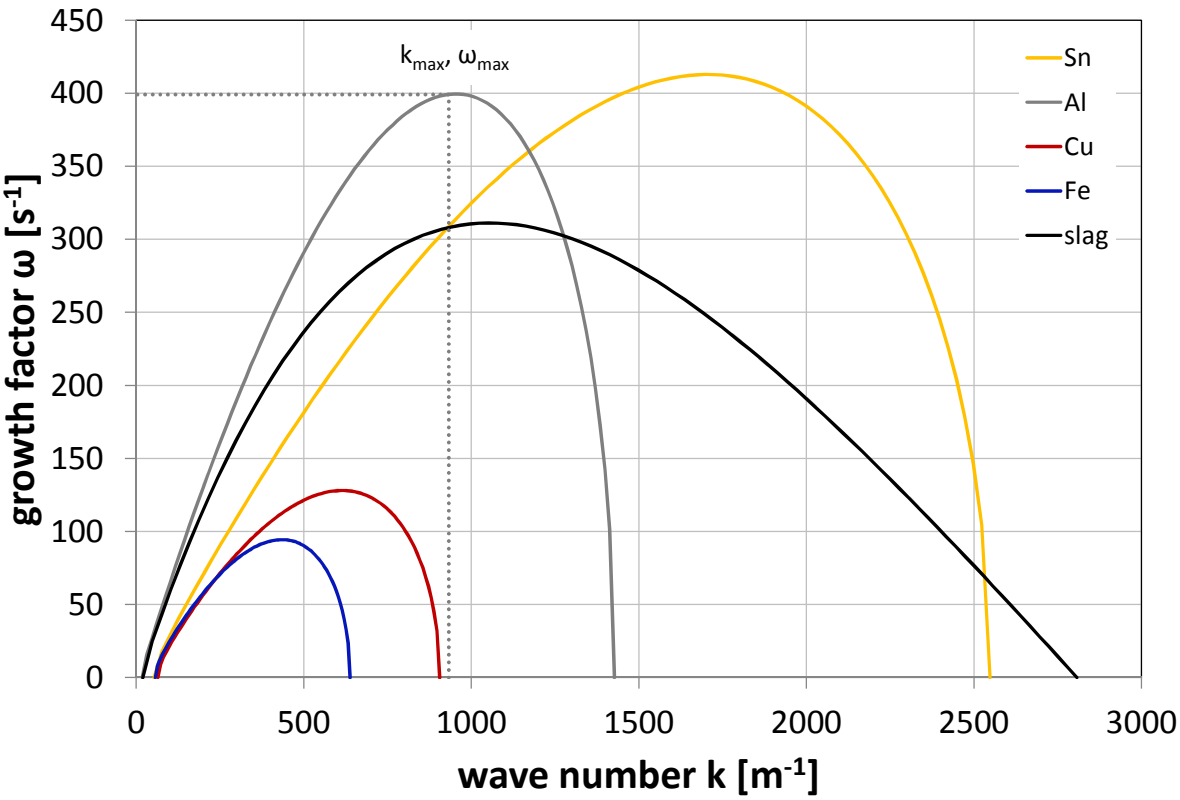

Figure 2.11: Calculated growth rates and wave numbers of disturbance waves at the jet surface following Bradley's model for different melts (cold air, relative velocity v_{rel}=50m/s)

In the second stage of the atomization process, Bradley suggested the following relation between the ligament diameter D_L and the maximum wave length, derived from visual observations:

$$D_L = \frac{\lambda_{max}}{4} \tag{2.28}$$

Finally, the ligament diameter can be related to the Rayleigh break-up mechanism, resulting in the following equation for the primary droplet diameter:

$$d = \left(\frac{3\pi}{\sqrt{2}}\right)^{\frac{1}{3}} D_L \left(1 + \frac{3\eta_L}{(\rho_L \sigma d_L)^{\frac{1}{2}}}\right)^{\frac{1}{6}} = 1{,}88 D_L (1 + 3Oh)^{\frac{1}{6}} \tag{2.29}$$

Some results for this model are exemplarily shown in figure 2.12. for different materials. Theoretical particle sizes are calculated for air at room temperature and Ma=0,5.

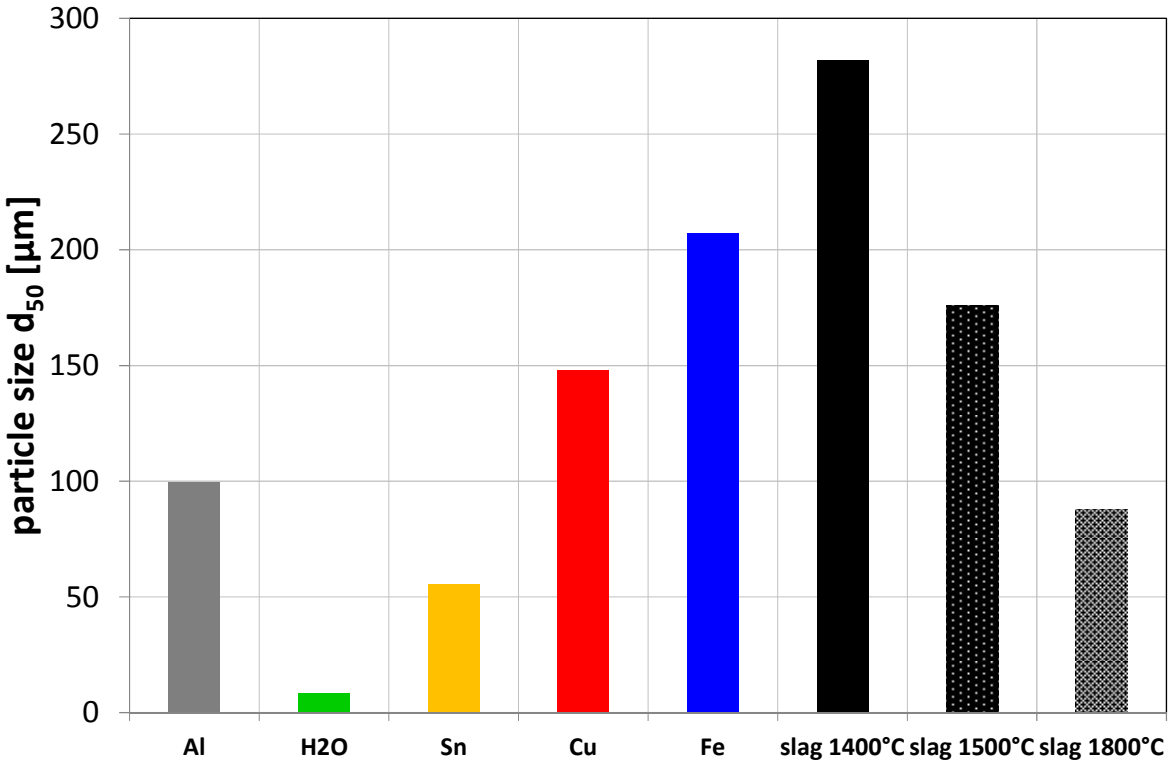

Figure 2.12 Theoretical primary droplet size of a melt disintegrated by cold air at Ma=0,5 according to Bradley's model. The influence of the melt temperature for slag is huge because its viscosity is strongly decreasing with temperature

The model of Bradley was chosen because of its simplicity, but is judged e.g. by Lawley to give a good picture of the influences on the atomization process [LAW1985]. It is one of the first to include compressibility of the gas into the calculations, with a maximum Mach number of 0,9). Furthermore, it was shown in [BRA1973b] that an additional increase of the Mach number leads only to a weak increase of k_{max} and ω_{max} (<10%). Nevertheless, some inaccuracies have to be accepted [LAW1985, MAR2002]:

- ➔ The inclination angle between the gas and the melt typically lies in the range between 15 and 45 degrees; in our example in chapter 3.2 it is 25 degrees, while Bradley's analysis assumes parallel flow.
- ➔ The mean relative velocity is not constant along the liquid jet propagation – here, the velocity is considered to be steady and onedimensional; while the primary break up occurs in the range of highest gas velocity gradients rather than at highest relative velocities along the jet axis
- ➔ The assumption of an inviscid gas neglects frictional effects in the boundary layer, which become more important for higher gas velocities.
- ➔ The results are only valid for the limit of small initial perturbations.

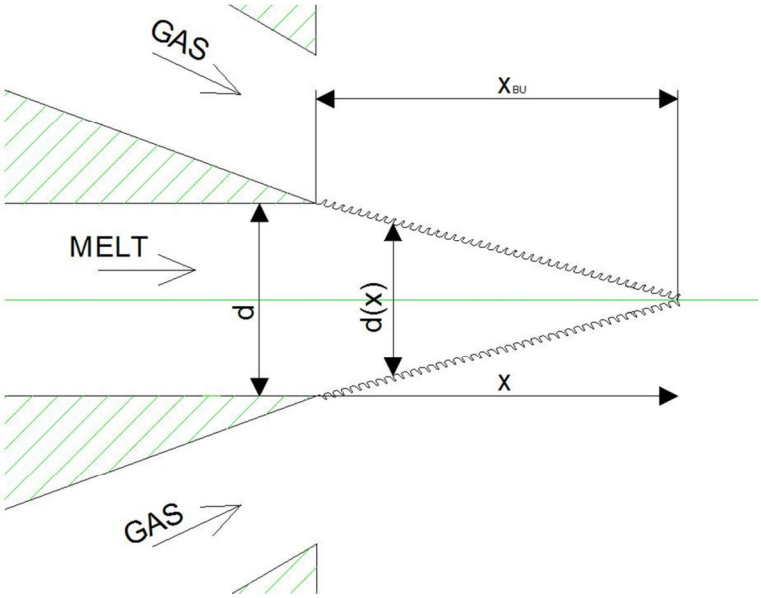

Figure 2.13: Geometrical setup to calculate the jet breakup length

By analyzing Bradley's equation and applying a simple mass balance, the breakup length of the jet can be estimated by assuming that a number of ω_{max} waves per second are emerging from the surface at a wave length $\lambda_{max}=2\pi/ k_{max}$. (see also figure 2.13).

The surface has to be:

$$A_{cone} = \frac{d\pi}{2}\sqrt{\frac{d^2}{4} + x_{BU}^2} \tag{2.30}$$

Presuming that the whole cone surface is perfectly covered with waves (at a distance λ_{max}), from which ligaments with diameter D_L are shed from the jet surface, the mass of ligaments emerging from this surface is:

$$\dot{m}_{melt} = \frac{A_{cone}}{d}\left(\frac{d}{\lambda_{max}} + 1\right)\frac{D_L^2\pi}{4}\rho_{melt}\omega_{max} \tag{2.31}$$

Hence, breakup length can be calculated (knowing that $d>>\lambda_{max}$):

$$x_{BU} = \left[\left(\frac{8}{\pi^2}\frac{\dot{m}_{melt}}{\rho_{melt}}\frac{\lambda_{max}}{\omega_{max}}\frac{1}{D_L^2}\frac{1}{d}\right)^2 - \frac{d^2}{4}\right]^{\frac{1}{2}} \tag{2.32}$$

This approach to analyze jet breakup implies a rude simplification:

It is assumed here that the relative velocity stays constant along breakup length, even as the jet thickness is decreasing due to ligaments shed from its surface, which is clearly very inaccurate – due to momentum conservation in the gas/liquid boundary layer, we have to consider that gas velocity is strongly decreasing when ligaments and droplets are accelerated. This will be discussed in further detail in chapter 3.2.

The empirical relation of Lin and Reitz for jet breakup in the atomization regime

Lin and Reitz [LIN1998] used curve-fits of numerical solutions to the dispersion equation for the maximum growth rate and the corresponding wavelength as follows:

$$\lambda_{max} = 9{,}02\,\frac{d}{2}\,\frac{(1+0{,}45Oh^{0{,}5})(1+0{,}4T^{0{,}7})}{(1+0{,}87We_{liq}^{1{,}67})^{0{,}6}} \tag{2.33}$$

With

$$T = OhWe_{gas}^{0{,}5} \tag{2.34}$$

And

$$\omega_{max} = \left(\frac{8\sigma}{d^3\varrho_{liq}}\right)^{0{,}5}\,\frac{(0{,}34+0{,}38We_{gas}^{1{,}5})}{(1+Oh)(1+1{,}4T^{0{,}6})} \tag{2.35}$$

Again, a simple mass balance is used to calculate breakup length.

A comparison between the model of Lin and Reitz and the model of Bradley in figure 2.14 shows that quite a good correlation between both models. Since Lin and Reitz did work in the field of organic fluids having low surface tensions (for which their model will have been optimized), deviations are increasing for melts with higher surface tensions (copper, iron).

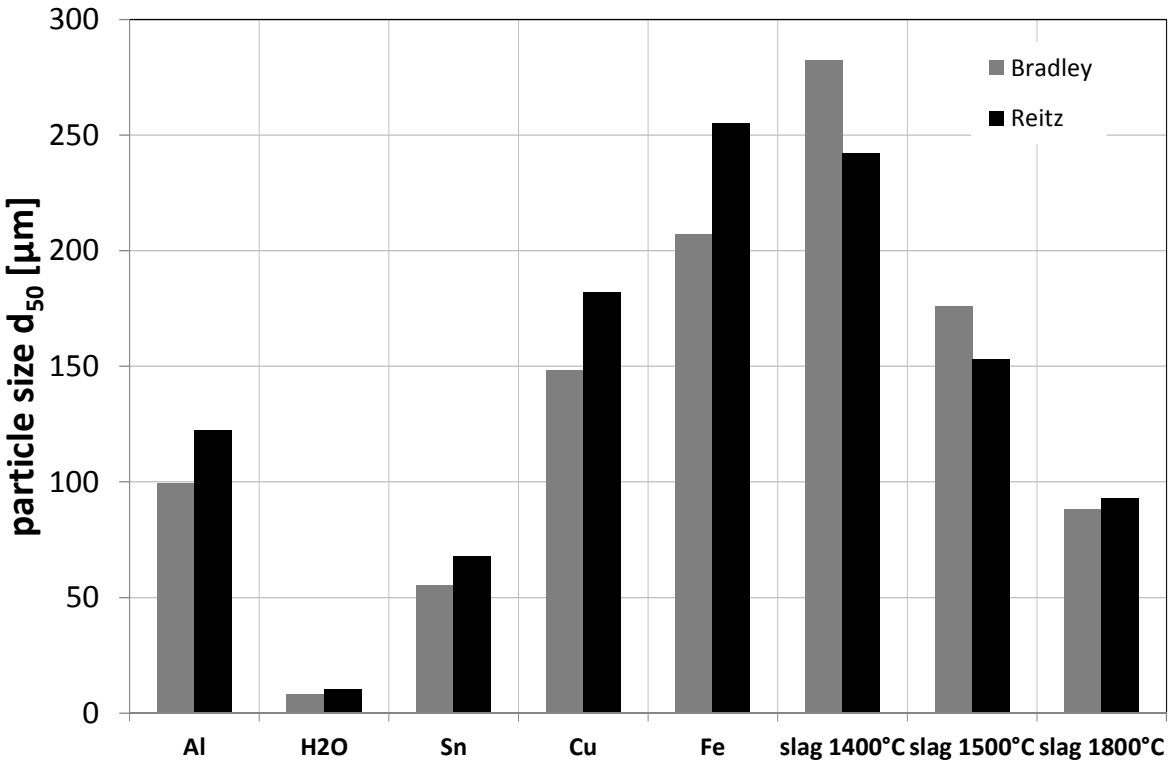

Figure 2.14: Comparison of primary droplet diameter according to the models of Lin&Reitz as well as Bradley for different melt materials; same conditions as in figure 2.12

2.2.2. Sheet Breakup

In many twin fluid atomizer systems, the melt jet is first converted into a sheet to increase primary surface (figure 2.15). This probably increases atomization efficiency, and also a narrower size distribution can be achieved, because breakup conditions are – in theory – unchanging for the entire liquid. This behavior is contrary to jet atomization where breakup conditions are becoming worse at the end of the jet.

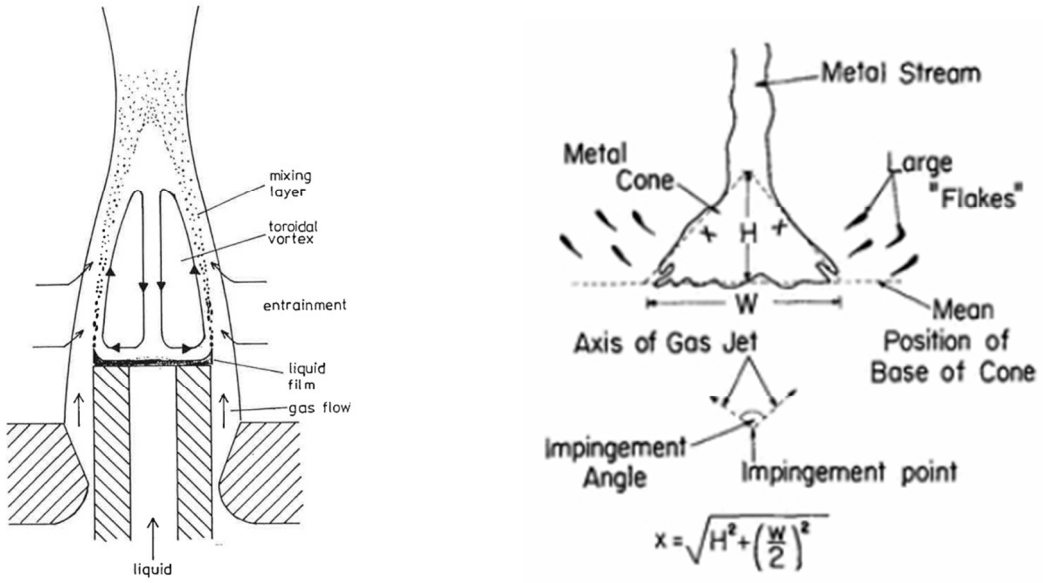

Figure 2.15: Left picture: transition of the liquid jet into a cylindrical sheet (or "liquid film") according to Ünal [UNA1989b]; right picture: transition and into a metal melt cone according to See et al. [SEE1978]

Linear stability analysis of the melt sheet

Similar to the linear stability analysis the jet surface, sheet breakup was analyzed e.g. by Senecal et. al [SEN1999]. They considered a two-dimensional, viscous, incompressible liquid sheet of thickness 2h moving with a relative velocity v_{rel} to the quiescent, inviscid, incompressible gas medium.

Again, as described in chapter 2.2.1, a small perturbation is applied on the surface (here: on the flat sheet), and growth behavior is observed.

On the one hand, Senecal et al. differentiated between antisymmetric (sinuous) waves and symmetric (varicose) waves as shown in figure 2.16, left picture. On the other hand, Senecal et al. found that – depending on the sheet Weber number – short or long wave breakup will occur. In the case of higher Weber numbers (We_{gas}>27/16), only one ligament is emerging from the melt sheet per wavelength ("short wave breakup"), while in the case of low Weber numbers (We_{gas}<27/16), two ligaments are produced per wavelength ("long wave breakup"). A sketch of short wave and long wave breakup is shown in figure 2.16 (right picture). Furthermore, it was shown that in the case of long wave breakup, the sinuous wave form is the more stable one, while, in the case of short wave breakup, the mathematical solution for both – sinuous and varicose wave forms – will be identical [MAD2007].

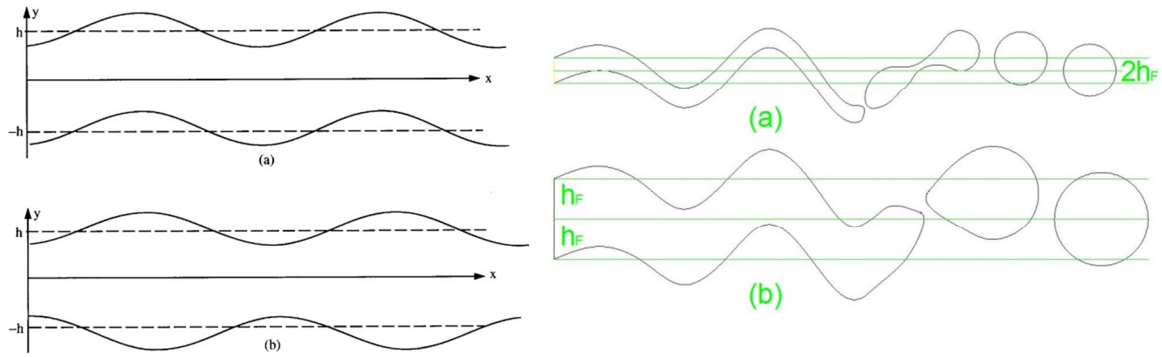

Figure 2.16: Left picture: Sinuous (a) and varicose (b) waves as a result of perturbations applied upon a two-dimensional liquid sheet, taken from [SEN1999]; right picture: long wave (a) and short wave breakup (b)

For the Weber number, Senecal et al. used the following relation:

$$We_{gas} = \frac{\rho_{gas} v_{rel}^2 h_F}{\sigma} \tag{2.36}$$

The maximum wave number k_{max} and the maximum growth rate ω_{max} of the most unstable wave can be calculated using the following relation (2.37):

$$\omega_r = -\frac{2\nu_{melt}k^2 \tanh(kh_F)}{\tanh(kh_F)+Q} + \frac{\sqrt{4\nu_{melt}^2 k^4 \tanh^2(kh_F) - Q^2 v_{rel}^2 k^2 - [\tanh(kh_F)+Q](-Q v_{rel}^2 k^2 + \frac{\sigma k^3}{\rho_{melt}})}}{\tanh(kh_F)+Q}$$

With

$$Q = \frac{\rho_{gas}}{\rho_{melt}} \tag{2.38}$$

This equation is evaluated for different materials at a relative velocity v_{rel}=50m/s and a theoretical half sheet thickness h_f=0,1mm in figure 2.17. The higher the wave number and the higher the growth factor, the easier a material is supposed to be atomized (the less energy we need to achieve the wanted particle sizes).

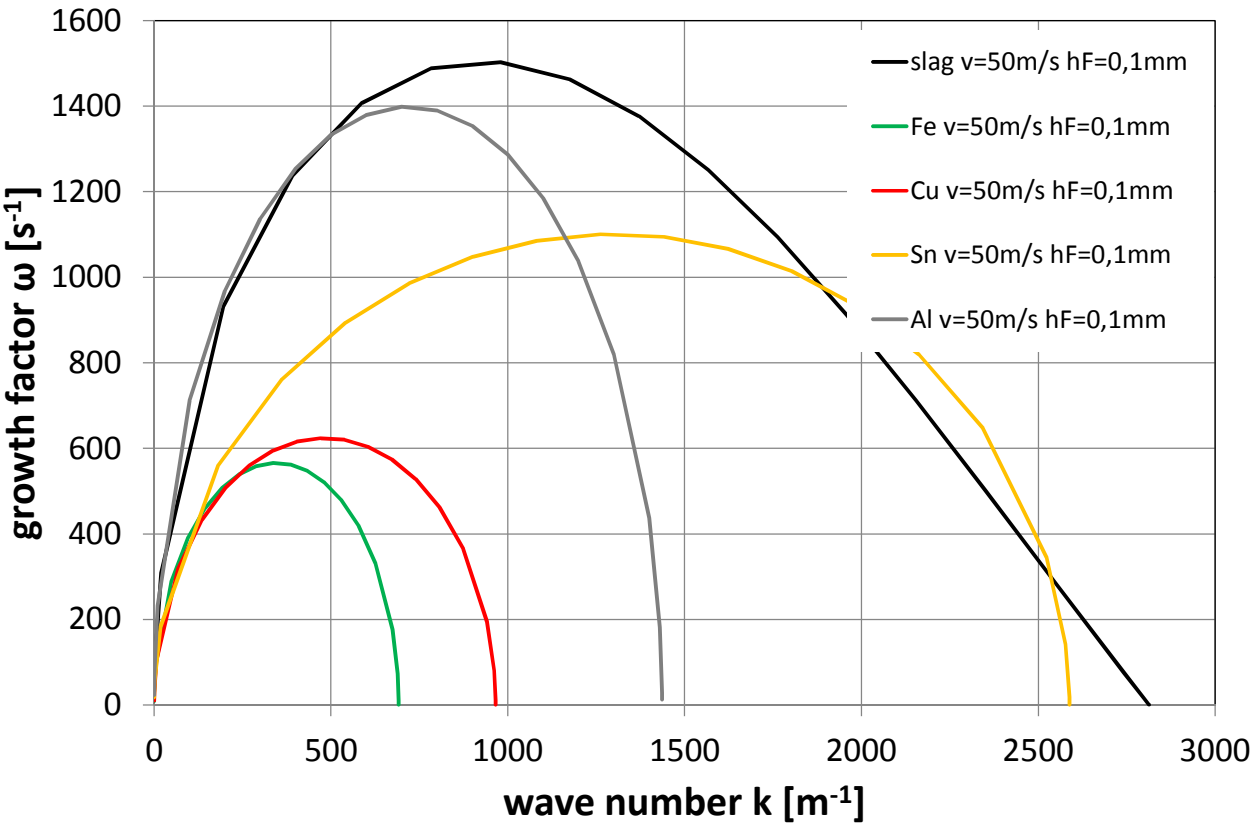

Figure 2.17: Influence of material properties on wave number and growth rate of a melt sheet with thickness h_F=0,1mm, relative velocity at the melt/gas interface v_{rel}=50 m/s; material properties to be found in chapter 6.

In figure 2.18, the influence of sheet thickness on maximum growth rate and corresponding wave number is shown. Apparently, sheet thickness does not chance the most unstable wave number, while its maximum growth rate resulting on more voluminous ligaments.

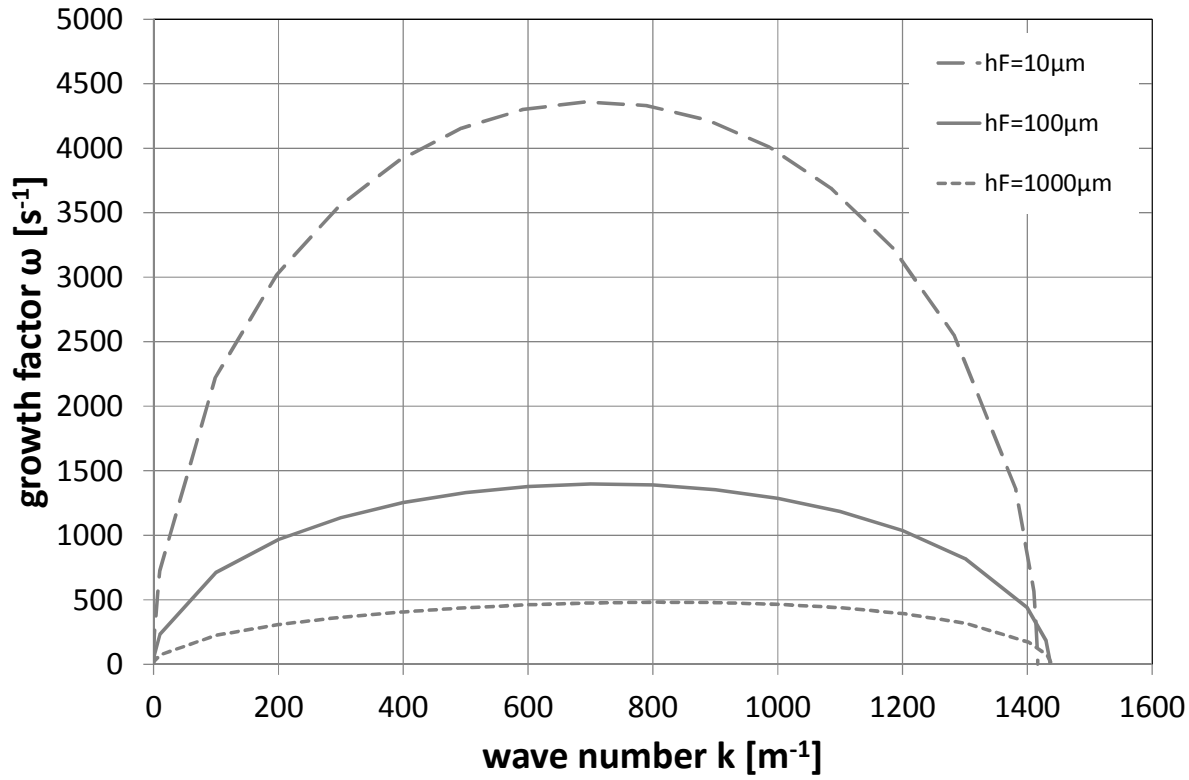

Figure 2.18: Influence of aluminium sheet thickness on wave number and growth rate of the most unstable wave; relative velocity v_{rel}=50 m/s, air temperature T_{gas}=400°C

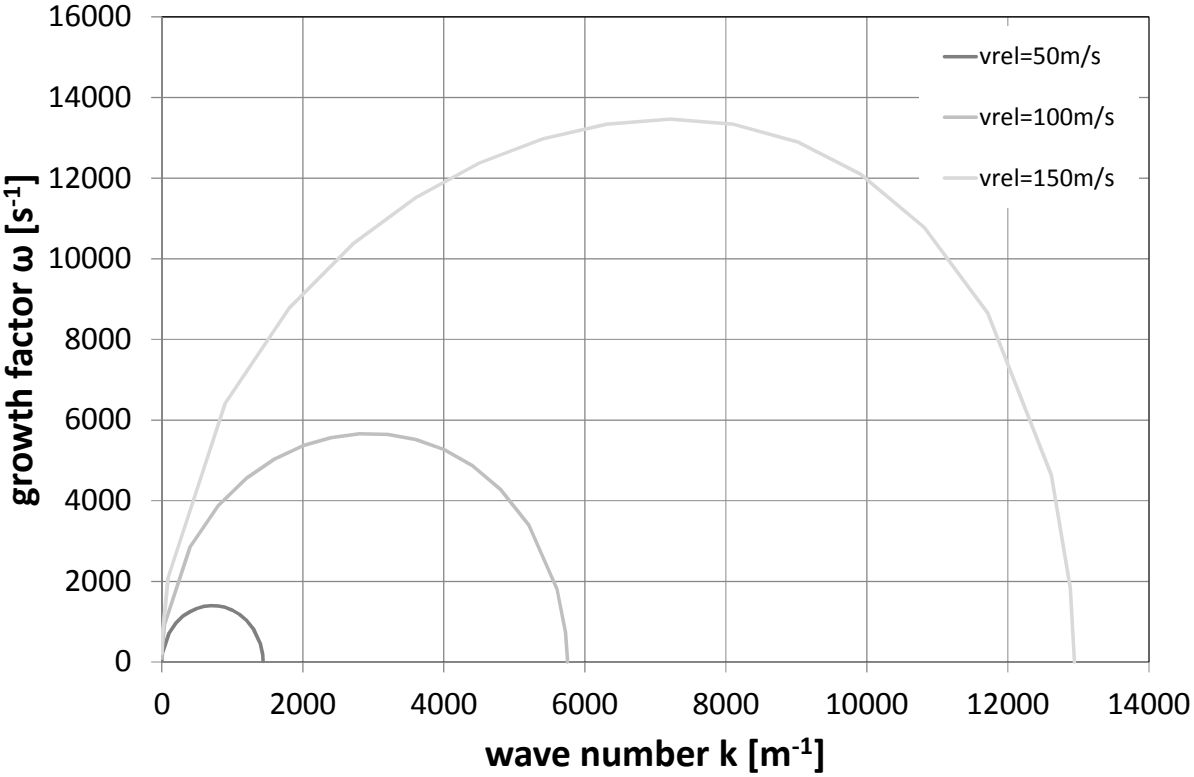

Figure 2.19: Influence of relative velocity on wave number and growth rate of the most unstable wave of an aluminium sheet, half sheet thickness h_F=100µm, air temperature T_{gas}=400°C

In figure 2.19, the influence of relative velocity on growth rate and wave number is shown. They both strongly increase with relative velocity (all other conditions being kept constant). A high relative velocity at the melt/gas interface strongly supports primary breakup.

Figure 2.20 shows the influence of melt viscosity on wave number and growth rate (slag, v_{rel}=50 m/s). As slag temperature decreases (from 1850°C to 1400°C), viscosity increases from 0,1 Pas to 0,9 Pas. A theoretical calculation for η_{melt}=0,001 is added to the picture to compare with viscosities of metal melts. Maximum growth rate and maximum wave number are both decreasing with increasing viscosity, but the influence becomes important only at high values of η_{melt}.

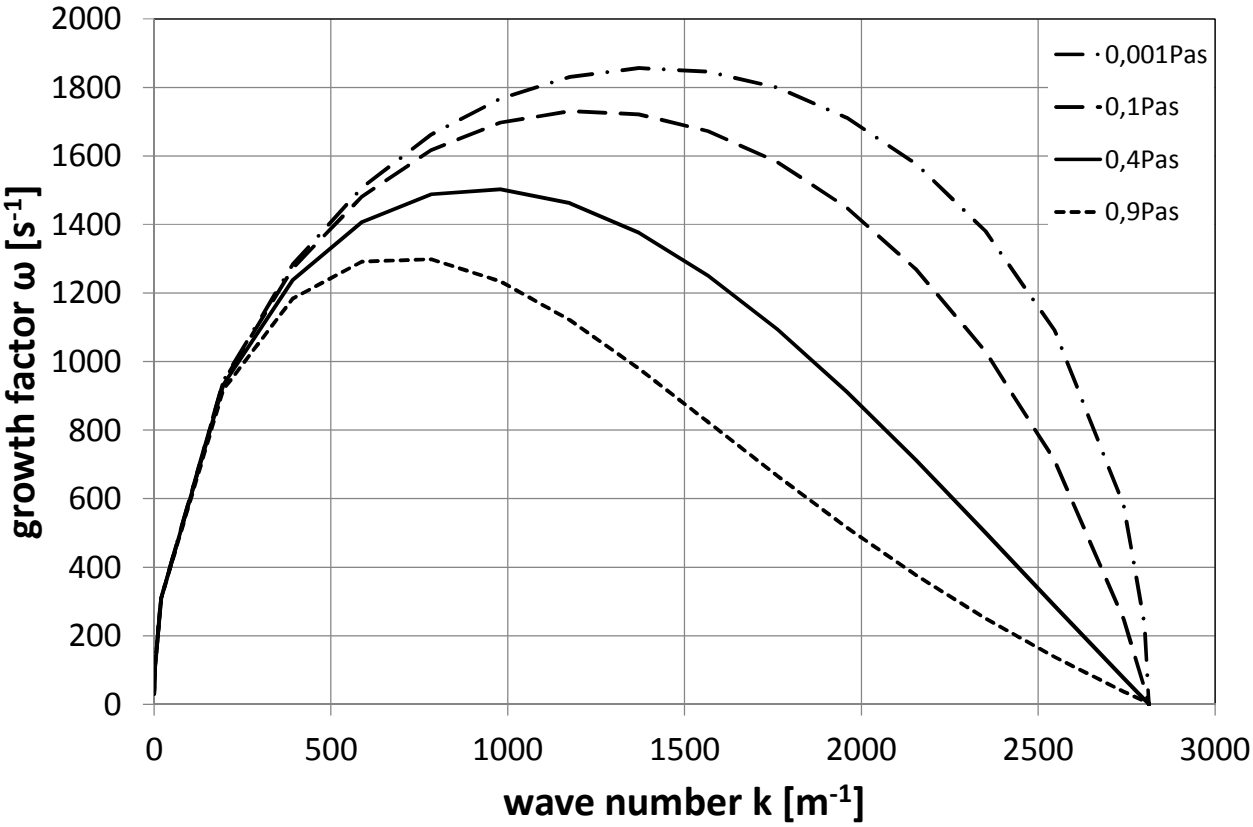

Figure 2.20: Influence of viscosity on wave number and growth rate

Drop sizes emerging from sheet breakup

As there is a main difference between the two cases, it is obvious to distinguish between long wave and short wave breakup. In the case of long waves (small Weber numbers, two ligaments per wavelength), the resulting ligament diameter can be calculated from local half sheet thickness at breakup, h_F, as follows:

$$D_L = \sqrt{\frac{8h_F}{k_{max}}} \tag{2.39}$$

For short waves, (high Weber numbers, one ligament per wavelength), ligament diameter will be:

$$D_L = \sqrt{\frac{16h_F}{k_{max}}} \tag{2.40}$$

As shown above, the theoretical drop size diameter can be determined from ligament diameter:

$$d = \left(\frac{3\pi}{\sqrt{2}}\right)^{\frac{1}{3}} D_L \left(1 + \frac{3\eta_L}{(\rho_L \sigma d_L)^{\frac{1}{2}}}\right)^{\frac{1}{6}} = 1{,}88 D_L (1 + 3Oh)^{\frac{1}{6}} \tag{2.29}$$

For low viscositiy melts, Ohnesorge number is very small and the relation reduces to:

$$d = 1{,}88 D_L \tag{2.41}$$

This relation is attributed to Lord Rayleigh [RAY1878].

Sheet breakup model of Dombrowski and Johns

For the sake of completeness, also the model of Dombrowski and Johns, established in the year 1963, is presented here [DOM1963]. With the same method of linear stability analysis, they derived as follows for the ligament diameter D_L:

$$D_L = 0{,}9614 \left(\frac{K^2\sigma^2}{\rho_{gas}\rho_{melt}v_{rel}^4}\right)^{\frac{1}{6}} \left(1 + 2{,}60\eta_L * \sqrt[3]{\frac{K\rho_{gas}^4 v_{rel}^7}{72\rho_{melt}^2\sigma^5}}\right)^{\frac{1}{5}} \tag{2.42}$$

K is a function of the half sheet thickness h_F and the melt sheet intact length x_{BU}:

$$K = 2h_F x_{BU} \tag{2.43}$$

Determination of the melt sheet intact length

The melt sheet intact length x_{BU} can be determined experimentally, as was done e.g. by Arai and Hashimoto [ARA1985], who measured breakup frequency and breakup length of thin liquid sheets in a co-current high speed gas stream. They determined for the liquid sheet intact length:

$$\frac{x_{BU}}{h_F} = 3{,}88 \left(\frac{h_F}{a_1}\right)^{-0{,}5} We_{GL}^{-0{,}5} Re_L^{0{,}6} \tag{2.44}$$

With

a_1 [m]=0,2*10^{-3}

and

$$We_{GL} = \frac{h_F \rho_{gas} (v_{gas} - v_{liq})^2}{\sigma} \tag{2.45}$$

$$Re_L = \frac{2h_F v_{liq}}{v_{liq}} \tag{2.46}$$

Estimation of the half sheet thickness after Gretzinger and Marshall

Ünal [ÜNA1987] used the following equation for the estimation of the half sheet thickness h_F at the position where the gas meets the metal. This quantity was derived from Gretzinger and Marshall [GRE1961]:

$$h_F = \frac{1}{2}\left(\frac{\eta_{melt}\dot{m}}{20\rho_{melt}^2 g\pi D}\right)^{\frac{1}{3}} \qquad (2.47)$$

Figure 2.21 shows the influence of nozzle diameter on sheet thickness for water at a mass flow rate ṁ=100 kg/h. With increasing nozzle diameter, sheet thickness decreases (left picture). The right picture shows the influence of mass flow rate on sheet thickness for different materials. Apparently, thickness increases with melt viscosity and decreases with melt density. Hence, sheet thicknesses for slag are one order of magnitude higher than the others. Also water sheets are thicker than melt sheets due to the low density of water, while tin sheets are very thin (relatively low viscosity, high density).

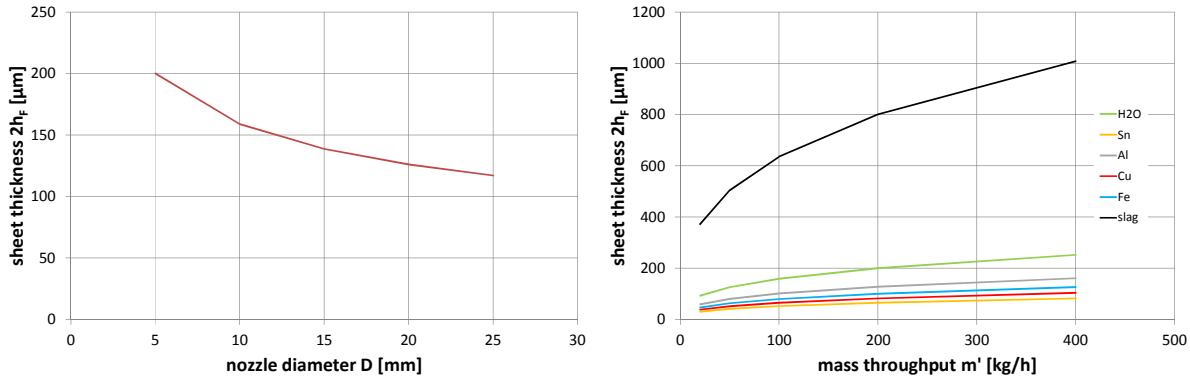

Figure 2.21. Water sheet thicknesses for a prefilming atomizer according to Ünal [UNA1987] for varying nozzle diameters; mass flow rate m'=100kg/h (left picture). Sheet thickness for different materials as a function of mass flow rate; nozzle diameter D=10mm (right picture)

Applications of Senecal's model for the estimation of ligament diameter in sheet breakup:

In the following, two commonly used applications of the twin fluid atomization process are described with the sheet breakup model of Senecal et al.: On the one hand, we assume that the sheet has got the shape of a cylinder, on the other hand, a conically shaped primary sheet formation is described (see figure 2.22).

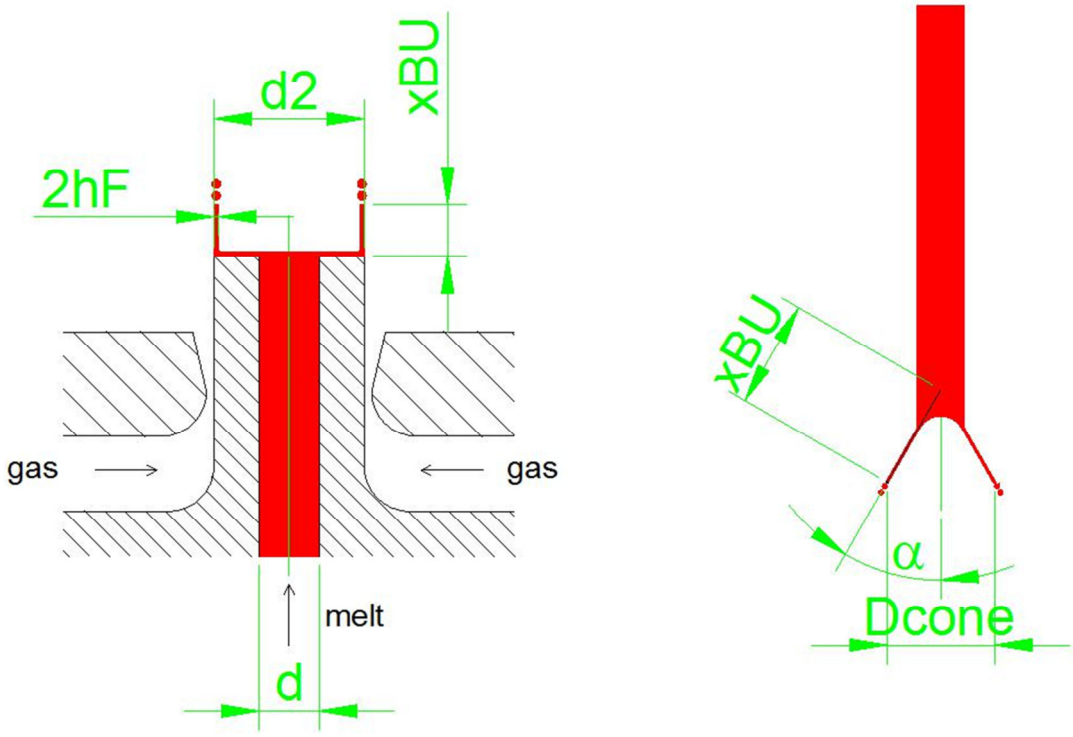

Fig. 2.22: Cylindrical (left picture) and conical sheet breakup (right picture)

a) Breakup of a cylindrical sheet

Mass flow in the sheet can be calculated as follows:

$$\dot{m}_{melt} = 2h_F v_{sheet} d_2 \pi \rho_{melt} \tag{2.48}$$

The maximum growth rate ω_{max} reveals, how many times per second a ligament is emerging from the sheet. Hence, the melt mass flow has to be equal to:

- in the case of short wave breakup:

$$\dot{m}_{melt} = \rho_{melt} d_2 \pi \frac{D_L^2 \pi}{4} \omega_{max} \tag{2.49}$$

- in the case of long wave breakup:

$$\dot{m}_{melt} = \rho_{melt} d_2 \pi \frac{D_L^2 \pi}{2} \omega_{max} \tag{2.50}$$

With the equations for ligament diameter (2.39 and 2.40) we can calculate the sheet velocity v_{sheet} and half sheet thickness h_F:

$$v_{sheet} = 2\pi \frac{\omega_{max}}{k_{max}} \tag{2.51}$$

$$h_F = \frac{1}{4\pi} \frac{\dot{m}_{melt}}{\rho_{melt}} \frac{1}{d_{cyl}\pi} \frac{k_{max}}{\omega_{max}} \tag{2.52}$$

For the calculation of the dispersion relation $\omega=\omega(k)$ to find the maximum growth rate ω_{max} and the corresponding wave number k_{max}, it is necessary to do a first estimation of the sheet half thickness h_F. With the values of k_{max} and ω_{max}, a new half sheet thickness h_F can be calculated

with equation (2.52). Hence, an iterative solution for half sheet thickness and maximum growth rate and wave number can be achieved.

Finally, equation (2.53) provided by Dombrowski and Johns [DOM1963] gives us the breakup length:

$$x_{BU} = v_{sheet}\tau = 12\frac{v_{sheet}}{\omega_{max}} \tag{2.53}$$

b) Breakup of a Conical Sheet following Senecal's Model

If we have a conical sheet, cone diameter is geometrically depending on breakup length and cone angle:

$$D_{cone} = x_{BU}2sin\alpha = 12\frac{v_{sheet}}{\omega_{max}}2sin\alpha \tag{2.54}$$

Mass balance leads to the calculation of the sheet thickness where breakup occurs. In the case of short wave breakup (one ligament per wavelength), we use:

$$\dot{m}_{melt} = \rho_{melt}D_{cone}\pi D_L^2\frac{\pi}{4}\omega_{max} = D_{cone}\pi 2h_F v_{sheet}\rho_{melt} \tag{2.55}$$

In the case of long wave breakup, we use:

$$\dot{m}_{melt} = \rho_{melt}D_{cone}\pi D_L^2\frac{\pi}{2}\omega_{max} = D_{cone}\pi 2h_F v_{sheet}\rho_{melt} \tag{2.56}$$

Dombrowski and Johns' relation between sheet velocity and wave growth parameters can also be used here:

$$v_{sheet} = 2\pi\frac{\omega_{max}}{k_{max}} \tag{2.51}$$

This leads to the diameter of the cone at breakup:

$$D_{cone} = \frac{48\pi}{k_{max}}sin\alpha \tag{2.57}$$

And finally, the calculation of the sheet half thickness:

$$h_F = \frac{1}{192\pi^3 sin\alpha}\frac{\dot{m}_{melt}}{\rho_{melt}}\frac{k_{max}^2}{\omega_{max}} \tag{2.58}$$

2.3. Ligament Breakup

After its formation, the ligament breaks down into droplets. For fluids of low viscosity, we expect Rayleigh breakup mechanism, and breakup time is only influenced by ligament diameter, liquid density and surface tension [ROD1995]:

$$t_{BU,L} = 1{,}95\sqrt{\frac{D_L^3\rho_{melt}}{\sigma}} \tag{2.59}$$

A much more sophisticated description of the phenomena around Rayleigh breakup can be found in [KOW1996] and [KUL1991].

Assuming that ligament breakup is governed by viscosity, we expect the breakup time to be [ROD1995]:

$$t_{BU,L} = 7{,}05\,\frac{\eta_{melt} D_L}{\sigma} \tag{2.60}$$

Table 2.4 shows the characteristic breakup time for a melt ligament with a diameter D_L=100µm for different liquids. Apparently, ligament breakup time for slag is one order of magnitude higher than for "normal" liquids.

Table 2.4: Ligament breakup time of a cylinder with diameter D_L=100µm for different liquids

fluid	$t_{BU,L}$ [µs]
water	81
tin	81
aluminium	35
copper	53
iron	42
slag	1379

2.4. Secondary Breakup

Following the primary atomization process, the droplet undergoes several different physical processes, which are influenced by one another. These are:

- droplet break-up due to the drag forces between gas and liquid
- acceleration, also due to the drag forces
- spheroidisation, due to surface tension forces
- cooling and solidification
- oxidation

The duration of these processes can be expressed by characteristic times:

- ➔ How long does it take for a droplet to break up into smaller particles?
- ➔ How long do we have conditions, where breakup is possible?
- ➔ How long does the droplet need to spheroidise?
- ➔ When is the droplet solidified so it cannot breakup or deform anymore
- ➔ How long does it take to build a significant oxide layer on the droplet surface?

In the following, the theoretical background to answer these questions is discussed. Due to the complexity of the topic, oxidation cannot be involved in the considerations.

2.4.1. Conditions for Droplet Breakup

To understand droplet breakup, it is necessary to distinguish between different breakup modes. We build the Weber number with relative velocity between gas and droplet and the gas density as follows:

$$We_{rel} = \frac{d_{drop}(v_{gas} - v_{drop})^2 \rho_{gas}}{\sigma} \tag{2.61}$$

And the droplet Ohnesorge number

$$Oh = \frac{\eta_{melt}}{\sqrt{d_{drop} \rho_{melt} \sigma}} \tag{2.62}$$

Amongst others, Faeth et al. [FAE1995] did experiments on droplet breakup by varying droplet Weber number and Ohnesorge number and found that for low Ohnesorge numbers (Oh<0,1), only Weber number is responsible for discrimination of the break-up regime. At higher Ohnesorge numbers – which means that liquid viscosity becomes more important compared to surface tension forces and/or external drag forces, we see that higher Weber numbers are needed to achieve break-up (figure 2.24).

At very low Weber numbers (We<1), deformation (<10%) can be neglected. No breakup will occure and a non-spherical droplet will spheroidise at these very low Weber numbers. With increasing We (1<We<12), deformation increases, droplets are oscillating and eventually, a process called “twinning” (or vibrational breakup) might occur. {In earlier times, this was one of the common ideas on how the moon was created: as a part of the still entirely liquid earth.}

At even higher Weber numbers (12<We<100), so-called “bag breakup” occurs (see figure 2.25), while at We>100, we talk of shear or stripping breakup. Several additional breakup modes can be distinguished (see e.g. [JOS1999]), which will not be discussed here.

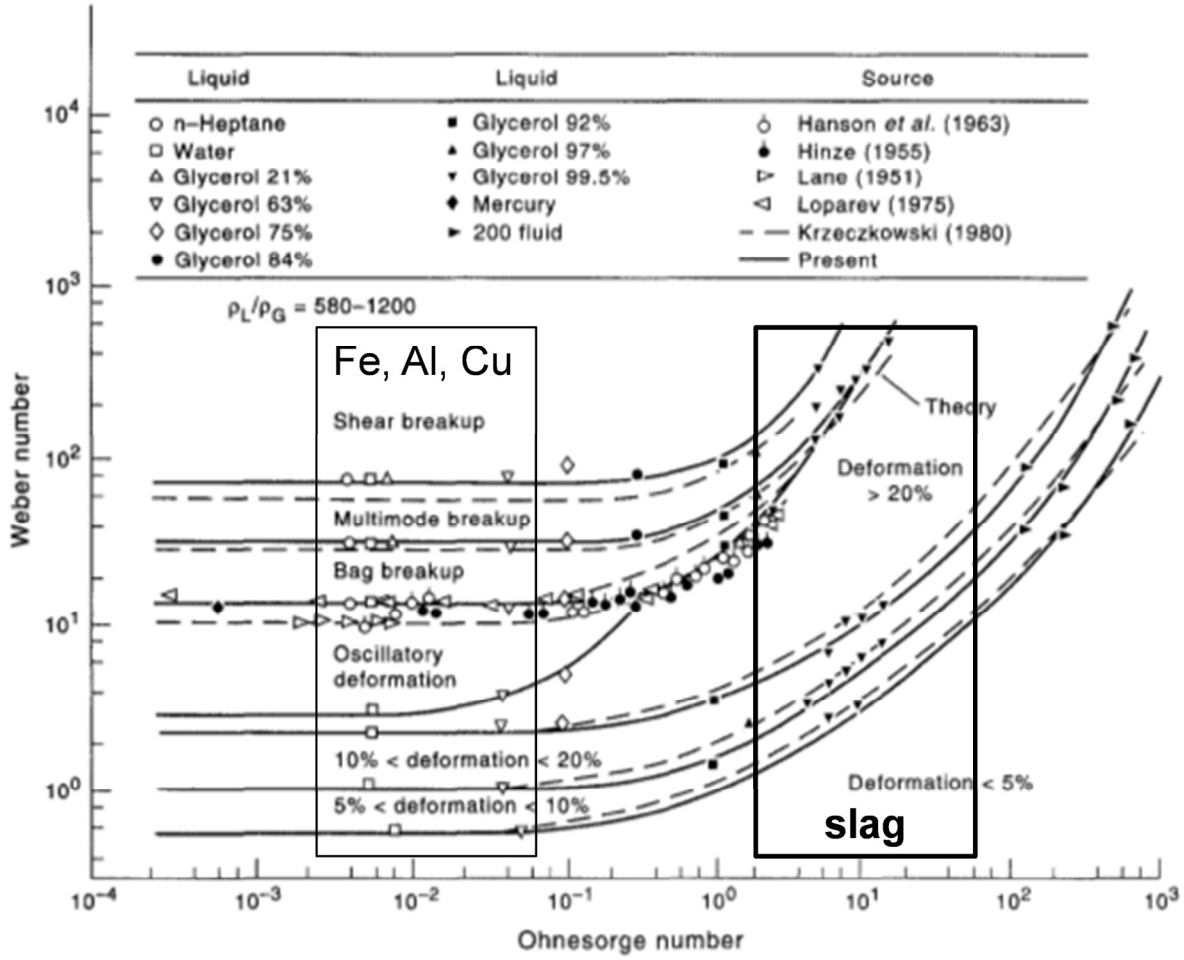

Figure 2.24: Break-up regimes for varying Ohnesorge and Weber numbers; the atomizer case studies discussed in chapter 3 (aluminium, iron) work in the range of $10^{-3}<Oh<10^{-1}$; if we consider slag as liquid, Ohnesorge numbers are three orders of magnitude higher

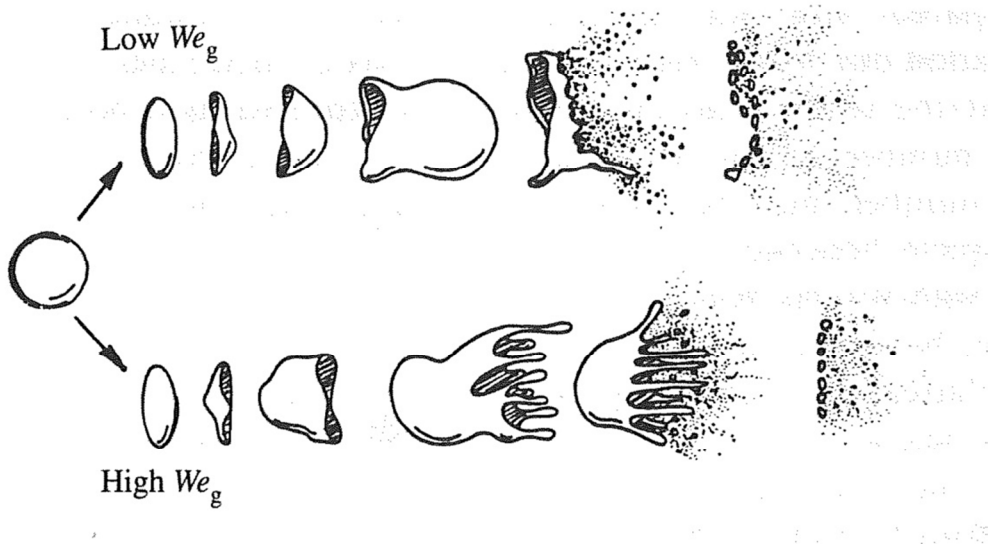

Figure 2.25: Schematic view of bag breakup (low Weber number, upper picture) and shear breakup (high Weber number); taken from [YUL1994]

2.4.2. Breakup Time

The break-up time of a droplet t_{BU} describes the time a droplet needs to deform and disintegrate into smaller droplets.

Applying a force model on the droplet, Gordon found that the time it takes for the droplet to disintegrate can be described by the following equation [GOR1959]:

$$\frac{2(16\eta_{melt})^2}{(\rho_{gas}v_{rel}^2-16\frac{\sigma}{d_{drop}})} = \frac{16\eta_{melt}t_{BU}}{\rho_{melt}d_{drop}^2} - 1 + e^{-\left(\frac{16\eta_{melt}t_{BU}}{\rho_{melt}d_{drop}^2}\right)} \tag{2.63}$$

Apparently, the equation can only be solved when the droplet/gas Weber-number is higher than 16.

$$We = \frac{\rho_{gas}d_{drop}v_{rel}^2}{\sigma} > 16 \tag{2.64}$$

In many publications, Wallis' relation [WAL1969] is cited – as also shown by Faeth et al. (see figure 2.24), droplet breakup starts in case We>12 for sudden accelerations, while, in the case of constant acceleration, higher Weber numbers (We>22) are necessary. A typical situation for the latter case is a rain drop falling due to gravity). Given the dynamic conditions in an atomizer, we expect to have something "between" constant and sudden acceleration, so a critical Weber number of 16 seems to be a reasonable choice.

Gordon also suggested a simplified relation, which, in his own words, is "never too small, max. 37% too high":

$$t_{BU} = \frac{2d_{drop}\rho_{melt}^{0,5}}{(\rho_{gas}v_{rel}^2-16\frac{\sigma}{d_{drop}})^{0,5}} + \frac{32\eta_{melt}}{(\rho_{gas}v_{rel}^2-16\frac{\sigma}{d_{drop}})} \tag{2.65}$$

The time a particle needs to deform to the critical value was also investigated by Naida [NAI1971], who established the following correlation for breakup time:

$$t_{BU} = 1{,}65\frac{d_{drop}}{v_{rel}}\sqrt{\frac{\rho_{melt}}{\rho_{gas}}} \tag{2.66}$$

while Faeth et al. [Faeth 1994] et al. suggested

$$t_{BU} = 5\frac{d_{drop}}{v_{rel}}\sqrt{\frac{\rho_{melt}}{\rho_{gas}}} \tag{2.67}$$

It is interesting to know that break-up time is more or less independent of break-up mode; and also independent of Oh, as long as Oh<0,1, which is the case here, unless we use the material properties of slag for our calculations.

The TAB Method ("Taylor Analogy Breakup") for numerical calculation of spray droplet breakup was first presented by O'Rourke and Amsden [ORO1987]. According to this reference, breakup time for small Weber-numbers (bag breakup) is:

$$t_{BU} = \sqrt{3\frac{\rho_{liq}}{\rho_{gas}}}\frac{d_{drop}}{2v_{rel}} \tag{2.68}$$

For higher Weber-numbers ("stripping" or shear breakup), breakup time is:

$$t_{BU} = \pi\sqrt{\frac{d_{drop}^3 \rho_{liq}}{64\sigma}} \tag{2.69}$$

Exemplarily, break-up time for a water droplet in a high velocity gas stream (v_{rel}=100m/s) is shown in figure 2.26. The mathematically simple models of Naida and of Faeth do not take into account that – for aerodynamic conditions close to critical Weber-Number – break-up time increases with decreasing droplet diameter and becomes infinite for We=16, while the TAB method differentiates between bag breakup and shear breakup.

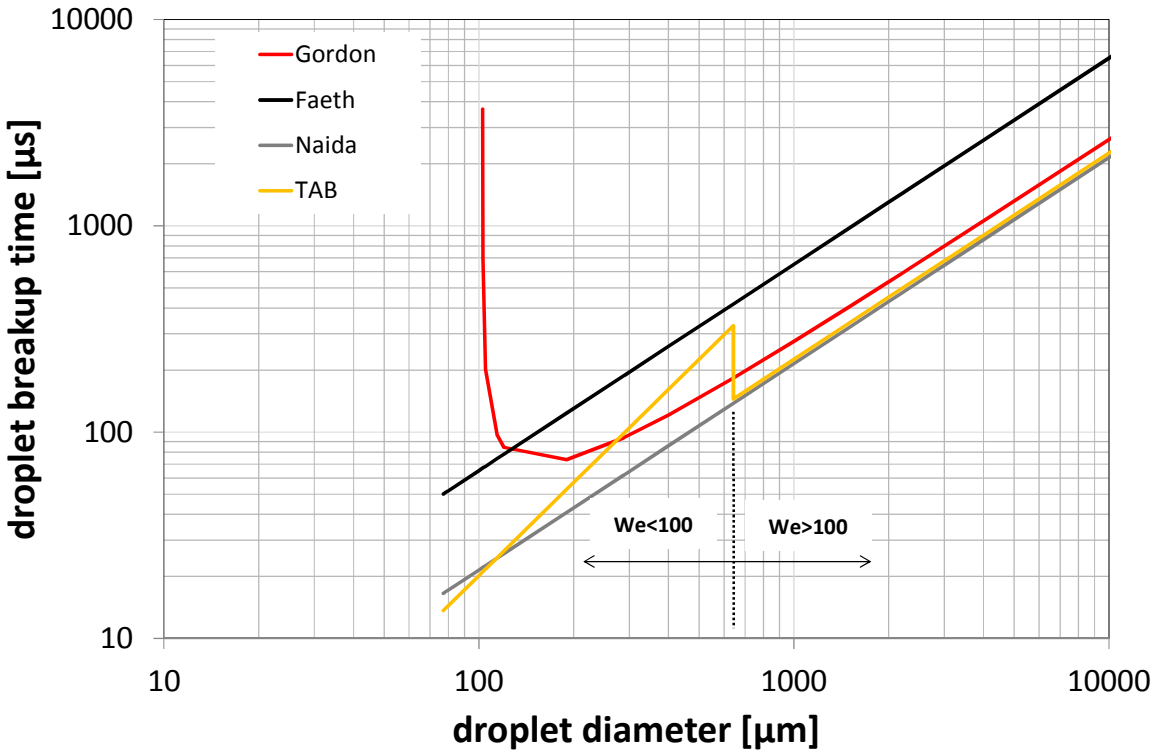

Figure 2.26: Different models of droplet break-up time as a function of primary droplet diameter: model calculations for the material system air/water at a relative velocity of 100m/s; Gordon's model is the only relation to include the increase of breakup time at Weber numbers around its critical value for breakup; the TAB method shows a discontinuity at the limit between bag and shear breakup

For analyzing secondary breakup in atomizer case studies 1, 2 and 3 in chapter 3, the simplified relation of Gordon (2.65) will be used for any calculations of the break-up time.

2.4.3. Breakup outcome in the form of secondary droplet sizes

Finally, droplet sizes resulting from droplet breakup are of interest. Based on experimental results on single droplets, Faeth et al. [FAE1995] suggested the following semi-empirical equation:

$$d_{50,sec} = \frac{7{,}44}{\left(\rho_{melt}\rho_{gas}\right)^{0{,}25}}\sqrt{\frac{\eta_{melt} d_0}{u_{rel}}} \tag{2.70}$$

The TAB Method distinguishes between bag breakup (including multimode breakup) and shear breakup as follows:

Bag/Multimode breakup (We_{gas}<100):

$$\frac{d_{50,sec}}{d_{50,prim}} = \frac{3}{7} \tag{2.71}$$

Shear breakup (We_{gas}>100):

$$\frac{d_{50,sec}}{d_{50,prim}} = \frac{6}{We} \tag{2.72}$$

This implies a jump in secondary drop size when there is a change in breakup mode. In "reality", we know that there are intermediate modes of droplet breakup which might need a more detailed examination. Furthermore, we see that in shear breakup mode, secondary drop size is independent of parent drop size.

Also the primary breakup model of Reitz (see chapter 2.2.1.) was applied on shear breakup. Results are in good agreement with the TAB method.

Secondary droplet diameter then is:

$$d_{50,sec} = 0{,}61\lambda_{max} \tag{2.73}$$

Chou and Faeth [CHO1998] examined bag breakup of droplets from organic liquids finding that it is necessary to distinguish between the droplets resulting from the bag ring and the one's resulting from the bag.

Volume percentage of the ring is at about 56% and the secondary droplet diameter follows the law:

$$\frac{d_{50,ring}}{d_{50,prim}} = 0{,}3 \tag{2.74}$$

The bag keeps the remaining part of the droplet volume (44%) and the resulting mean diameter is

$$\frac{d_{50,bag}}{d_{50,prim}} = 0{,}042 \tag{2.75}$$

All these results are exemplarily shown in figure 2.27 for liquid aluminium droplets in a hot air stream (400°C).

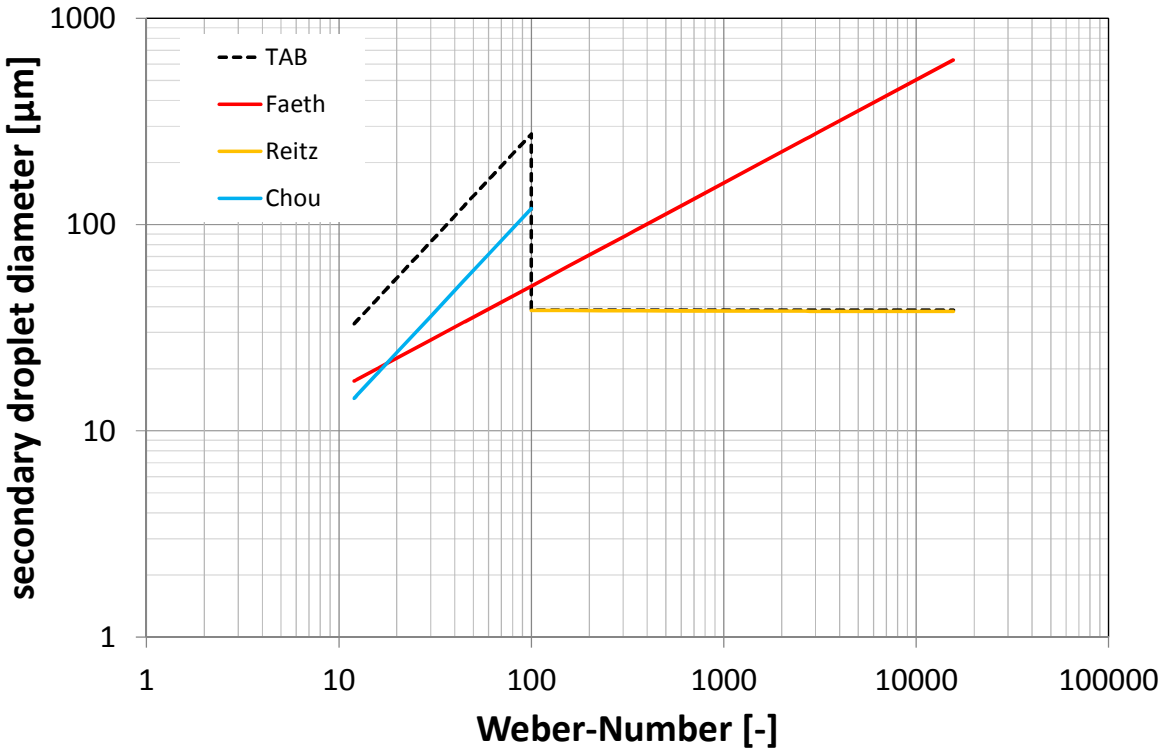

Figure 2.27: Secondary droplet size for aluminium droplets in a hot gas stream (400°C) following different models. The step at We=100 corresponds to a change in breakup mode from bag/multimude to shear breakup.

2.4.4. Droplet Acceleration

During atomization, the droplet starts with a very low velocity (e.g. v_{drop}=0 near the nozzle tip) and is accelerated due to the drag force of the gas. Droplet break-up is only possible, when the critical Weber Number is still high enough (see figure 2.24). The acceleration time t_{acc} is defined as the time during which We>16 is fulfilled.

As described in chapter 2.1.4., the gas velocity can be described by the following equation:

$$v_{gas} = v_{gas,0} e^{-\frac{z}{\lambda_v}} \tag{2.76}$$

With

$$\lambda_v = a_1 v_{gas,0}^n \; ; a_1 = 3{,}04 * 10^{-4} \text{ and } n = 1{,}24 \tag{2.77}$$

Considering that gravity, Basset, Saffmann and Magnus forces can be neglected [DEL2000], only drag force is important to describe the acceleration of the droplet:

$$\frac{\partial v_{drop}}{\partial t} = \frac{3 C_D}{4 d_{drop}} \frac{\rho_{gas}}{\rho_{melt}} (v_{gas} - v_{drop}) \left| v_{gas} - v_{drop} \right| \tag{2.78}$$

The drag force coefficient C_D can be taken from figure 2.28. Approximating the droplet as a perfect, accelerating sphere and that the Reynolds number is higher than 500, C_D is set to the

value 0,44. The latter assumption is true for metal melts when breakup is still possible (We>16), but becomes more and more imprecise at smaller relative velocities.

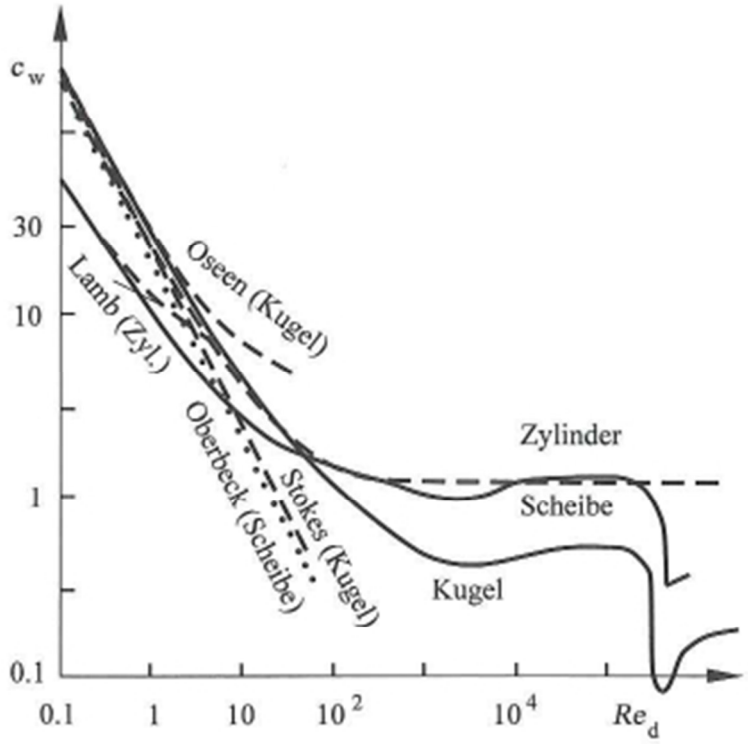

Figure 2.28: Drag coefficient as a function of the Reynolds number Re [PRA1969]; the Reynolds number has to be established with the relative velocity $v_{rel}=v_{gas}-v_{drop}$ and the gas density and viscosity

[GRA2012] developed an easy to use calculation routine for the evolution of the relative velocity between gas and droplet.

In the following, a numerical example how this can be done, is demonstrated:

With chosen initial conditions (water/air, v_{gas}=100m/s, $v_{droplet}$=0m/s, $d_{droplet}$=200µm), the decrease of the gas velocity and the increase of the droplet velocity is shown in figure 2.29. Weber (left picture) and Reynolds number (right picture) for these conditions are plotted in figure 2.30. We can see that at 1300 µs, We number becomes lower than 16. No further breakup is possible.

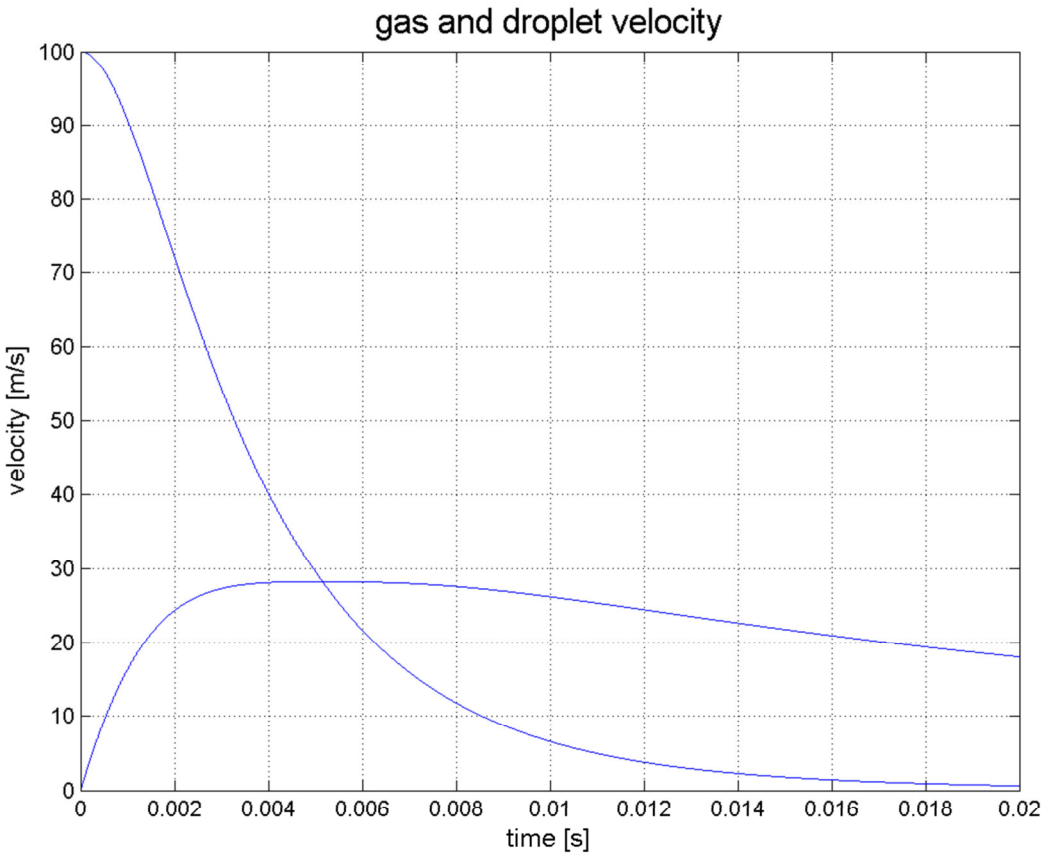

Figure 2.29: Gas and droplet velocity (system air water), initial gas velocity=100m/s, droplet size is 200 µm

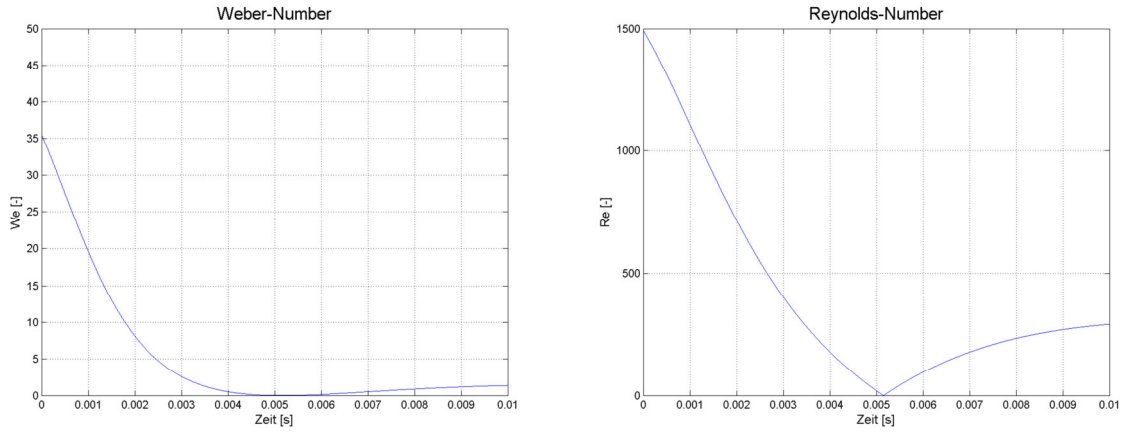

Figure 2.30: Evolution of the droplet Weber number (left picture) and the Reynolds number (right picture) in a gas field with decreasing velocity according to equations (2.76 – 2.78)

2.4.5. Droplet Spheroidisation

A 4-force model, as first presented by Rao [RAO1972, RAO1973], was adapted for our purposes:

$$\sum Forces = IF + VF + SF + DF = 0 \qquad (2.79)$$

With:

Inertia force:

$$IF = \frac{1}{2} m_{drop} \frac{\partial^2 L}{\partial t^2} \tag{2.80}$$

Viscous force:

$$VF = \frac{V_{drop}\eta_{melt}}{2L^2}\left(\sqrt{1+\frac{8\pi L^3}{V_{drop}}}-1\right)\frac{\partial L}{\partial t} \tag{2.81}$$

Surface tension force:

$$SF = \frac{V_{drop}\sigma}{2L^2}\left(-\frac{1}{2L^2}+\sqrt{\frac{\pi}{2V_{drop}L}}\right) \tag{2.82}$$

Knowing that spheroidisation is only possible in the case of low drag forces (We<1 as shown in figure 2.24.), the drag forces can be neglected:

Drag force:

$$DF = 0 \tag{2.83}$$

Hence, equation (2.79) can be expressed as:

$$\frac{1}{2} m_{drop} \frac{\partial^2 L}{\partial t^2} + \frac{V_{drop}\eta_{melt}}{2L^2}\left(\sqrt{1+\frac{8\pi L^3}{V_{drop}}}-1\right)\frac{\partial L}{\partial t} + \frac{V_{drop}\sigma}{2L^2}\left(-\frac{1}{2L^2}+\sqrt{\frac{\pi}{2V_{drop}L}}\right) = 0 \tag{2.84}$$

Rao's model describes the "spheroidisation" of a cylinder with an initial length L_0 at an initial diameter D_0 with L_0/D_0=5 (the shape of a cylindrical ligament formed from primary break-up mechanisms). From Rayleigh's relation (d_{drop}=1,88D_L), we are able to calculate the initial length-to-diameter ratio L_0/D_0 (2.85). The starting diameter D_0 in this process corresponds to the ligament diameter D_L. The final length and diameter L_{END} can be expressed as shown in equation (2.86) (see also figure 2.31).

$$\frac{L_0}{D_0} = \frac{2}{3} * 1{,}88^3 = 4{,}44 \tag{2.85}$$

$$\frac{L_{END}}{d_{drop}} = \sqrt[3]{\frac{2}{3}} \tag{2.86}$$

Final shape is a cylinder with L_∞/D_∞=1, while d_{drop} is the diameter of the sphere with the same volume as the cylinder. Rao defined the spheroidisation time as the time when the length reached 1/0,632 of its final length. Apparently, this model is not very exact, but is supposed to give a realistic order of magnitude for the spheroidisation process.

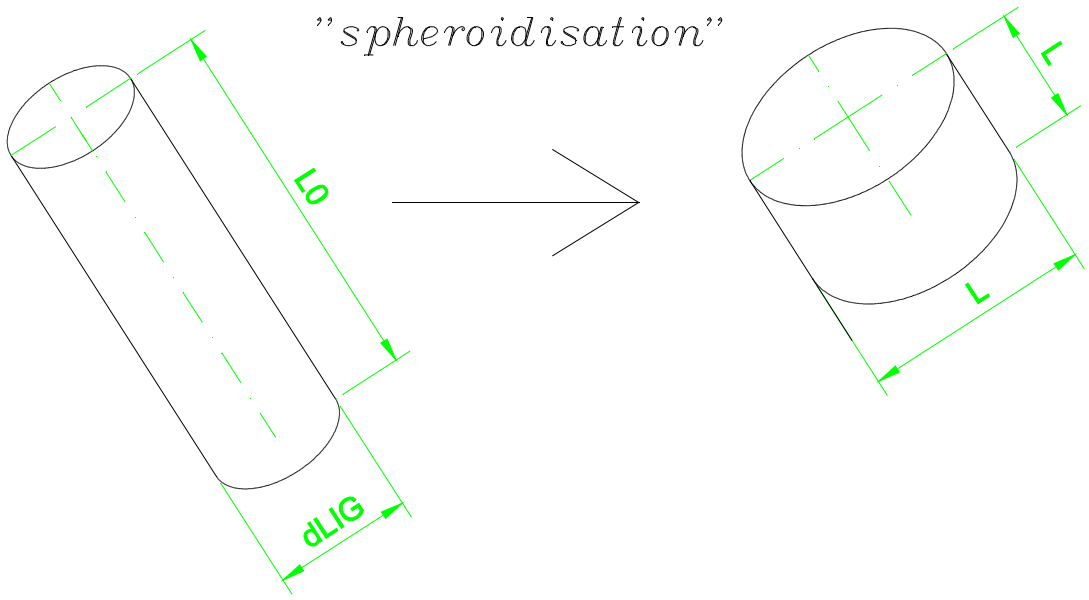

Figure 2.31: Spheroidisation process following the model of Rao [RAO1973]: Starting from a ligament with diameter d_{LIG} (taken from equation 2.22, 2.37 or 2.38) and initial length L_0, the cylinder oscillates until it reaches its final length and diameter L

Figure 2.32. (left picture) shows the spheroidisation process for a steel droplet with d_0=145µm. It can be seen that the length of the cylinder is fluctuating at a frequency of about 5200 Hz and it takes 7ms until the spherical condition is achieved. The right picture shows the spheroidisation process for a slag droplet with d_0=1000µm. Frequency is about 250 Hz and the spheroidisation time is compareable to the one of the steel droplet with about1/7 of the size. In the case of very high viscosities (e.g. slag right above its softening temperature, μ_{melt}>1Pas), the system will be overdamped and no oscillation occurs, but a slow "creeping" from cylinder to spherical shape will take place.

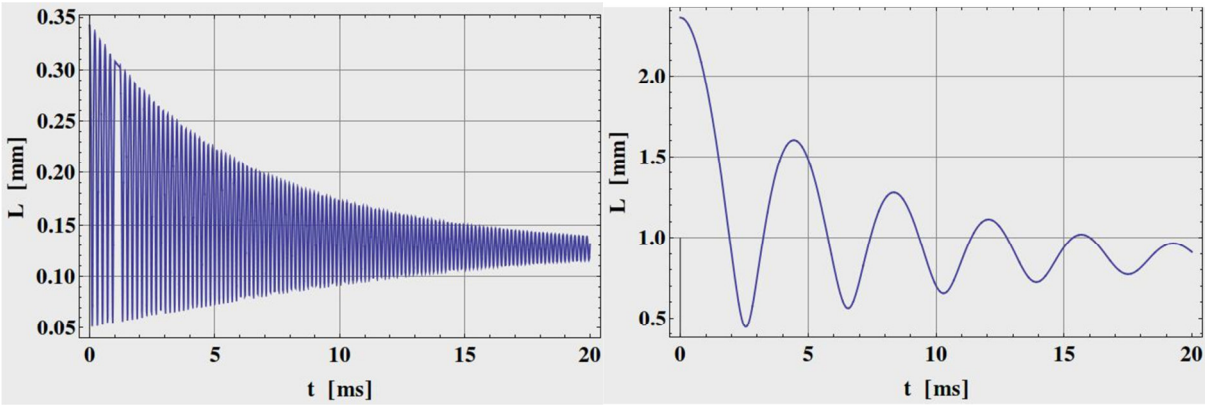

Figure 2.32: Two examples for the spheroidisation process: left picture shows the spheroidisation of a steel droplet with d_{end}=145µm, right picture shows the spheroidisation of a slag droplet with d_{end}=1000µm. The spheroidisation time for both is about 7ms, while the steel droplet is oscillating at a frequency which is about 20 times higher than the one for slag

Two other, simpler expressions to estimate spheroidisation time were suggested in earlier times.

Nichiporenko and Naida [NIC1967, NIC1968] did atomization trials with various melts such as copper, aluminium and lead finding the following relation:

$$t_{sph} = \frac{3}{4}\frac{\pi^2 \eta_{melt}}{V_{drop}\sigma}\left(\frac{1}{2}\right)^4 \left(d_{drop}^4 - D_{\mathrm{L}}^4\right) \tag{2.87}$$

Again, assuming that L_0/D_L=4,44 we see that D_L can be neglected and the formula becomes

$$t_{sph} = \frac{9\pi}{32}\frac{\eta_{melt} d_{drop}}{\sigma} \tag{2.88}$$

The viscosity plays the damping role in spheroidisation, so one would expect that a higher viscosity results in a decrease of the spheroidisation time. Nichiporenko and Naida pointed out, that their results are orders of magnitude below of what one would expect from atomization results, so this equation's value is only a historical one.

Yule et al. [YUL1982] empirically found the following relationship for spheroidization time of kerosene droplets:

$$t_{sph} = 0{,}1\varrho_{melt}\frac{d_{drop}^2}{\eta_{melt}} \tag{2.89}$$

This equation gives comparable results to the concept of Rao presented above, as long as it is only used for liquids with comparable surface tension (water, organic liquids), while its use for metal melts (high surface tension, high melt densities) is low.

In the following, the model of Rao is used for any calculations of spheroidisation time; a comparison of these three models for water drops is shown in figure 2.33.

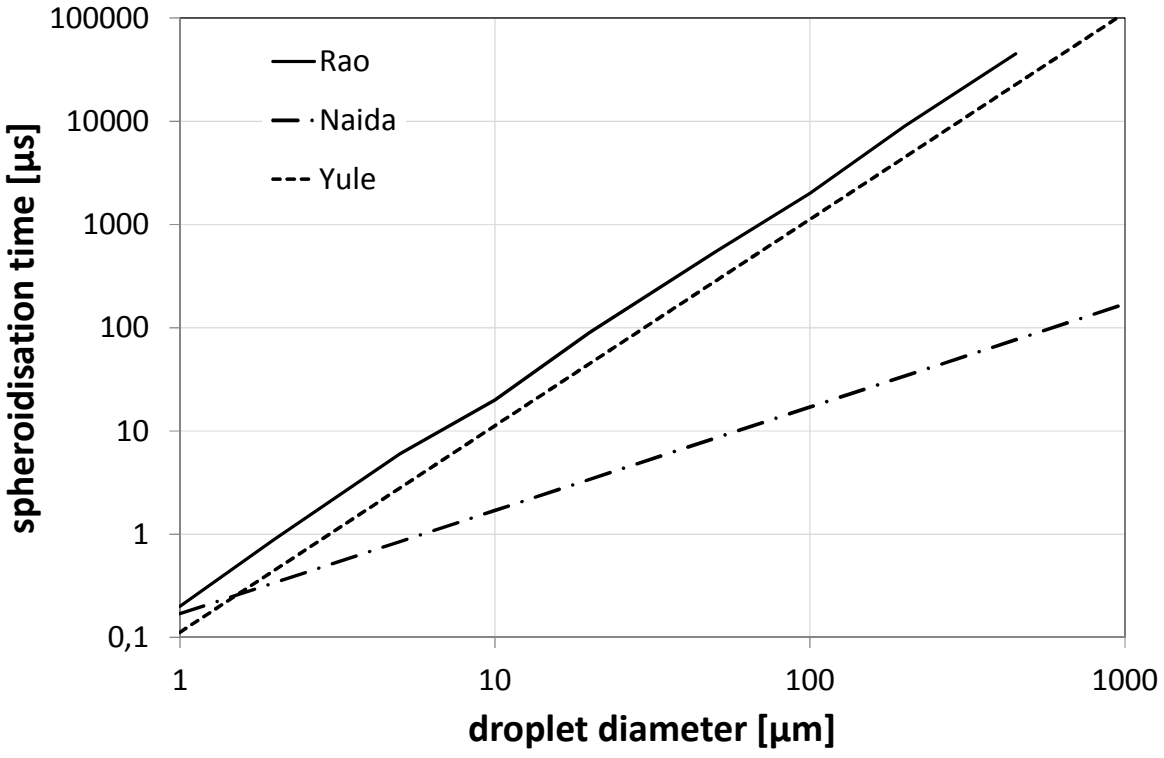

Figure 2.33: Spheroidisation time of water droplets – model based estimations as a function of droplet diameter

2.4.6. Droplet Cooling and Solidification

The following relations for cooling and solidification time are widely used and were first established by Nichiporenko and Naida [NIC1968]: The time needed to cool the melt droplet from its initial temperature to its solidification temperature is depending on metal properties, gas temperature and on the droplet initial temperature:

$$t_{cool} = \frac{d_{drop}\rho_{melt}c_{p,melt}}{6\alpha} ln\left[\frac{T_{melt}-T_{gas}}{T_{sol}-T_{gas}}\right] \tag{2.90}$$

Assuming that the thermal conductivity of the metal is high in relation to the heat transfer coefficient (Bi<<1), we have (in case Re<10^6 und Pr>0,5) forced convection and we get:

$$\alpha = \frac{\lambda_{gas}}{d_{drop}} Nu = \frac{\lambda_{gas}}{d_{drop}} (2{,}0 + 0{,}6Re^{0{,}5}Pr^{0{,}33}) \tag{2.91}$$

with

$$Pr = \frac{c_{p,gas}\eta_{gas}}{\lambda_{gas}} \tag{2.92}$$

The time the particle needs to solidify is calculated by

$$t_{sol} = \frac{d_{drop}\rho_{melt}}{6\alpha}\left[\frac{\Delta h_{melt}}{(T_{sol}-T_{gas})}\right] \tag{2.93}$$

$$t_{sol+cool} = \frac{d_{drop}\rho_{melt}}{6\alpha}\left[c_{p,melt} ln\left(\frac{T_{melt}-T_{gas}}{T_{sol}-T_{gas}}\right) + \frac{\Delta h_{melt}}{(T_{sol}-T_{gas})}\right] \tag{2.94}$$

Nichiporenko‘s model implies a constant heat transfer coefficient α. As α is decreasing when relative velocity is decreasing, we expect a higher cooling and solidification time when we include the – decreasing – relative velocity in the calculations. This was done – again – by Gratzer [GRA2012], who used the model presented above (chapter 2.3.4.) to calculate heat transfer coefficients.

Exemplarily, results are shown in figure 2.34 for the system aluminium/air. The heat transfer coefficient shows a minimum at 0,01 seconds (see figure 2.34b), corresponding to the moment where gas and droplet velocity are equal (v_{rel}=0). At 0,005 seconds (see figure 2.34d), droplet temperature is constant for 0,03 seconds – this is the time the droplet needs to solidify. It is also interesting to see that the thermal conductivity of melts is lower than the one of solid metals. Hence, the cooling rate shows some discontinuity at 0,035 seconds, where the solid state is achieved (figure 2.34c).

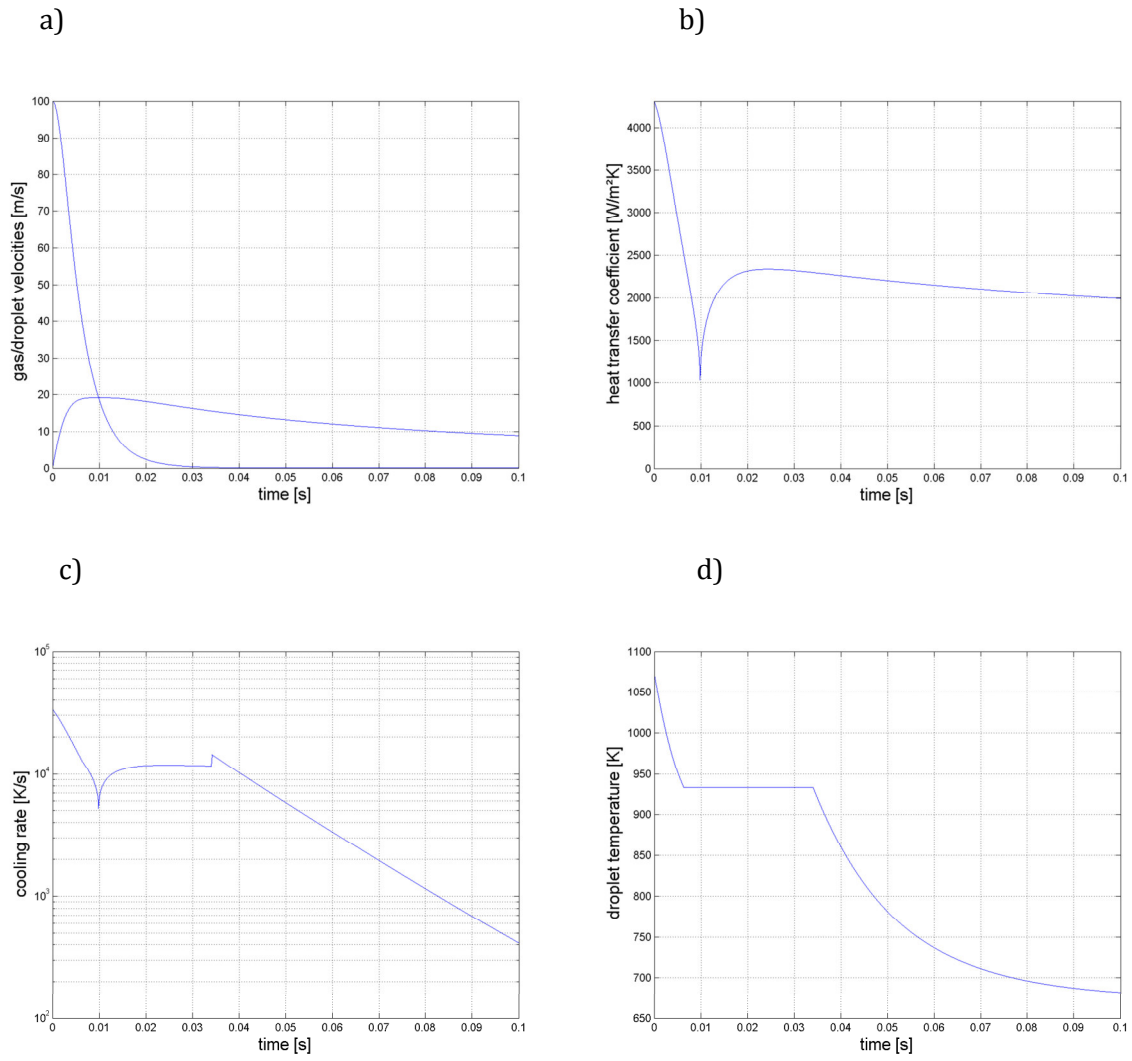

Figure 2.34: Cooling and solidification of an aluminium droplet in air with diameter d_{drop}=100µm, initial relative velocity between droplet and gas v_{rel}=100m/s, initial droplet temperature T_{melt}=800°C, gas temperature T_{gas}=400°C=const; a) gas and droplet velocity b) heat transfer coefficient c) cooling rate d) droplet temperature

For a whole range of particle sizes, a comparison is done between the models of Gratzer and Nichiporenko (figure2.35). For small particles, the two models are in good accordance, while for larger particles (when the heat exchange coefficient is decreasing), cooling and solidification takes place much slower.

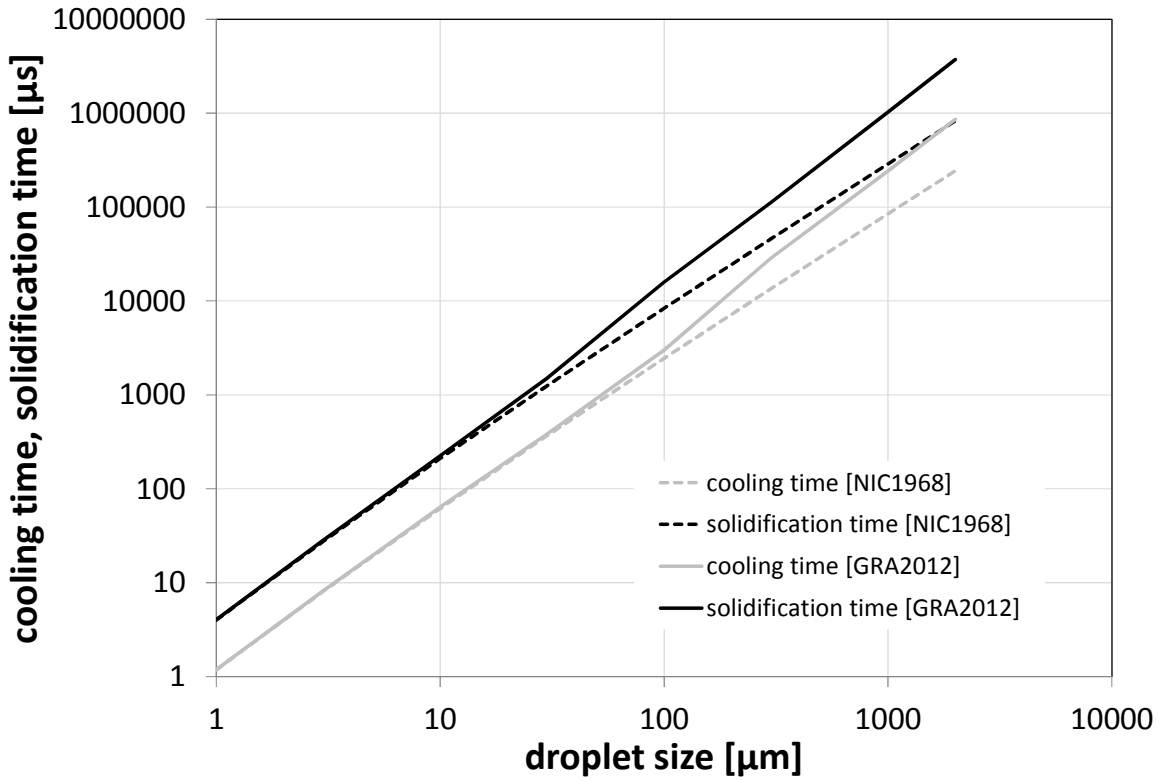

Figure 2.35: Cooling time and solidification time of aluminium droplets in air – comparison between the models of Gratzer and Nichiporenko; initial relative velocity v_{rel}=100 m/s, gas temperature T_{gas}=0°C, melt temperature T_{melt}=800°C

Still, one drawback of the model of Gratzer is that the droplet – also during the solidification process – is seen as a homogeneous sphere. Hence, side effects like nucleation, surface undercooling, recalescence etc. are neglected. More sophisticated models were established e.g. by Grant et al .[GRA1993] and Delplanque et al [DEL2000].

Furthermore, heat exchange between the atomizing gas and the surrounding gas is not included in the calculations, as well as the heat flow from the melt droplets to the atomizing gas.

3. Model Atomizer Case Studies

Three commonly used atomization systems are investigated with the model presented in chapter 2: A typical open jet nozzle is discussed in chapter 3.1. Material system is iron/air. In chapter 3.2., two different close-coupled nozzles, a prefilming and a direct nozzle, are compared for the material system aluminium/air.

3.1. Open jet atomization

3.1.1. Nozzle Geometry, Material System and Initial Conditions

The geometry of the atomization system is shown in figure 3.1, the corresponding geometrical details and the boundary conditions for the calculations are given in table 3.1.

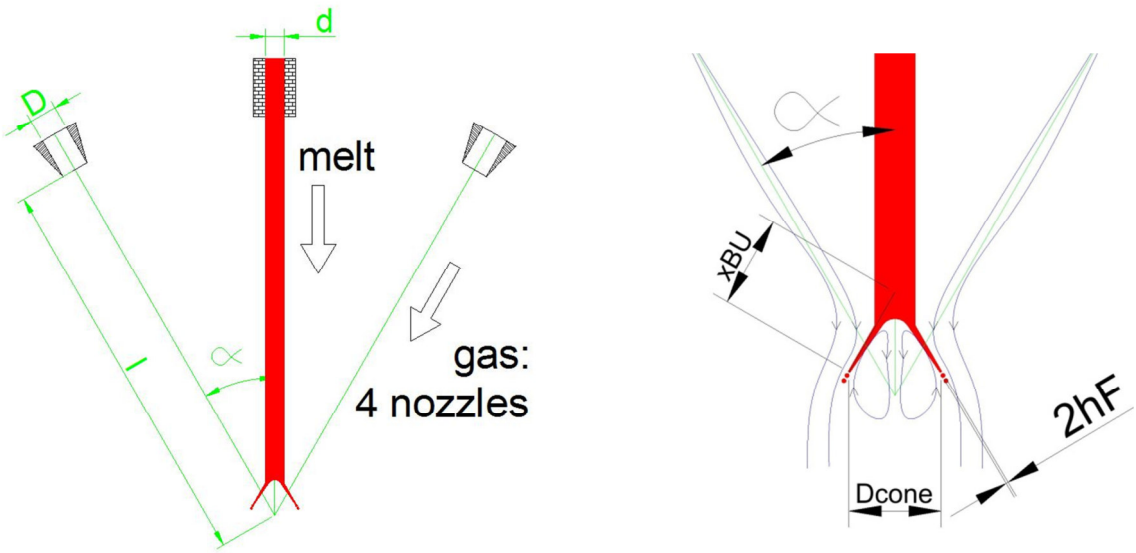

Figure 3.1: Open jet atomization: pressurized gas flows through 4 nozzles (diameter D) at an angle α to the vertical melt stream. Breakup position is at distance x from nozzle exit. According to See and Runkle [SEE1973] a conical sheet with a half opening angle α is formed. At position x_{BU}, the sheet, having a half sheet thickness h_F and a cone diameter D_{cone}, breaks into ligaments.

3.1.2. Critical Conditions

In the narrowest cross section (which is the gas exit for cylindrical nozzles), we achieve critical conditions which are calculated using equations 2.11-2.13 with Ma=1. Gas consumption is calculated using equation 2.3 (see table 3.2).

Table 3.1: Initial Conditions and Nozzle Geometry

AMBIENT CONDITIONS				
ambient pressure	p_1	[bar abs]	1	
ambient temperature	T_1	[°C]	200	
ambient gas density	ρ_1	[kg/m³]	0,74	

NOZZLE GEOMETRY				
gas nozzle diameter	D	[mm]	4,7	
gas cross section (4 nozzles)	A_{nozzle}	[mm²]	69,4	
distance gas nozzle//melt jet	l	[mm]	68	see fig. 3.1. left
gas flow half angle	α	[°]	30	
liquid jet diameter	d	[mm]	3,17	

INITIAL CONDITIONS - AIR				
gas reservoir pressure	p_0	[bar abs]	10	
gas reservoir temperature	T_0	[°C]	400	
gas density	ρ_0	[kg/m³]	5,18	
sonic velocity	a_0	[m/s]	520,4	

INITIAL CONDITIONS - STEEL				
melt production rate	m'_{melt}	[kg/h]	300	
melt temperature	T_{melt}	[°C]	1750	

Table 3.2: Critical Conditions

CRITICAL CONDITIONS				
gas consumption	m'_{gas}	[kg/h]	328,8	Eq. (2.3)
critical pressure	p*	[bar abs]	5,28	Eq. (2.11)
critical density	ρ*	[kg/m³]	3,28	Eq. (2.12)
critical temperature	T*	[°C]	287,8	Eq. (2.13)
critical velocity	a*	[m/s]	474,9	

3.1.3. Conditions at Primary Breakup Position

For the estimation of the mean gas velocity at breakup position, we use equations 2.4 – 2.10 presented in chapter 2.1. With the gas pressure ratio p_0/p_1=10 and the non-dimensional distance x/d_{nozzle}=14,5 we can also use figure 3.2 to estimate the maximum Mach number at the breakup position.

The theoretical supersonic core is longer than the distance from gas nozzle exit to melt breakup position. Mean gas velocity is subsonic, so equations 2.6 – 2.10 are used to calculate mean gas velocity at breakup position, $v_{mgas,BU}$. In addition, we have to consider gas inclination angle (see also the stream lines in figure 3.1, left picture). In the absence of a sufficient analysis of the 3D gas flow field, we estimate that the resulting gas velocity at breakup position corresponds to its value in melt flow direction.

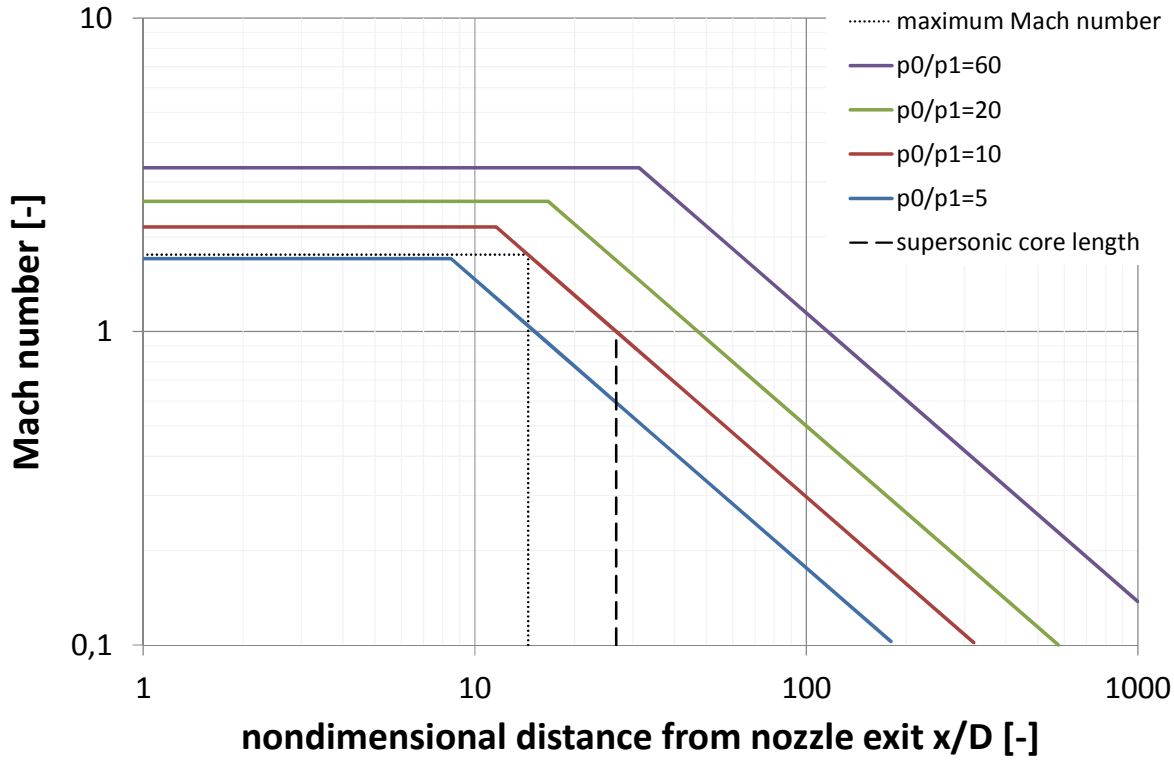

Figure 3.2: Estimation of the maximum Mach number and supersonic core length

Table 3.3: Conditions at primary breakup position

CONDITIONS AT BREAKUP				
Maximum Mach number	Ma_{max}	[-]	2,16	Eq. (2.4)
Mach number, Koria	Ma_{Koria}	[-]	1,76	Eq. (2.8)
gas velocity	v_{gas} (Ma_{max})	[m/s]	807,9	Eq. (2.10)
nondimensional distance	x/d_{nozzle}	[-]	14,5	
Mach number	Ma	[-]	1,76	
max gas velocity	$v_{maxgas,BU}$	[m/s]	719,5	
mean gas velocity	$v_{mgas,BU}$	[m/s]	359,8	Eq. (2.6)
gas flow half angle	α	[°]	30	
gas velocity in flow direction	$v_{gas,BU}$	[m/s]	311,6	
breakup Mach number	Ma_{BU}	[-]	0,62	
total gas flow	$m'_{gas,BU}$	[kg/h]	657,6	Eq. (2.7)
core gas temperature	$T_{gas,BU}$	[°C]	287,8	
mean gas temperature	$T_{mgas,BU}$	[°C]	243,9	
mean gas density	$\rho_{mgas,BU}$	[kg/m^3]	0,67	

3.1.4. Some Words about Heat Loss

a) Convective heat loss of the melt jet from nozzle exit to breakup position

The convective heat loss of the melt jet from nozzle exit to breakup position is estimated by a simple heat balance (equation 3.1, table 3.4). As the temperature decreases by only 1.1°C, we will ignore this quantity for ongoing calculations.

$$\dot{Q} = \dot{m}_{melt} c_{p,melt} \Delta T_{melt} = A_{jet} \alpha_{melt} \overline{(T_{melt} - T_{gas})} \tag{3.1}$$

Table 3.4: Cooling of the melt jet due to convection

COOLING OF THE MELT JET				
melt jet velocity	v_{jet}	[m/s]	1,51	
jet/gas Reynolds number	Re_{jet}	[-]	137	
ambient temperature	T_1	[°C]	200	
ambient gas viscosity	$\eta_{gas,1}$	[kg/ms]	2,57133E-05	
Nusselt number	Nu	[-]	6,8	
heat transfer coefficient	α_{jet}	[W/m²K]	81,6	
ambient gas conductivity	$\lambda_{gas,1}$	[W/mK]	0,0379	
melt jet surface area	$A_{meltjet}$	[m²]	0,00059	
convected heat	Q	[W]	74,2	
melt temperature loss	ΔT_{melt}	[°C]	1,1	

b) Radiation of the melt jet from nozzle exit to breakup position:

The heat loss of a body due to radiation is to be calculated as follows:

$$\dot{Q} = A \varepsilon \sigma_B \left(T_{melt}^4 - T_1^4\right) \tag{3.2}$$

The emissivity ε lies between 0 (black body) and 1 (perfect radiation) and is assumed to be 0,5. For estimating the heat loss of the open jet by radiation, see table 3.5.

Table 3.5: Heat loss of the jet due to radiation

RADIATION OF THE MELT JET				
ambient temperature	T_1	[°C]	200	
melt temperature	T_{melt}	[°C]	1750	
Stefan-Boltzmann constant	σ_B	[W/m²K⁴]	5,67E-08	
emissivity (estimation)	ε	[-]	0,5	
melt jet surface area	$A_{meltjet}$	[m²]	0,00059	
radiated heat	Q	[W]	277,7	
melt temperature loss	ΔT_{melt}	[°C]	4,0	

c) Radiation of Melt Droplets

The heat loss due to radiation of melt iron droplets of different sizes is roughly compared to convective heat losses (see table 3.6.). The smaller the droplet and the lower its temperature, the less important radiation is. At opposite conditions (large droplets, high temperature) as shown in table 3.6. (left column), we see that heat loss due to radiation becomes more important – but still is more than one order of magnitude smaller than heat loss due to convection. Hence, we will neglect radiation in our further calculations.

Table 3.6: Heat loss of melt droplets due to radiation

RADIATION OF A MELT DROPLET			**open jet**	**open jet**	**open jet**
droplet diameter	d_{drop}	[µm]	368	112	30
melt droplet surface area	A_{drop}	[m^2]	4,25E-07	3,94E-08	2,83E-09
melt droplet mass	m_{drop}	[kg]	2,09E-07	5,88E-09	1,13E-10
ambient temperature	T_1	[°C]	200	200	200
melt temperature	T_{melt}	[°C]	1729	1729	1729
Stefan-Boltzmann constant	σ_B	[W/m^2K^4]	5,67E-08	5,67E-08	5,67E-08
emissivity (estimation)	ε	[-]	0,5	0,5	0,5
radiated heat	Q	[W]	1,93E-01	1,79E-02	1,28E-03
melt temperature loss radiation	ΔT_{melt}	[°C/µs]	1,11E-03	3,65E-03	1,36E-02
melt temperature loss convection	ΔT_{melt}	[°C/µs]	1,20E-02	1,38E-01	1,93E+00
relation convection/radiation		[-]	10,8	37,8	141,8

3.1.5. Calculation of the Mean Ligament Diameter

According to See et al. [SEE1973], the melt jet is converted into a conical sheet with the opening angle similar to the gas flow angle (see figure 3.1). This is a reasonable approach which can be validated by examining pictures e.g. from Marcus [MAR2002]. (A variation of the angle of the conical sheet between 20 and 40 degrees results in a change of the calculated ligament diameter of less than 15 %.)

Using the model of Senecal et al. presented in chapter 2.3. [SEN1999], maximum wave length and maximum growth rate were calculated. In figure 3.3, we see the comparison between long wave (We < 1,69) and short wave breakup (We > 1,69). Exemplarily, the exact solution and the inviscid solutions are added to the figure for long wave assumption. In the following, the simplified solutions will be used for the calculations.

Corresponding data such as sheet thickness and velocity, breakup length, ligament diameter, primary droplet diameter and breakup time can be taken from table 3.7. The sheet Weber number (built with the sheet half thickness h_F) is slightly higher than 1,69, so we expect short wave breakup. Primary droplet diameters are quasi the same for short wave and long wave model. This is only the case when sheet Weber numbers are close to the long wave/short wave limit of 1,69.

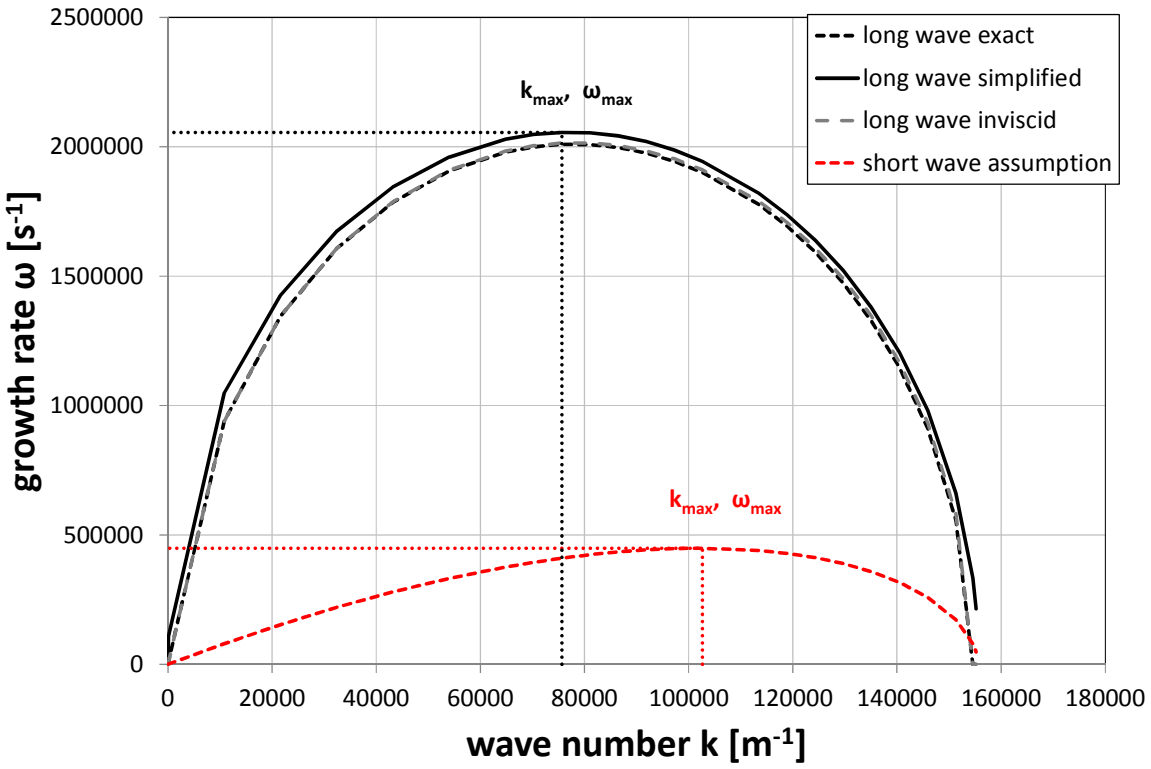

Figure 3.3: Growth rate as a function of wave number for the long wave assumption (dark lines: exact, inviscid and simplified solutions) and the short wave assumption (red lines)

Table 3.7: Conditions after primary breakup

PRIMARY BREAKUP			**short wave**	long wave
maximum growth rate	ω_{max}	[1/s]	**35782**	51870
maximum wave number	k_{max}	[1/m]	**21335**	15720
maximum wave length	λ_{max}	[µm]	**294,5**	399,7
sheet velocity	v_{sheet}	[m/s]	**10,5**	10,4
half sheet thickness	h_F	[mm]	**0,051**	0,076
sheet Weber number	We_{sheet}	[-]	**1,79**	2,67
breakup length	x_{BU}	[mm]	**3,5**	2,4
ligament diameter	D_L	[µm]	**195,6**	197,2
primary droplet diameter	d	[µm]	**368,4**	371,4
sheet breakup time	t_{sheet}	[µs]	**585,0**	231,3
ligament breakup time	t_L	[µs]	**325,9**	330,0

3.1.6. Cooling of the melt sheet and the ligaments

For sheet breakup, heat loss is estimated as follows (analogous to equation 3.1), the corresponding data can be found in table 3.8.

$$\dot{Q} = \dot{m}_{melt} c_{p,melt} \Delta T_{melt} = A_{sheet} \alpha_{melt} \overline{(T_{melt} - T_{gas})} \qquad (3.3)$$

The Nusselt number for the estimation of the heat transfer coefficient was calculated as follows:

$$Nu_{sheet} = 0{,}644 Re^{0{,}5} Pr^{0{,}33} \quad (3.4)$$

Table 3.8: Cooling of the melt sheet

COOLING OF THE SHEET				
initial melt temperature	T_{melt}	[°C]	1749	
relative sheet velocity	$v_{sheet\text{-}gas}$	[m/s]	296,9	
mean half sheet thickness	h_{Fmean}	[mm]	0,10	
sheet/gas Reynolds number	$Re_{sheet\text{-}gas}$	[-]	748	
gas temperature	T_{gas}	[°C]	243,9	
gas viscosity	η_{gas}	[kg/ms]	2,73187E-05	
Nusselt number	Nu	[-]	16,40	
heat transfer coefficient	α_{sheet}	[W/m²K]	6554,6	
gas conductivity	$\lambda_{gas,1}$	[W/mK]	0,0408	
sheet surface area	A_{sheet}	[m²]	0,00008	
convected heat	Q	[W]	762,7	
melt temperature loss	ΔT_{melt}	[°C]	11,0	

For ligament breakup, the heat loss can be estimated as follows:

$$Q = m_L c_{p,melt} \Delta T_{melt} t_{BU,L} = A_{lig} \alpha_{melt} \overline{(T_{melt} - T_{gas})} \quad (3.5)$$

With $t_{BU,L}$ being the ligament breakup time and A_L being the surface of the ligament (see table 3.8).

Here, the Nusselt number was calculated as follows:

$$Nu_L = 0{,}644 Re^{0{,}5} Pr^{0{,}33} \quad (3.6)$$

Table 3.9: Cooling of the ligaments

COOLING OF THE LIGAMENTS				
ligament temperature	T_L	[°C]	1738,0	
diameter of the cylinder	d_L	[µm]	195,6	
length of the cylinder	l_L	[µm]	867,9	
Reynolds number of cylinder	Re_L	[-]	1433	
Nusselt Number	Nu_L	[-]	22,5	
heat transfer coefficient	α_L	[W/m²K]	4681	
cylinder surface area	A_{sheet}	[m²]	6,54E-07	
convected heat	Q	[J]	1,48E-03	
mass of one ligament	m'_L	[kg]	1,82E-07	
melt temperature loss	ΔT_{melt}	[°C]	9,78	
ligament temperature	T_{melt}	[°C]	1728,2	

3.1.7. Secondary Droplet Breakup

For estimation of secondary breakup, we transform the calculated mean primary droplet diameter into a droplet size distribution. We assume a logarithmic normal distribution with a standard deviation of 2,5 and we take the calculated diameter as mass median diameter d_{50} from table 3.7. This distribution is shown in figure 3.4 for atomizer case study 1.

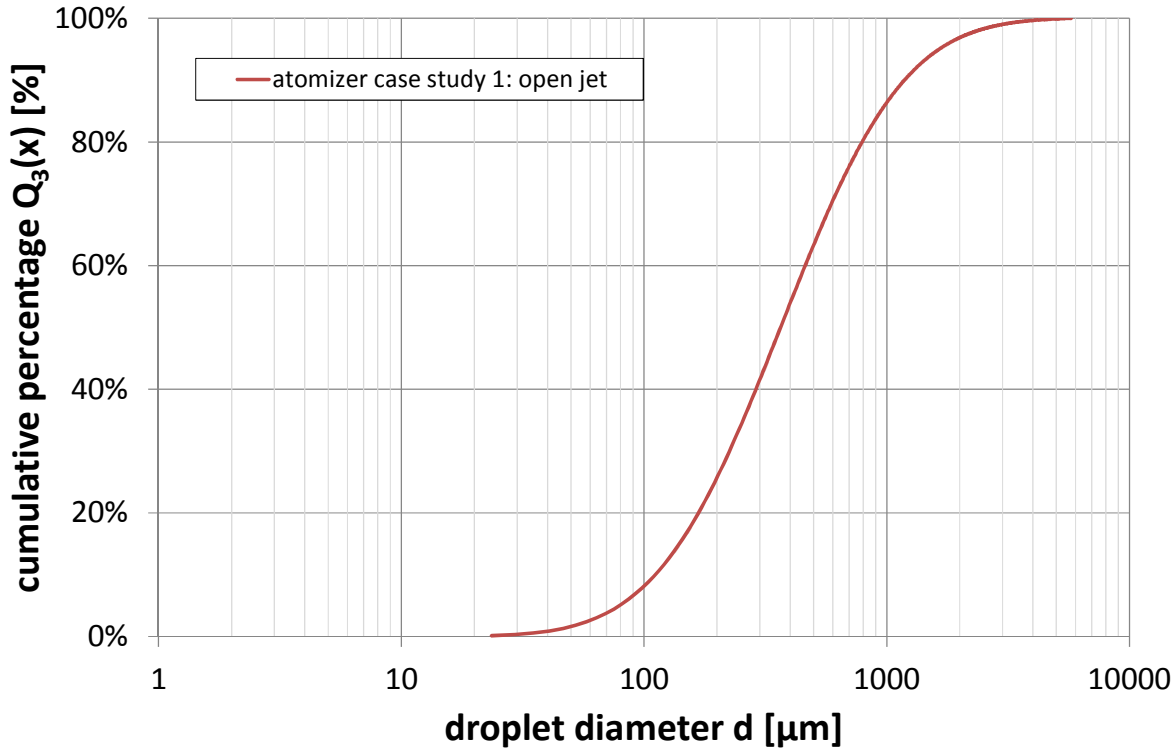

Figure 3.4: Cumulative particle sizes for the calculation of secondary breakup

Secondary bag breakup occurs in case of the droplet Weber number being higher than 16, shear breakup needs a droplet Weber number higher than 100. Hence, the percentage of the primary droplets which undergo secondary breakup can be determined and the resulting droplet diameter can be estimated. This is shown for the case of the open jet nozzle in figure 3.5.

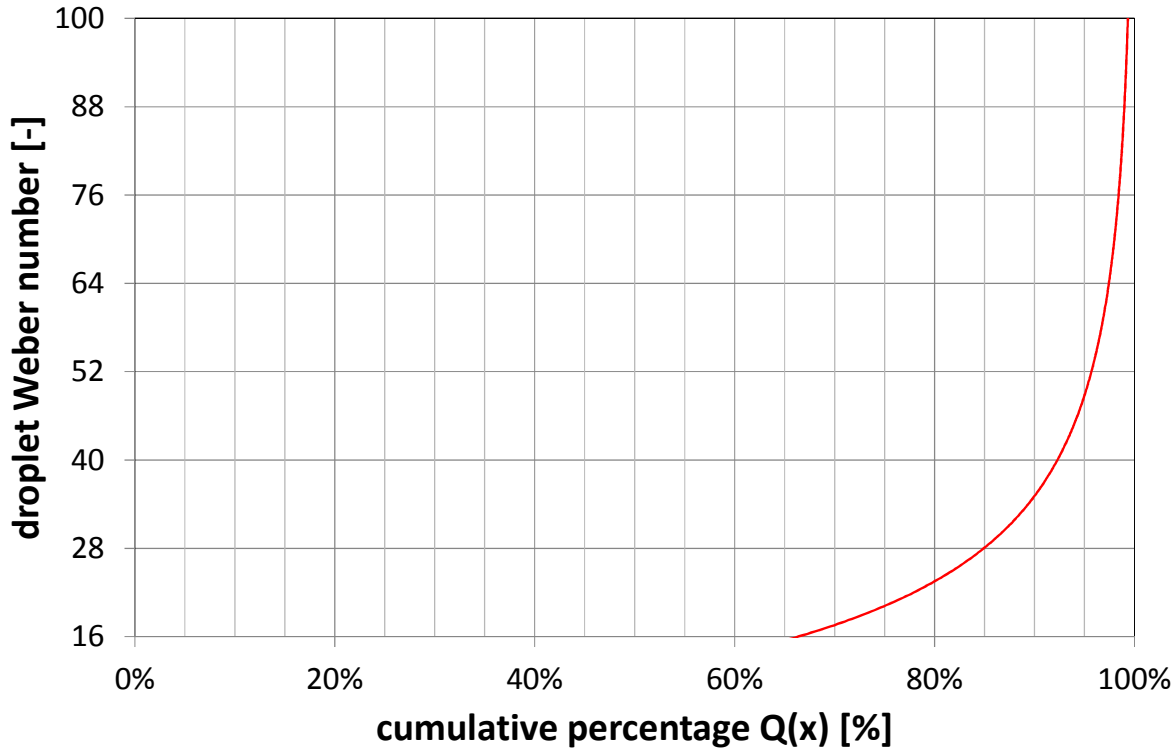

Figure 3.5: Droplet Weber number percentage due to secondary breakup. At Weber numbers higher than 16 (33,4 % of the droplets), bag breakup occurs, at We > 100 (0,65%), shear breakup is expected.

The resulting particle sizes can be taken from table 3.10.

Table 3.10: Secondary breakup conditions and results

SECONDARY BREAKUP				
primary droplet diameter	d	[µm]	368,4	
relative velocity	v_{rel}	[m/s]	287,0	
Bag Breakup Percentage	Q_{BB}	[%]	33,36%	
secondary diameter	$d_{sec,bag}$	[µm]	157,9	
Shear Breakup Percentage	Q_{SB}	[%]	0,65%	
secondary diameter	$d_{sec,shear}$	[µm]	22,1	
residueing primary droplets	$d_{prim,res}$	[µm]	241,4	
resulting diameter	d_{sec}	[µm]	212	

3.1.8. Droplet Acceleration, Spheroidization, Cooling and Solidification

In a final step, the behavior of droplets of various sizes was analyzed in further detail with regards to

- Secondary breakup
- Acceleration
- Cooling
- Solidification
- Spheroidization

This is now explained exemplarily for a droplet with a diameter d=1182µm (which corresponds to the d_{90} in atomizer case study 1). With data from table 3.10 and using the method described by Gratzer [GRA2012], we can calculate the droplet Weber number in the gas stream (figure 3.6).

At the same time, the cooling and solidification process of the droplet is calculated, results are shown in figure 3.7 as a function of time (left picture) and of the distance travelled (right picture). At the chosen conditions, our droplet travels about 16 meters until it is completely solidified!

Spheroidisation time is calculated using the method of Rao [RAO1973]. In our simplified model, spheroidisation starts as soon as We<1. This process is shown in figure 3.8. We see that the droplet is oscillating at a frequency of about 240Hz.

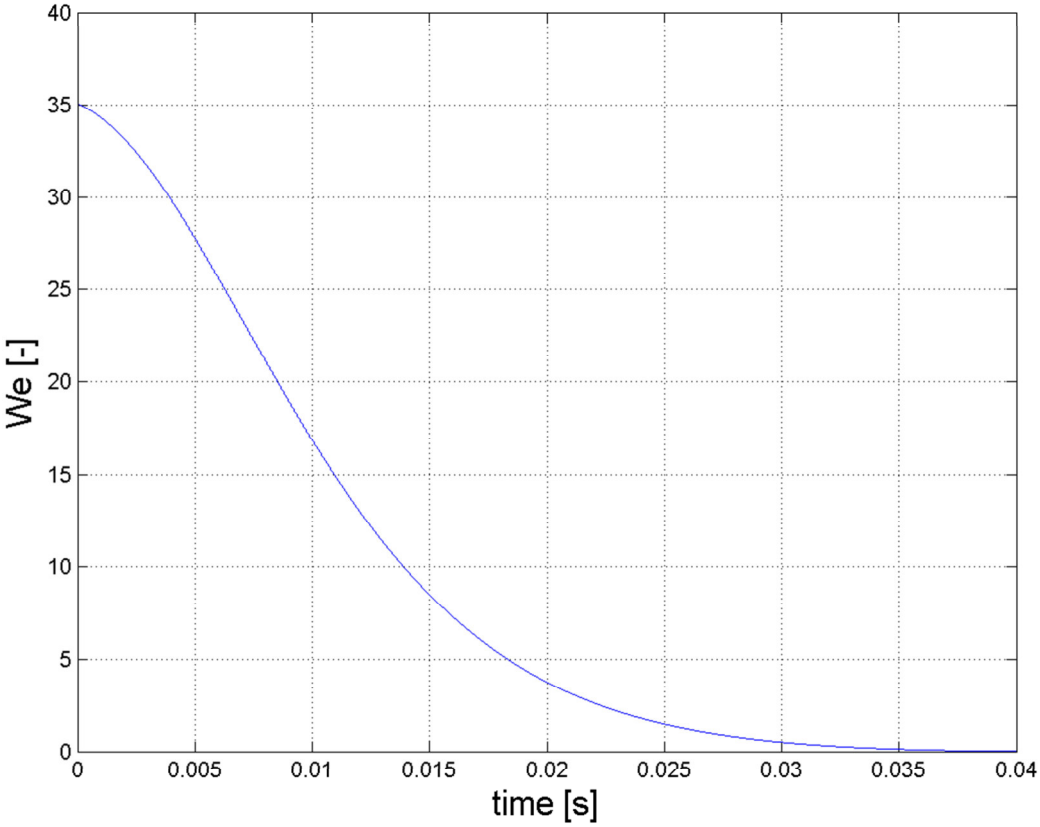

Figure 3.6: Droplet Weber number for a droplet with diameter d=1182µm; as long as We>16, secondary breakup may occur, while at We<1, we expect spheroidization to start.

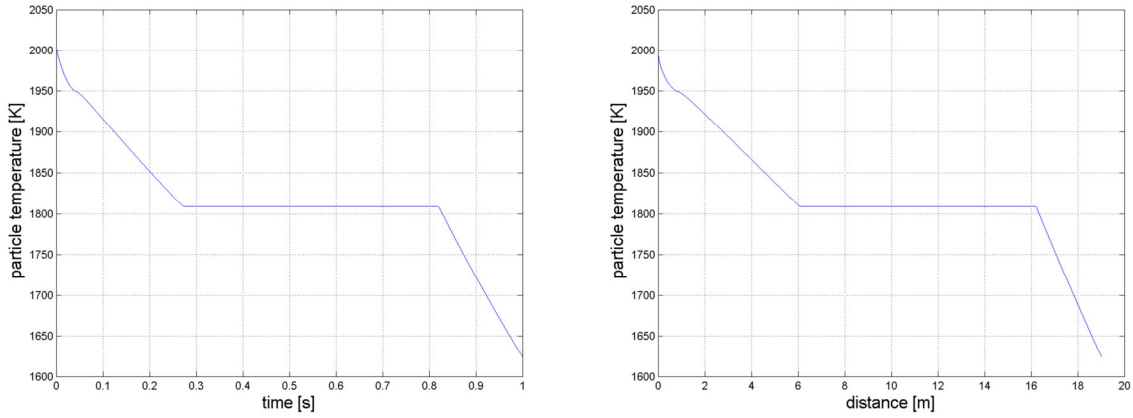

Figure 3.7: Droplet temperature evolution of a droplet with diameter d=1182 µm as a function of time (left picture) and distance travelled (right picture).

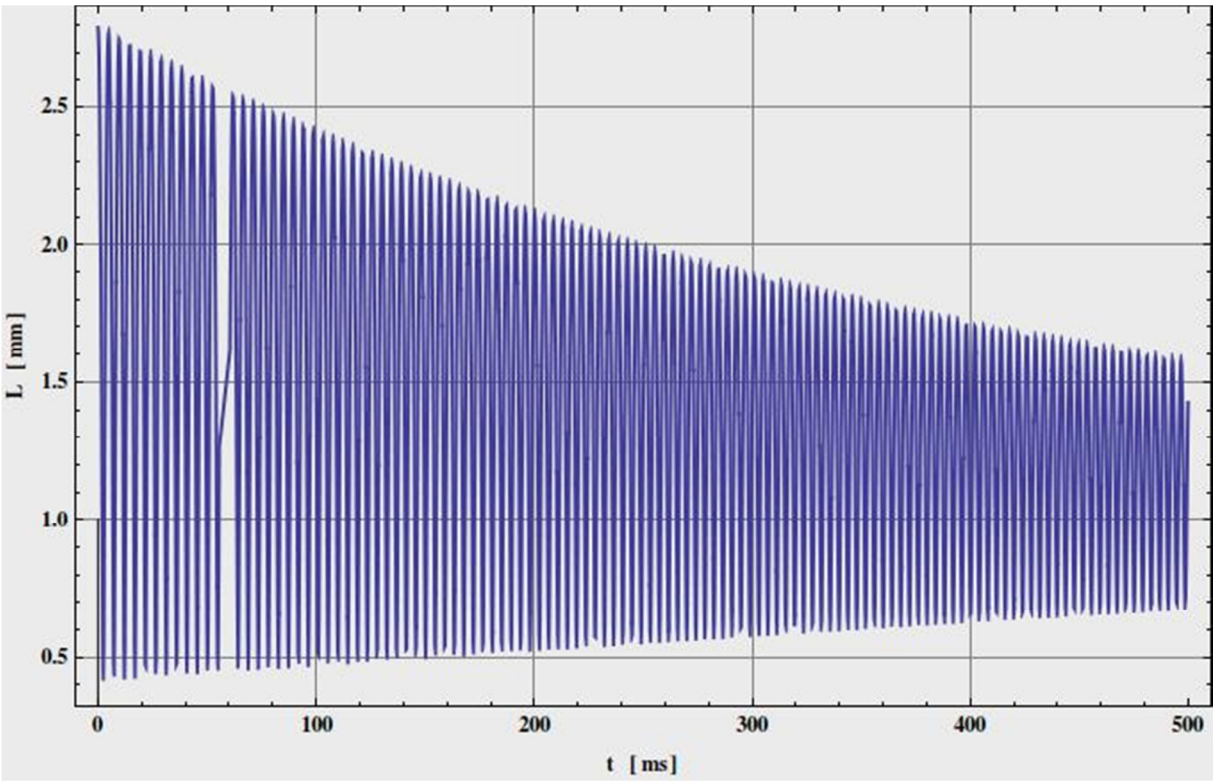

Figure 3.8: Oscillation of the droplet; the process starts with at a droplet length of 2,37*d and – per definition – terminates at 1,38*d

The time the droplet needs for breakup was calculated using equation 2.57 [GOR1959]. A comparison of these characteristic times can be seen in figure 3.9. This picture leads us to the following conclusions:

- The time our droplet needs to breakup is one order of magnitude lower than the time the droplet Weber number is higher than 16 (“acceleration time”) and 2 orders of magnitude lower than cooling time. Hence, secondary breakup of the droplet is very likely.
- Spheroidisation time is higher than cooling time and almost as long as solidification time – hence, the melt droplet will partly be solidified before it is spherical.

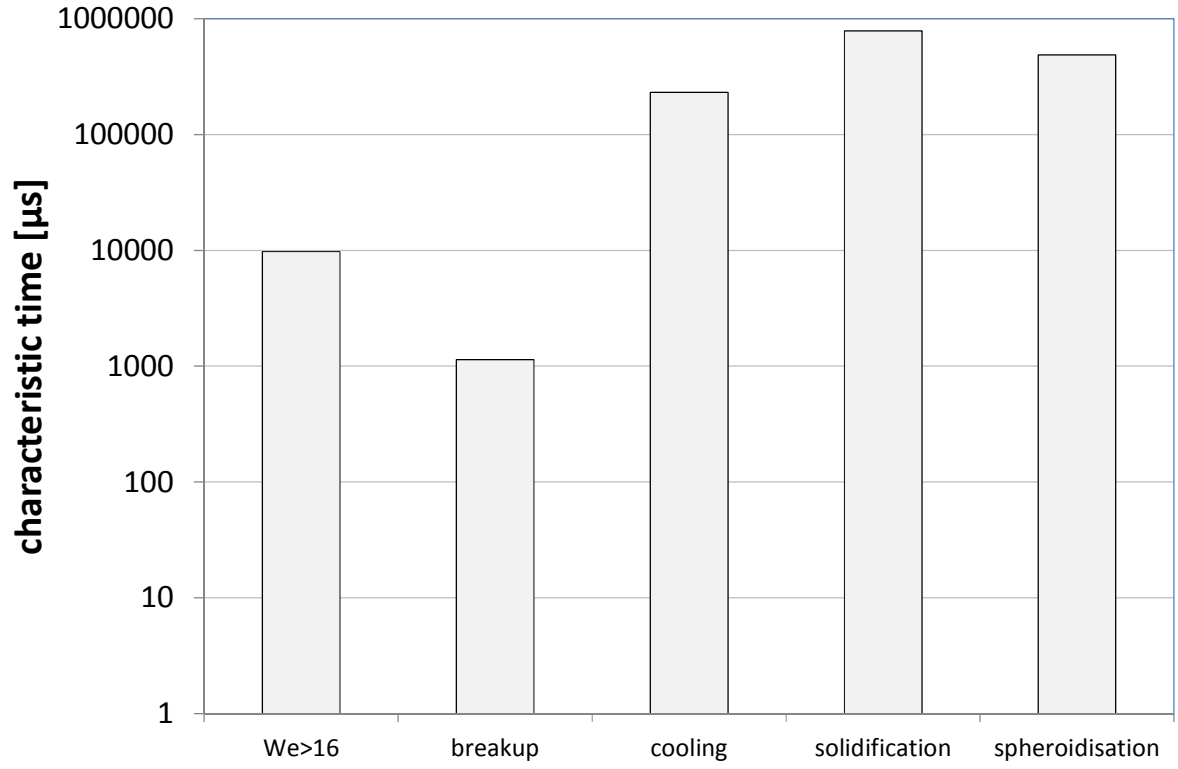

Figure 3.9: Characteristic times for a droplet with diameter d=1182µm

These characteristic times can be estimated for all droplet sizes for a given atomization situation (material system, gas and melt temperatures, relative velocity) which is shown in figure 3.10. We see that spheroidization time lies between solidification and cooling time, except for very small particles (<15µm) for which we expect spherical shape. Secondary breakup is only likely for particles larger than about 650µm (window within the blue and green lines). This figure also gives some indication what needs to be done to change product properties:

- ➔ Production of finer powder: Here, it is necessary to move the green line upwards and to the left, which can be done by increasing relative velocity or gas density (e.g. by using gases with higher sonic velocities or elevated gas temperature and atomizing into a pressurized chamber)
- ➔ Production of spherically shaped powder: Here, we need to increase melt temperature or decrease relative velocity and/or gas density, so the cooling time is increased by almost an order of magnitude. Still, for particles > 100µm it will hardly be possible to produce spherical steel particles by twin fluid atomization.

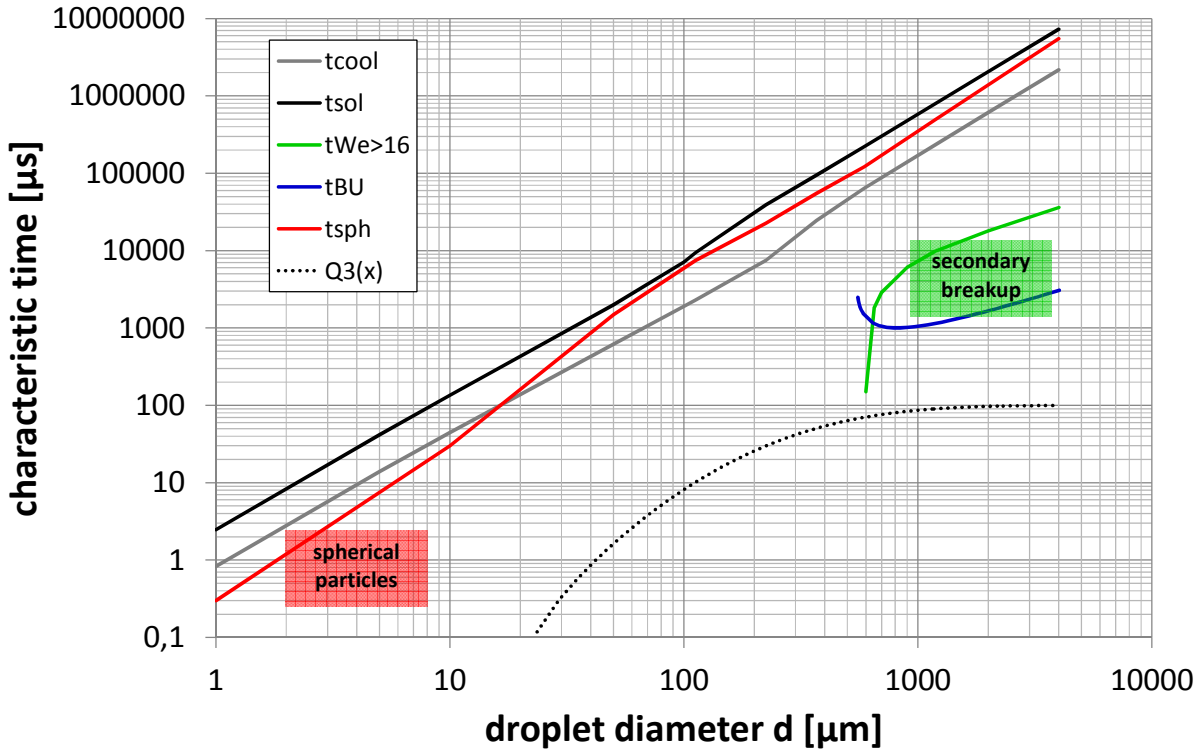

Figure 3.10: Characteristic times for the whole size range for atomizer case study 1; the black dotted line shows the primary droplet size distribution

3.1.9. Time and Length Scales in Atomizer Case Study 1

In table 3.11, an overview of times and distances travelled in the different conditions – starting with primary breakup and ending with solidification – is listed. As soon as primary droplets are involved, the mass median particle size (d_{50}=212µm) is chosen for the calculations. Additionally, gas and melt velocities are listed.

Table 3.11: Time and length scales in melt atomization (atomizer case study 1)

open jet	distance travelled	time travelled	melt temp.	gas velocity	melt velocity	relative velocity
	[mm]	[µs]	[°C]	[m/s]	[m/s]	[m/s]
primary breakup (start)	0	0	1750	311,6	1,5	310,1
primary breakup (end)	3,6	585	1738	307,4	10,5	296,9
ligament breakup	5,02	911	1729	306,2	19,2	287
cooling	755	25311	1536	30	39,9	-9,9
solidification	3275	95111	1536	0	32,6	-32,6

3.1.10. Comparison to Other Work

Due to the high number of possible differences in geometry and operating parameters, it is difficult to compare the model to available data. Nevertheless, we chose the following 2 options:

a) Atomization of Steel, Comparison to Lubanska's Model:

Lubanska's model [LUB1970] is widely used for prediction of atomizer performance of any kind, and its value is discussed distinctively in several books [e.g. YUL1994, LAW1992]. Using the atomizer geometry described above, Lubanska's equation (1.8) was applied and the data is compared to our model in figure 3.11. Additionally, Rao's results were introduced into the picture [RAO1971]. Rao's atomizing and operating conditions are slightly different to what is used here, but still well comparable.

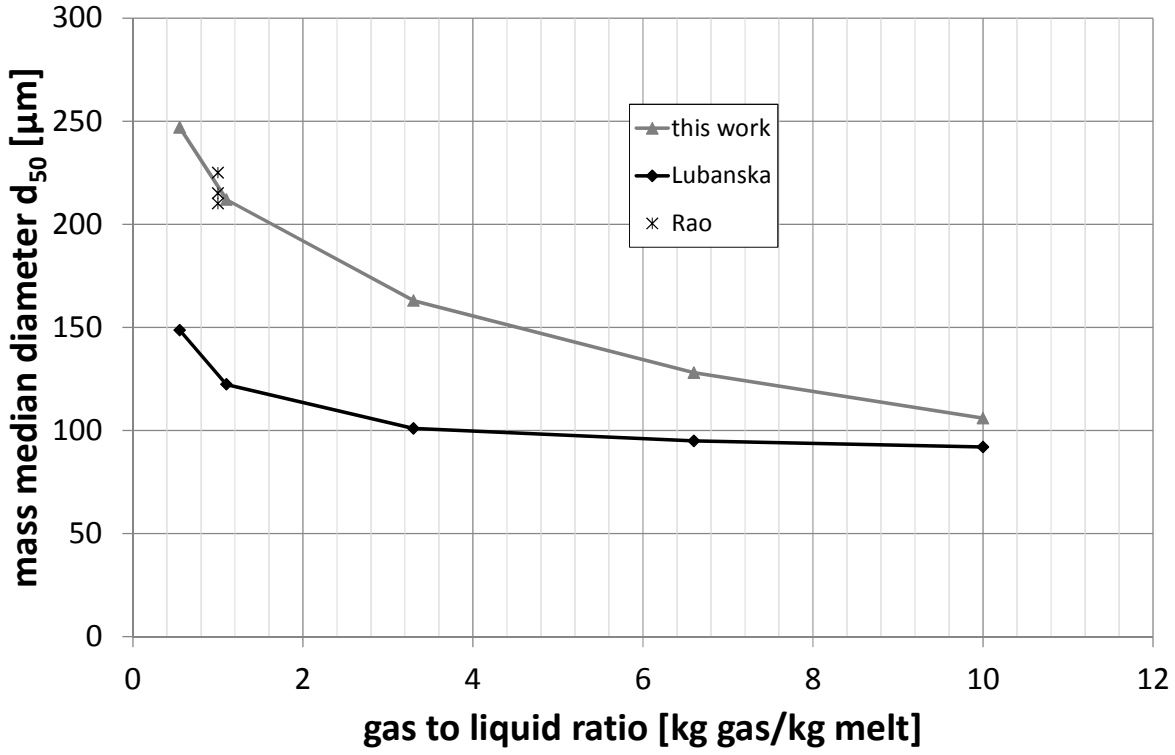

Figure 3.11: Comparison of 2 models for steel powder production (Lubanska vs. this work) and atomization results of Rao

b) Atomization of Tin

The procedure presented in this chapter to predict particle sizes was also applied to the atomization of tin following the production data of See and Johnston [SEE1978]. The results are well comparable, although the influence of the gas to liquid ratio (GLR) is stronger for experimental data compared to our model (figure 3.12.).

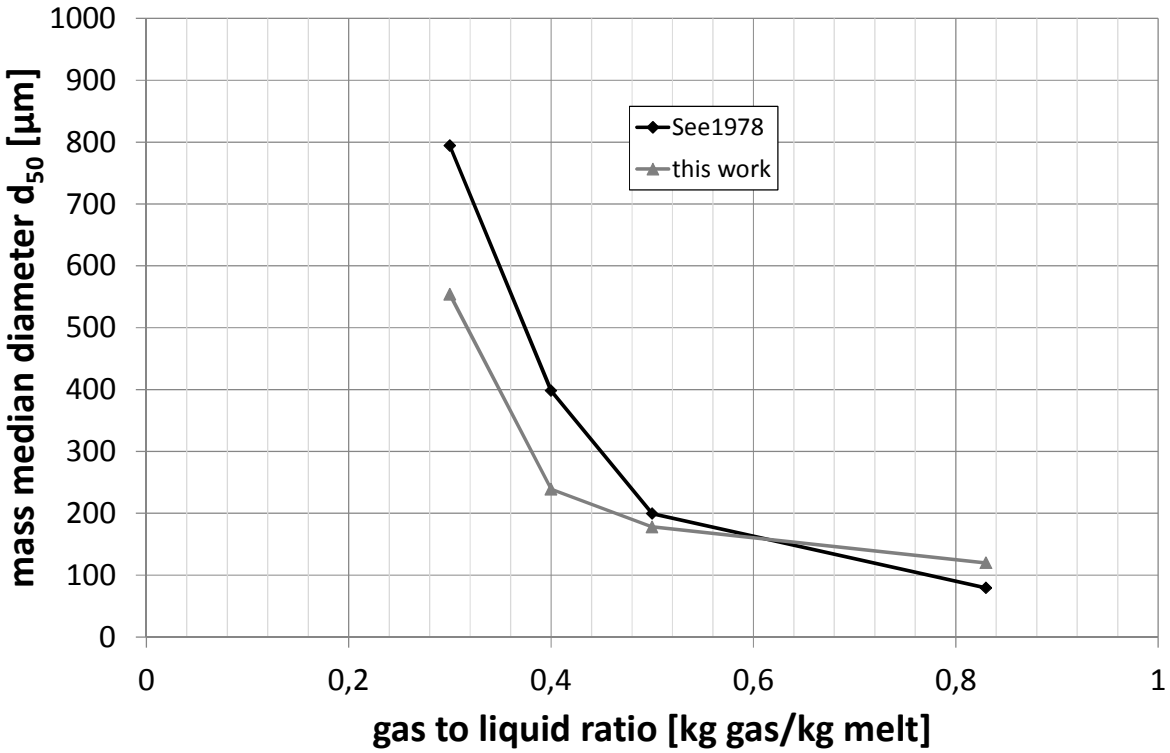

Figure 3.12: Comparison of See's data with the present model for tin

3.1.11. How can we Produce Finer Powder?

For upcoming applications (e.g. additive manufacturing), it is necessary to produce steel powders with sizes between 10 and 45 µm. For reasons of product purity and process reliability, this is often done by open jet atomization. The model presented here can be a means to understand how we can move the particle size distribution from a d_{50} of 212µm (table 3.10) towards much finer results:

a) Increase Gas-To-Liquid Ratio (GLR)

This is already shown in figure 3.10 – an increase of the GLR from 1 to 10 kg gas/kg melt (by decreasing melt flow rate) leads to a decrease of the theoretical mass median diameter from 212µm to 106µm, because the primary sheet thickness is strongly decreasing, which leads to finer ligaments.

b) Increase Gas Reservoir Pressure

Increasing gas pressure leads to a higher relative velocity between gas and melt. Hence, ligament diameter is smaller and secondary breakup is more likely. Additionally, GLR is increasing in the case of keeping any other parameter constant. Comparing the effect of increasing gas pressure to decreasing melt throughput, we see that the decrease of the mass median diameter d_{50} is of the same order of magnitude, and it seems that the gas-to-liquid ratio is the main influence (see table 3.12.).

Table 3.12: Influence of gas reservoir pressure on gas-to-liquid ratio and mass median diameter

gas reservoir pressure [bar]	gas-to-liquid ratio [kg gas/kg melt]	mass median diameter [µm]
10	1,1	212
40	4,4	130
91	10	107

c) Nozzle Geometry Options

To increase GLR, it is also possible to increase gas nozzle diameter or to use more gas nozzles. The effect of the latter is described in [HEC2000] and cannot be discussed here. The effect of the increase of the gas nozzle diameter on particle size is characterized by the length of the supersonic core, which is proportional to the nozzle diameter and shown in table 3.13. Apparently, also here the gas-to-liquid ratio is the main influence on particle size for the given geometry!

Table 3.13: Length of the supersonic core and mass median diameter at different conditions

gas nozzle diameter [mm]	gas reservoir pressure [bar]	supersonic core length [mm]	mass median diameter [µm]
4,7	10	58	212
4,7	40	116	130
4,7	91	189	107
4,7	10	58	212
10	10	116	130
14,2	10	164	115

d) Atomization Gas

As a comparison, we use Helium as atomization gas for the calculations – due to the higher sonic velocity, we expect finer powder. According to our model, we can reduce particle size by about 35% by replacing air by Helium (see figure 3.13). As one would expect the use of Helium to be even more beneficial, we also investigate secondary droplet behavior (see figure 3.14). Due to a higher heat transfer coefficient, the use of Helium leads to a reduction in cooling and solidification time. The more important change is the secondary breakup window, which is wider – breakup time is much smaller, while acceleration time (the time where the Weber number is still higher than 16) is increasing. Hence, the probability of secondary breakup is strongly increasing. Additionally, if we look at droplet breakup in detail, we see that during breakup, the surface area of the droplet is increasing, which leads to a quicker freezing process. Often, freezing is observed while breakup is not finished. As – due to Helium as atomization gas – breakup time is strongly decreasing, the solidification during breakup becomes less likely.

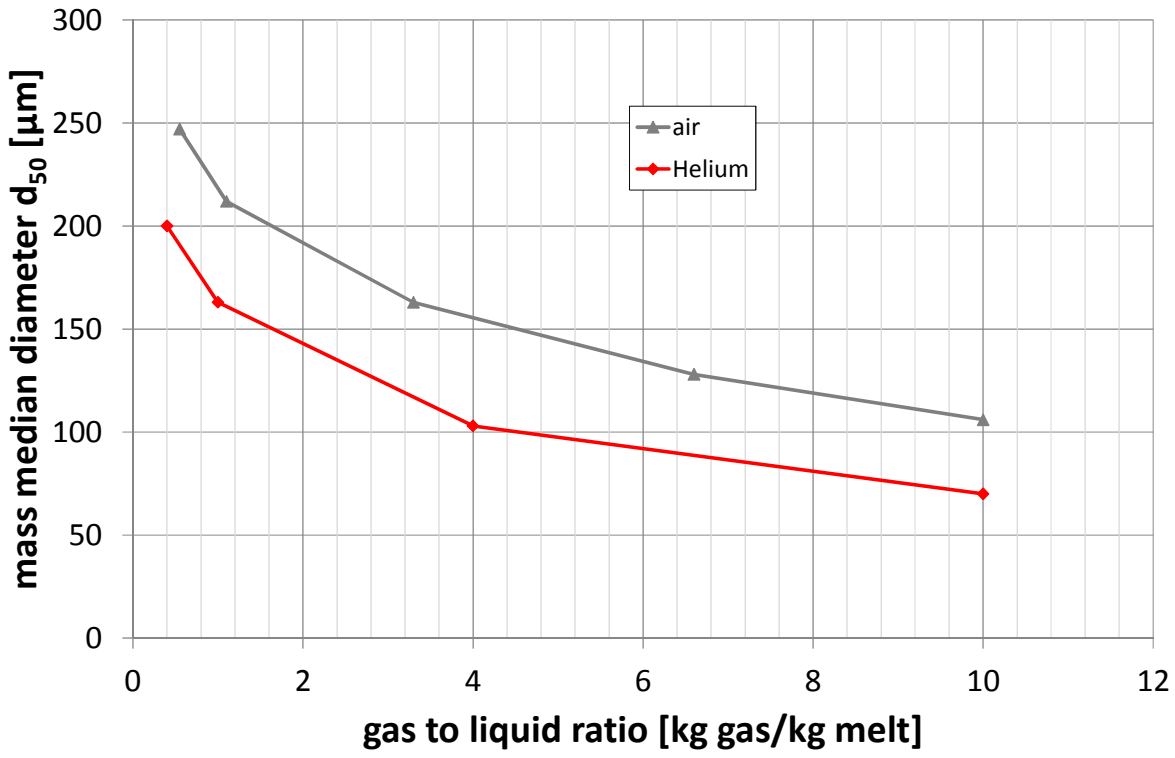

Figure 3.13: Influence of atomization gas on predicted particle sizes with our model

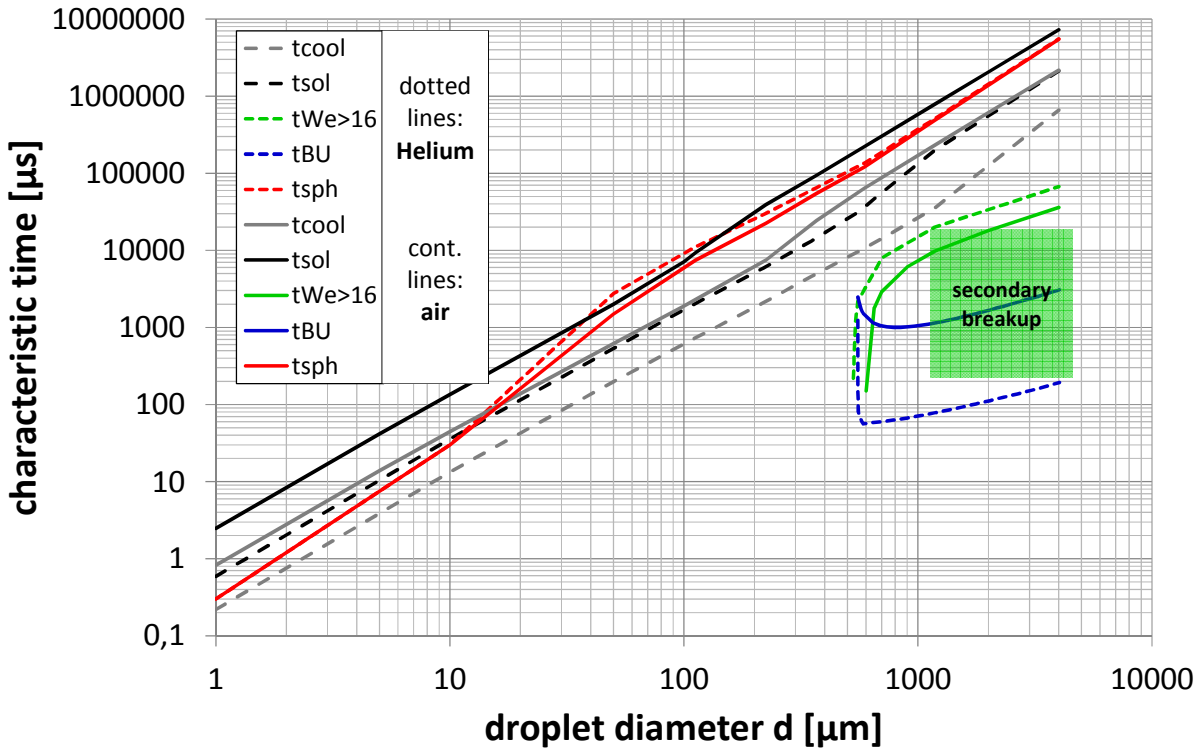

Figure 3.14: Influence of atomization gas on secondary droplet behaviour

3.2. Prefilming and Direct Nozzles

3.2.1. Nozzle Geometry, Material System and Initial Conditions

The geometry of the 2 atomization systems is shown in figure 3.14, the corresponding geometrical details and the boundary conditions for the calculations are given in table 3.14.

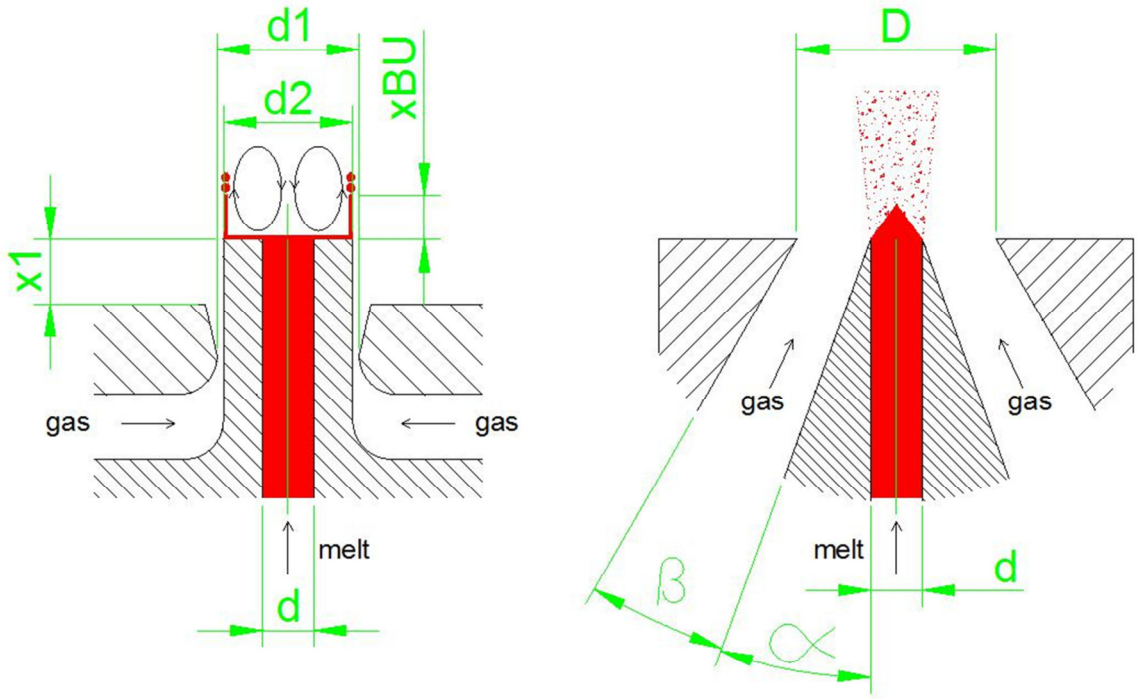

Figure 3.15: Left picture: prefilming atomization; pressurized gas flows through a gas gap width; on the nozzle face, a cylindrical sheet is formed which breaks into ligaments at a breakup length x_{BU}; right picture: direct atomization; directly at the jet surface, waves which convert into ligaments are shed from the jet

Table 3.14: Nozzle Geometry and Initial Conditions for Atomizer Case studies 2 & 3

AMBIENT CONDITIONS			**prefilming**	**direct**
ambient pressure	p_1	[bar abs]	1	1
ambient temperature	T_1	[°C]	20	20
ambient gas density	ρ_1	[kg/m³]	1,19	1,19

NOZZLE GEOMETRY			**prefilming**	**direct**
gas nozzle diameter	D	[mm]	-	
number of nozzles	n	[-]	1	1
gas outer nozzle diameter	d_1	[mm]	11	15,5
gas inner nozzle dimaeter	d_2	[mm]	10	4
gas outer half flow angle	β	[°]	0	30
gas inner half flow angle	α	[°]	0	20
gas gap width	-	[mm]	0,5	5,75
gas cross section (4 nozzles)	A_{nozzle}	[mm²]	16,5	176,1
distance gas/liquid contact point	x	[mm]	5	0
liquid jet diameter	d	[mm]	4	4

INITIAL CONDITIONS - AIR			**prefilming**	**direct**
gas reservoir pressure	p_0	[bar abs]	16,6	16,6
gas reservoir temperature	T_0	[°C]	0	0
gas density	ρ_0	[kg/m³]	21,2	21,2
sonic velocity	a_0	[m/s]	331,5	331,5

INITIAL CONDITIONS - ALUMINIUM			**prefilming**	**direct**
melt production rate	m'_{melt}	[kg/h]	24	256
melt temperature	T_{melt}	[°C]	875	875

3.2.2. Critical Conditions

Similar to chapter 3.1.2., critical conditions are calculated (see table 3.15)

Table 3.15: Critical Conditions

CRITICAL CONDITIONS			**prefilming**	**direct**
gas consumption	m'_{gas}	[kg/h]	203,6	2174,6
critical pressure	p*	[bar abs]	8,77	8,77
critical density	$\rho*$	[kg/m³]	13,43	13,43
critical temperature	T*	[°C]	-45,53	-45,53
critical velocity	a*	[m/s]	302,5	302,5
gas-to-liquid ratio	GLR	[kg_{gas}/kg_{liq}]	8,5	8,5

3.2.3. Conditions at Primary Breakup Position

The mean gas velocity for atomizer case studies 2 and 3 (Prefilming & "Direct" nozzles) is estimated with equations 2.15 and 2.16 (see chapter 2.1). The evolution of the gas velocity with distance from nozzle exit is shown in figure 3.16.

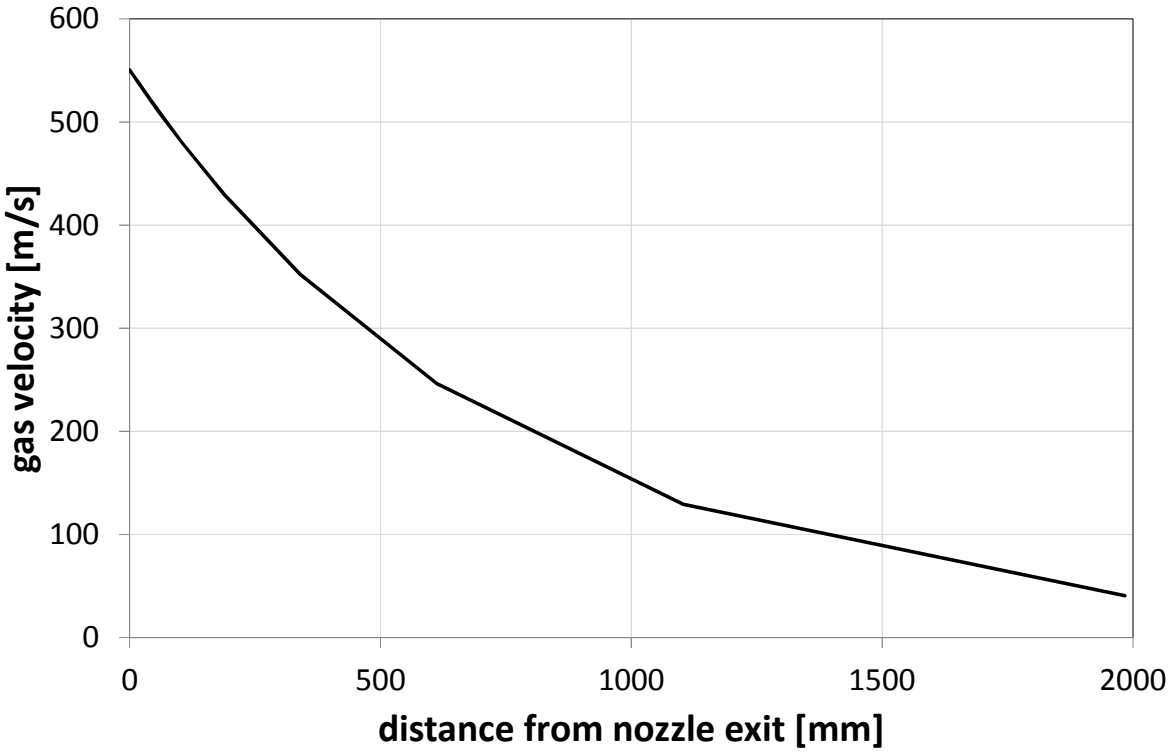

Figure 3.16: Mean gas velocity for confined nozzles (case studies 2 and 3)

Due to boundary layer phenomena we expect the effective relative velocity between liquid sheet and gas flow never to exceed sonic velocity (case study 2 – prefilming nozzle). Further insight into this topic can be found e.g. in [ZHO1992, LI1992, FUN2006].

To ease calculations for case study 3 (direct nozzle), we limit relative velocity to 0,9*Ma as described in [BRA1973a]. This simplification may appear rude and arbitrary to the reader, but it strongly reduces efforts, while the deviation of the d_{50} according to Bradley is less than 10% [BRA1973b].

Conditions for the calculation of primary breakup can be taken from table 3.16.

Table 3.16: Conditions at primary breakup position

CONDITIONS AT PRIMARY BREAKUP POSITION			**prefilming**	**direct**
gas velocity	$v_{gas,BU}$	[m/s]	302,5	272,3
breakup Mach number	Ma_{BU}	[-]	1	0,9
gas temperature	$T_{gas,BU}$	[°C]	-45,5	-45,5
gas density	$\rho_{gas,BU}$	[kg/m^3]	1,55	1,55

3.2.4. Calculation of the mean ligament diameter

a) Prefilming atomization:

As described in chapter 2.2.2, we determine maximum wave number and growth rate for a melt sheet – this time, a cylindrical sheet can be assumed as shown in figure 3.15., left picture. With

k_{max} and ω_{max} taken from figure 3.17, we can calculate all necessary variables for cylindrical sheet breakup (see table 3.18).

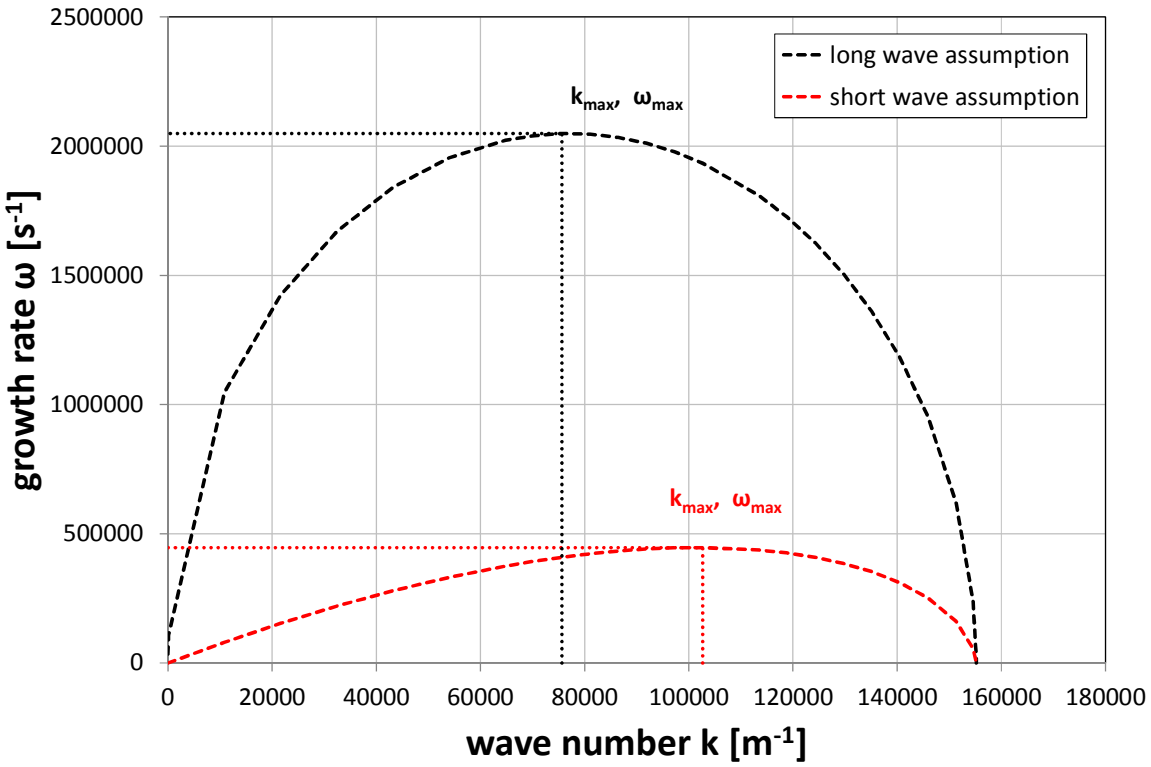

Figure 3.17: Maximum growth rate and wave number for the long wave and short wave assumptions (atomizer case study 2).

Table 3.18: Conditions after primary breakup for prefilming nozzle

CONDITIONS AFTER PRIMARY BREAKUP			short wave	**long wave**
maximum growth rate	ω_{max}	[1/s]	446701	**2048829**
maximum wave number	k_{max}	[1/m]	102668	**75650**
maximum wave length	λ_{max}	[µm]	61,2	**83,1**
sheet velocity	v_{sheet}	[m/s]	27,3	**85,1**
half sheet thickness	h_F	[mm]	0,00155	**0,00054**
sheet Weber number	We_{sheet}	[-]	0,244579	**0,085208**
breakup length	x_{BU}	[mm]	0,73	**0,50**
ligament diameter	D_L	[µm]	15,5	**7,6**
primary droplet diameter	d	[µm]	29,3	**14,3**
sheet breakup time	t_{sheet}	[µs]	26,9	**17,0**
ligament breakup time	t_{lig}	[µs]	6,1	**2,1**

As the resulting half sheet thickness h_F is very low, Weber numbers are low, too and we are working in the long wave regime (We<1,69).

b) Direct Atomization:

Using Bradley's model and the assumptions described in chapter 2.2.1., we are able to calculate maximum wave number ω_{max} and corresponding wave number k_{max} for jet breakup (figure 3.18.)

and then estimate all necessary quantities to describe jet breakup in the atomization regime (table 3.19).

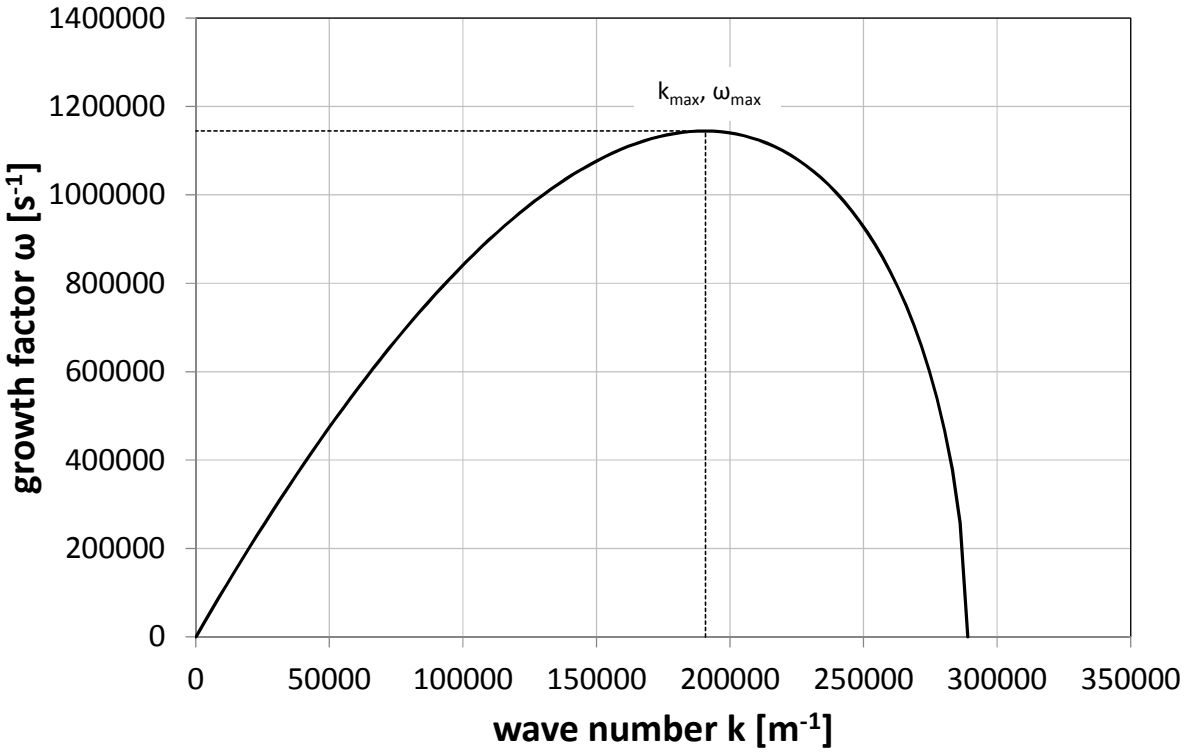

Figure 3.18: Maximum growth rate and wave number using Bradley's model (atomizer case study 3).

Table 3.19: Primary breakup conditions for direct nozzle

CONDITIONS AFTER PRIMARY BREAKUP				
maximum growth rate	ω_{max}	[1/s]	1144484	
maximum wave number	k_{max}	[1/m]	190775	
maximum wave length	λ_{max}	[µm]	32,9	
jet velocity	v_{jet}	[m/s]	2,4	
mean breakup diameter	d_{BU}	[mm]	3,17	
mean ligament mass	m_L	[mg]	0,0013	
breakup length	x_{BU}	[mm]	1,62	
ligament diameter	D_L	[µm]	8,2	
primary droplet diameter	d	[µm]	15,6	
mean breakup time	t_{BU}	[µs]	681,6	
ligament breakup time	t_{lig}	[µs]	2,4	

Although the methods of calculation seem to be strongly differing, wave numbers and growth rates for atomizer case studies 2 and 3 are in the same order of magnitude – and so is the calculated primary droplet diameter.

3.2.5. Cooling of the Melt during Primary Breakup

Similar to chapter 3.1.6., the heat loss of the melt during primary breakup is calculated – the results can be seen in table 3.20. Apparently, the heat loss of the sheet is much higher than the heat loss of the jet, which is due to the sheet thickness which is 4 orders of magnitude smaller than the jet diameter. From practical experiences, we know that nozzle tip freezing is an issue for prefilming nozzles, while this is hardly the case if we have jet breakup. For the sake of completeness, it is important to mention that we do not take into account heat transfer before the nozzle exit here (hoping that we are able to work with perfectly isolating nozzle tip materials).

Table 3.20: Melt temperature loss during primary breakup

COOLING OF THE MELT SHEET or JET			**prefilming**	**direct**
relative velocity of the sheet	$v_{sheet/gas}$	[m/s]	458,8	-
relative velocity of the jet	$v_{jet/gas}$	[m/s]	-	549,5
mean half sheet thickness	h_{Fmean}	[mm]	0,00054	-
mean breakup diameter	d_{BU}	[mm]	-	3,17
Reynolds number	$Re_{melt-gas}$	[-]	52	182565
gas temperature	T_{gas}	[°C]	-45,5	-45,5
ambient gas viscosity	$\eta_{gas,1}$	[kg/ms]	1,48E-05	1,48E-05
Nusselt number	Nu	[-]	4,33	328,73
heat transfer coefficient	α_{melt}	[W/m²K]	83973,5	2173,0
gas conductivity	$\lambda_{gas,1}$	[W/mK]	0,0210	0,0210
melt surface area	A_{cone}	[m²]	0,0000157	0,0000162
convected heat	Q	[W]	1124,7	32,4
melt temperature loss	ΔT_{melt}	[°C]	129,8	0,4
melt temperature	$T_{melt,BU}$	[°C]	745,2	874,6

Similar to chapter 3.1.6., the heat loss of the ligaments during breakup is estimated (see table 3.21.). Melt temperature after primary breakup is now reduced by 140°C for prefilming nozzle and only by 14°C for direct nozzle. Hence, a certain superheat is absolutely necessary if we want to operate a prefilming nozzle without freezing issues.

Table 3.21: Melt temperature loss during ligament breakup

COOLING OF THE LIGAMENTS			**prefilming**	**direct**
ligament temperature	T_{lig}	[°C]	745,2	874,6
diameter of the cylinder	D_L	[µm]	7,6	8,2
length of the cylinder	l_L	[µm]	33,5	36,5
Reynolds number of cylinder	Re_L	[-]	363	474
Nusselt Number	Nu_L	[-]	11,3	12,9
heat transfer coefficient	α_L	[W/m²K]	31360,9	32878,8
cylinder surface area	A_L	[m²]	8,86E-10	1,16E-09
convected heat	Q	[J]	4,54E-08	0,035
mass of one ligament	m_L	[kg]	3,57E-12	1,95E-06
melt temperature loss	ΔT_{melt}	[°C]	9,78	13,71
ligament temperature	$T_{melt,BU}$	[°C]	735,5	860,9

3.2.6. Secondary Droplet Breakup

Again, for estimation of secondary breakup, the calculated mean primary droplet diameter is transformed into a droplet size distribution with a standard deviation of 2,5 – this distribution is shown in figure 3.19 for atomizer case studies 2 and 3. The Weber number as a function of the cumulative percentage for the 2 atomizer case studies is shown in figure 3.20 – as was done in chapter 3.1.7., secondary droplet sizes can be estimated for the 2 case studies. As the relative velocity for direct nozzles is higher, secondary breakup is much more important and resulting particles are smaller here (see table 3.22).

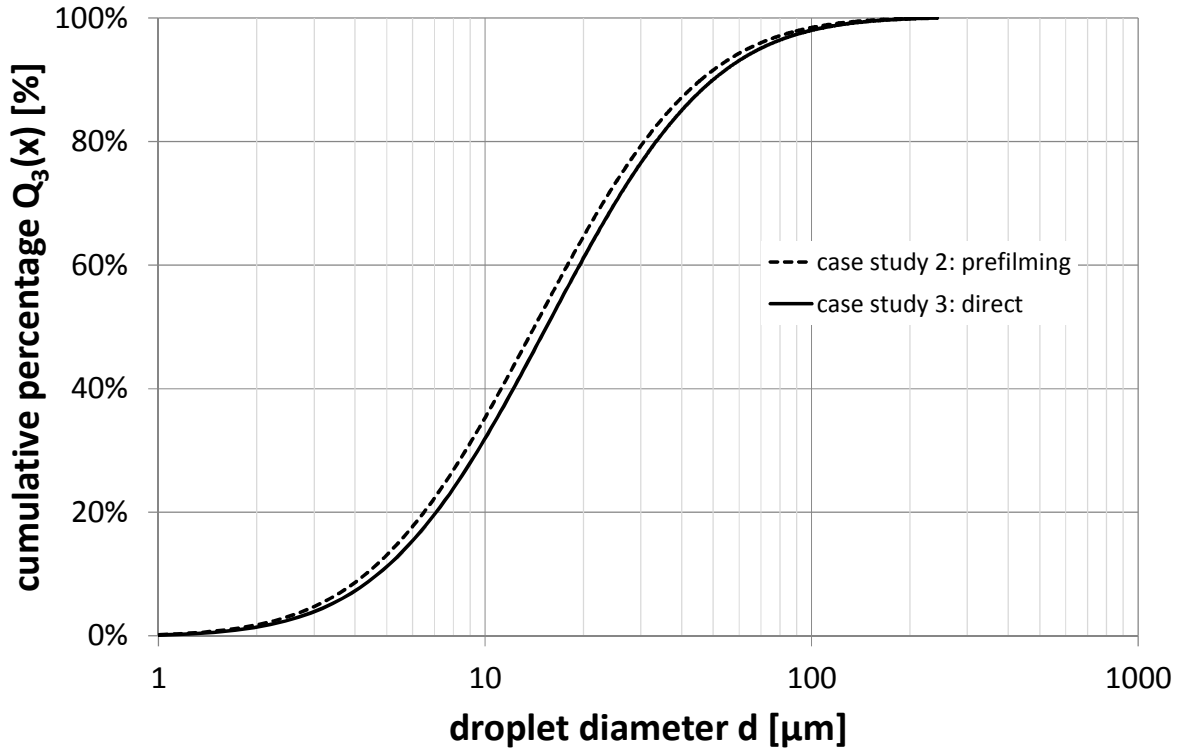

Figure 3.19: Cumulative particle sizes for the calculation of secondary breakup (atomizer case studies 2 and 3)

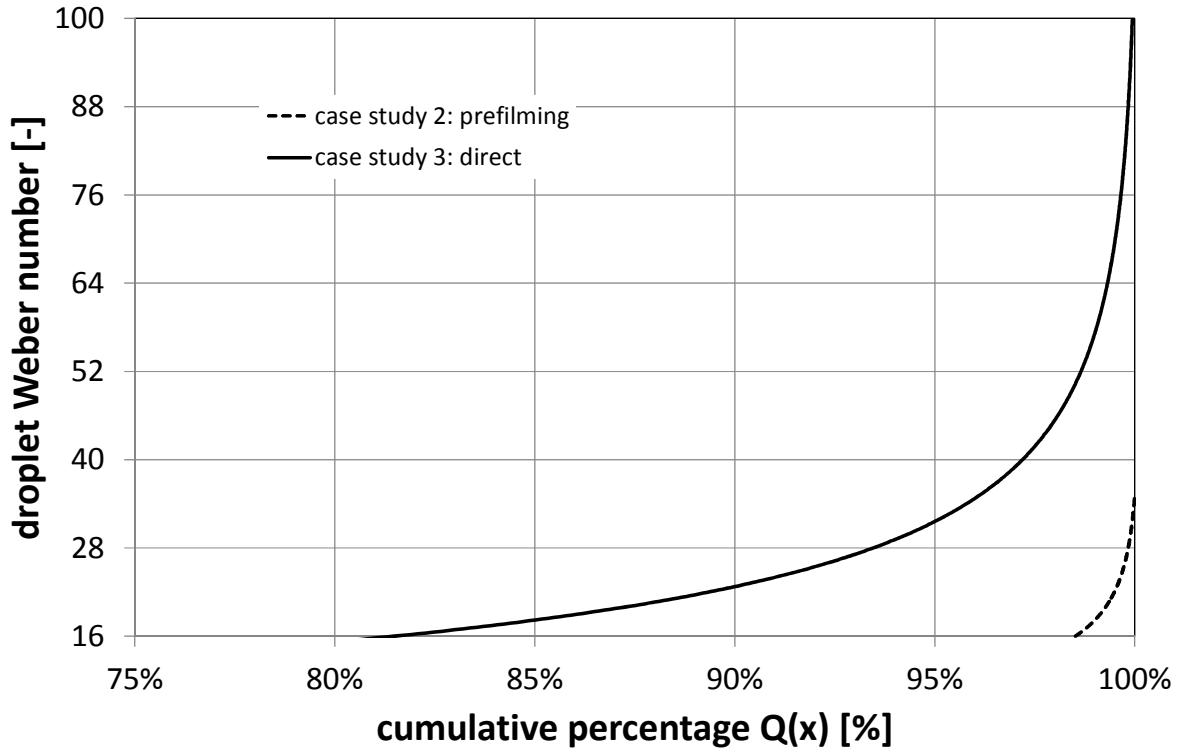

Figure 3.20: Droplet Weber number percentage due to secondary breakup. At Weber numbers higher than 16 (33,4 % of the droplets), bag breakup occurs, at We > 100 (0,65%), shear breakup is expected.

Table 3.22: Secondary breakup conditions and results (case studies 2 &3)

SECONDARY BREAKUP			**prefilming**	**direct**
primary droplet diameter	d_{50}	[µm]	14,3	15,6
relative velocity	v_{rel}	[m/s]	461,1	514,1
Bag Breakup Percentage	Q_{BB}	[%]	1,49%	18,65%
secondary diameter	$d_{sec,bag}$	[µm]	6,1	6,7
Shear Breakup Percentage	Q_{SB}	[%]	0,00%	0,06%
secondary diameter	$d_{sec,shear}$	[µm]	0,9	0,9
residueing primary droplets	$d_{prim,res}$	[µm]	13,8	12,4
resulting diameter	d_{sec}	[µm]	13,7	11,3

3.2.7. Droplet Acceleration, Spheroidization, Cooling and Solidification

Similar to chapter 3.1.7., droplet behavior after primary breakup is considered for atomizer case studies 2 and 3.

In figure 3.21, the characteristic time scales are shown for atomizer case study 2 (prefilming nozzle). For comparison, the corresponding data for the direct nozzle (atomizer case study 3) is introduced in figure 3.22 (dashed lines). We see that the "window" for secondary breakup is larger for direct nozzles, which is due to the higher relative velocity after primary breakup. The acceleration of the sheet during primary breakup is impressive and leads to fine ligaments after prefilming, but results in a much lower relative velocity for secondary breakup. Additionally, the cooling during primary breakup is massive (140°C) which results in a much shorter cooling time for droplets. It is well known that for prefilming nozzles, nozzle tip freezing is an issue and

particles freeze while they are in the process of disintegration. So figure 3.22 can contribute to an understanding of these phenomena.

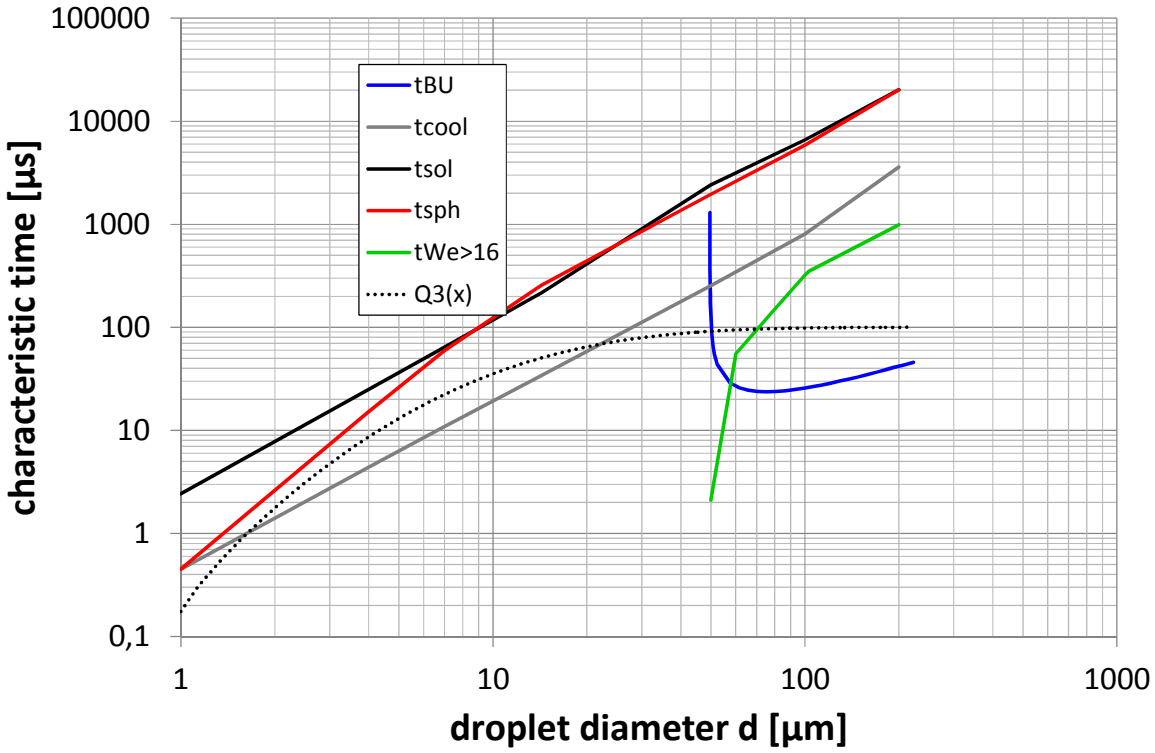

Figure 3.21: Prefilming nozzle: characteristic time scales for secondary breakup

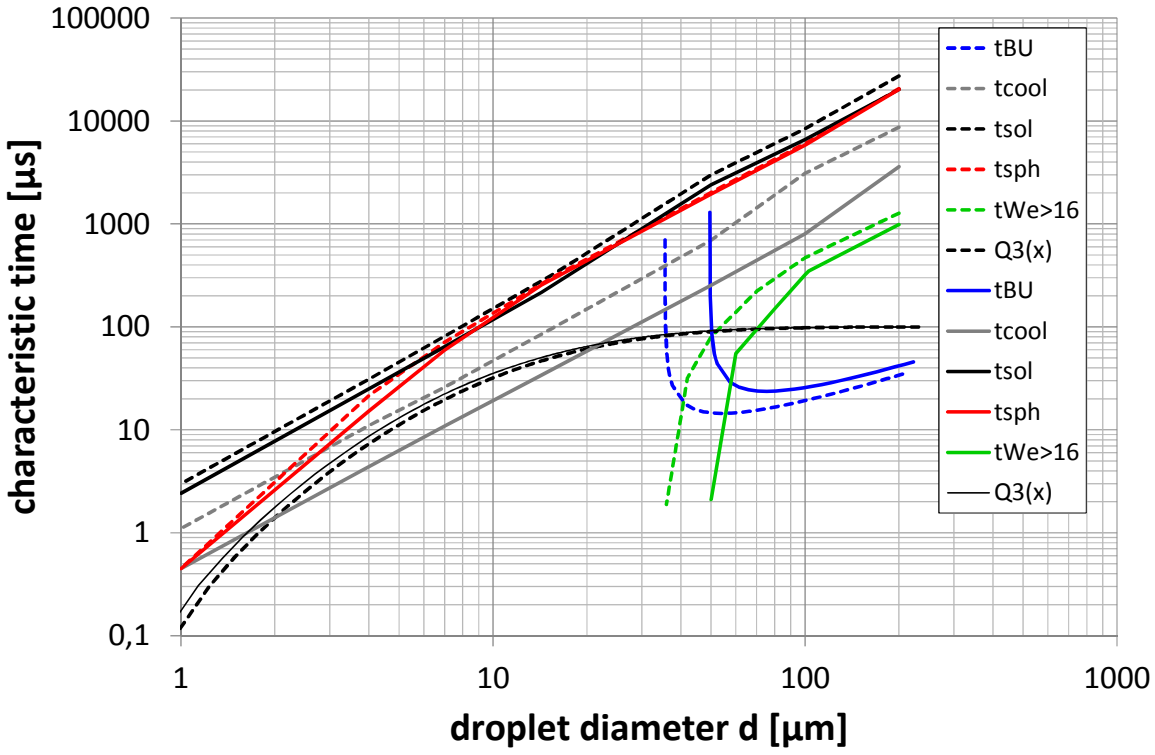

Figure 3.22: Comparison between prefilming and direct nozzles: characteristic time scales for secondary breakup; dashed lines for direct atomization, continuous lines for prefilming atomization

3.2.8. Times and Length Scales in Atomizer Case Studies 2 and 3

The times and length scales are listed in table 3.23 and 3.24. The two main differences are:

- ➔ the strong acceleration of the liquid sheet in case study 2 before primary breakup occurs, while – in our model – the jet (case study 3) is not accelerated
- ➔ the cooling of the liquid sheet in case study 2 (which is due to the formation of a very thin melt sheet before primary breakup), while in atomizer case study 3, cooling during primary breakup is two orders of magnitude lower.

It is important to understand that the effective relative velocity is assumed to have a local value influenced by boundary layer conditions to calculate primary breakup, where we would have to consider microscopic scales. For secondary droplet behavior (droplet acceleration and breakup, cooling and solidification, spheroidisation), macroscopic scales can be chosen and the overall mean relative velocity is used for calculations.

Table 3.23: Time and length scales in atomizer case study 2 (prefilming nozzle)

prefilming (case study 2)	distance travelled	time travelled	melt temperature	gas velocity	melt velocity	relative velocity
	[mm]	[µs]	[°C]	[m/s]	[m/s]	[m/s]
primary breakup (start)	0	0	875	544,2 // 302,5	0	544
primary breakup (end)	0,73	17,1	744,9	543,7 //302,5	85,4	458
ligament breakup	0,93	19,2	735,1	543,5	107,9	436
cooling	5,7	53,3	660	530	180	350
solidification	57,9	235,2	660	495	335	160

Table 3.24: Time and length scales in atomizer case study 3 (direct nozzle)

direct (case study 3)	distance travelled	time travelled	melt temperature	gas velocity	melt velocity	relative velocity
	[mm]	[µs]	[°C]	[m/s]	[m/s]	[m/s]
primary breakup (start)	0	0	875	550,7 // 272,3	2,4	548,3
primary breakup (end)	1,62	681,6	874,6	549,5 // 272,3	2,4	547,1
ligament breakup (end)	1,661	684,0	860,9	549,47	35,4	514
cooling	16,761	782	660	538,4	241,6	297
solidification	89,861	1009	660	489,2	365,6	124

3.2.9. Comparison to the Experiments of Ünal

Ünal did experiments with different nozzles at varying operating conditions [UNA1986, UNA1987, UNA1988, UNA1989a, UNA1989b, UNA1990] (which is the reason this specific geometry was chosen). At comparable conditions, Ünal produced powders with a d_{50} between 17µm and 27µm depending on various conditions which are discussed in [UNA1988].
The calculations presented here give finer results for the produced particle size. This can be explained by an effect which was discussed by Andersen [AND2009] who did high speed video analysis of the nozzle face finding that there is no continuous film on the ceramic nozzle front,

but only a part (say 30 to 50%) is covered by the melt film wandering around arbitrarily on the nozzle face. This leads to a thicker melt sheet, as 2 to 3 times of the mass is locally atomized at the same time – one could say that the local gas-to-liquid ratio is 2 to 3 times higher than for a perfect cylindrical sheet formation. The effect of this influence can be seen in figure 3.23 – the half sheet thickness h_F is strongly increasing and hence the resulting droplet diameter, too. With the explanations from Anderson, the deviation of our model to the results of Ünal [UNA1987] can partly be explained.

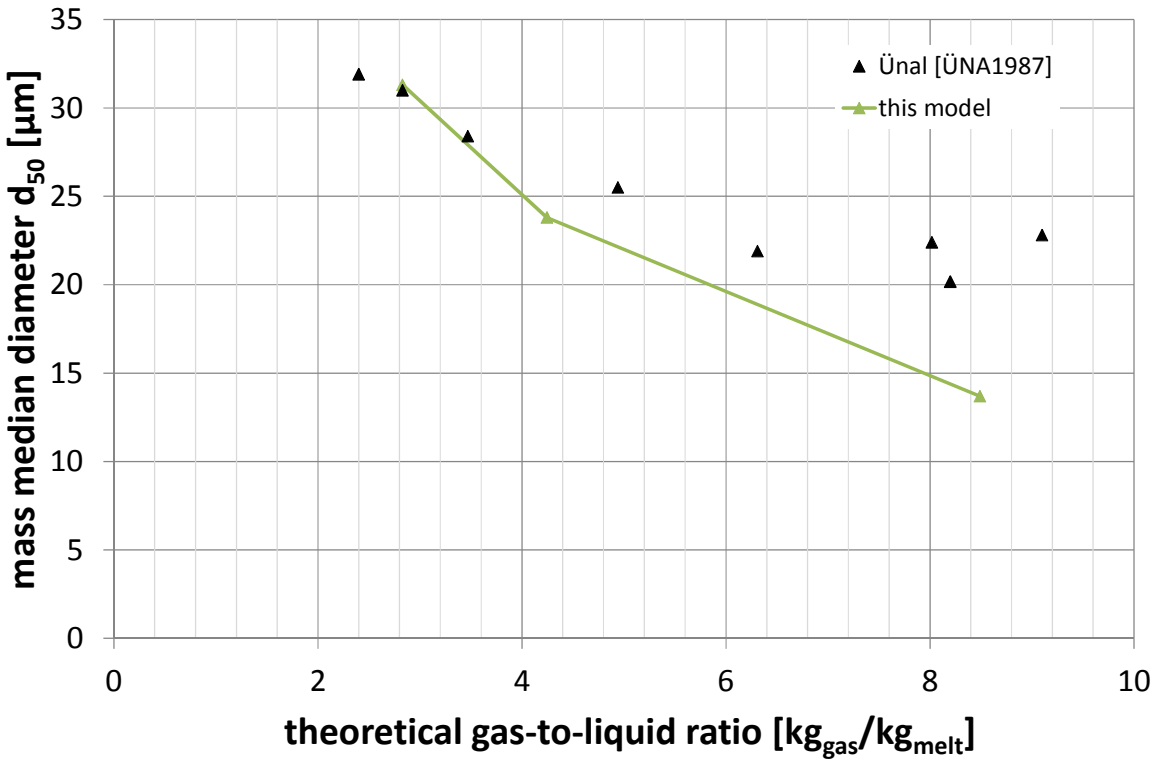

Figure 3.23: Mass median diameter as a function of the theoretical gas-to-liquid ratio – for comparison, the experimental results of Ünal are included in the figure; it is assumed here that – due to the effect described above, particle sizes do not decrease at gas-to-liquid ratios higher than 6 kg_{gas}/kg_{melt}

3.2.10. Analysis of Atomizer Case Study 3

Confined ("direct") nozzles and prefilming nozzles are expected to give comparable results at comparable atomization conditions. Hence, also in atomizer case study 3, a mass median diameter between 20 and 30 µm was expected. In a final step, it is now necessary to explain why the results in atomizer case study 3 are "better" than reality:

The model introduced by Bradley [BRA1973a] describes a single surface wave formed by a relative velocity between gas and liquid which stays constant (according to figure 2.8. in chapter 2.1.1). The mean conditions for this model are calculated (table 3.19). In real atomizer conditions, the phenomena are shown for different melt velocities (melt throughputs) in figure 3.24.

At high melt velocities (figure 3.24 left picture), calculated breakup length is long. At this stage, we expect that the local gas velocity is decreasing from nozzle exit due to momentum

conservation, as ligaments have to be shed off the melt surface and are accelerated. Hence, the disintegration of the melt at longer distances from nozzle exit is less efficient and it is possible that breakup regime shifts from atomization mode to second-wind induced regime.

At decreasing melt velocities, the calculated breakup length becomes smaller and smaller and reaches a value (say 0), where no jet can be observed anymore, but the melt turns into a cylindrical sheet (figure 3.24 right picture). At the operating conditions discussed in atomizer case study 3, we calculated a breakup length somewhere in between these two extremes, and a sketch to scale (breakup length x_{BU}=1,62mm) is seen in figure 3.24 central picture. As the calculated decrease of the jet surface is much higher than the half opening angle of the surrounding gas, it is not expected that primary breakup takes place in the Bradley mode ("shedding") for the whole melt cone, but only for a part of it, while in the center of the cone, again, a shift in atomization mode is to be expected (from atomization regime to second or first wind-induced breakup). This, of course, leads to a much coarser primary breakup result.

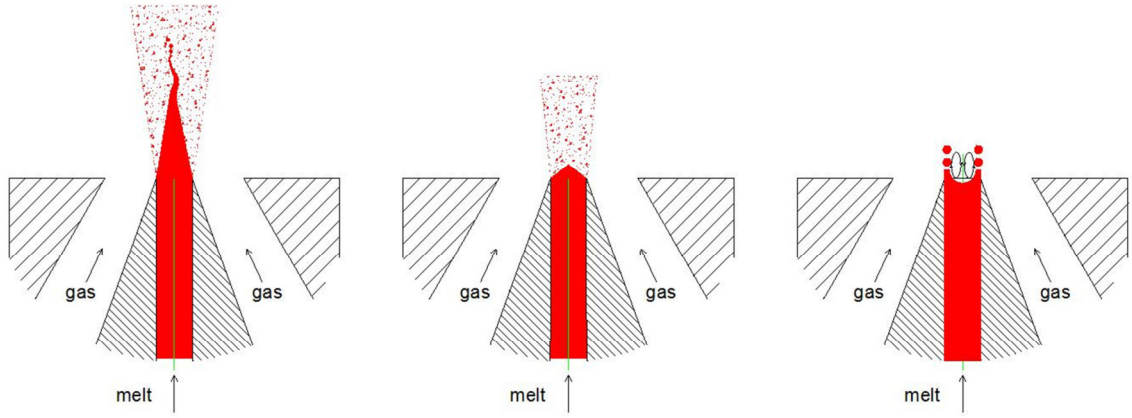

Figure 3.24: Jet breakup at decreasing melt production rates (from left to right): breakup length decreases and finally the jet is transformed into a cylindrical sheet.

4. Summary, Suggestions for Further Work

In this study, a complete model for the gas atomization process of metal melts was established taking into account the following steps of the atomization process:

- ➔ The formation of the gas velocity field
- ➔ Primary breakup of the melt into ligaments and droplets
- ➔ Secondary breakup of the droplets
- ➔ Spheroidisation, Cooling and solidification of the droplets

Goal of the model is to give a sufficiently exact image of the "real" atomization process, which is nevertheless simple and can be applied on new spray problems without efforts. This was achieved by applying realistic gas atomization processing variables on breakup models (primary and secondary ones) chosen from relevant publications on this topic.

With the present model, it is possible to improve existing atomization systems by analyzing the different steps during breakup. Any processing issues such as powder fineness, energy costs, non-spherical powders, nozzle freezing, cooling rates, etc. can be detected and ameliorated. Hence, any necessary changes in an atomization system (geometry, atomizing parameters, materials, boundary conditions) can also be predicted and their influences on product properties will be understood.

This model was applied on 3 commonly used twin fluid atomization systems (open jet, prefilming and direct confined nozzles) and a comparison to existing experimental data was given. Though the model results fit astonishingly well to the experimental data, the model implies several drawbacks which shall be discussed here.

a) Gas Velocity Field

In the model presented here, gas velocity is simply considered as a one dimensional quantity, oriented in line with the nozzle axis, while the real 3D-situation is – of course – very complex. In addition, the three-dimensional gas flow is influenced by compressible flow phenomena and gas/melt interactions which have to be considered. The available literature concerning these influences is focused on very specific geometrical and operational conditions. To prove and enhance the value of this atomization model, the exemplarily application of computational fluid dynamics and/or PIV measurements on the gas flow field can be a helpful and forward-looking step.

b) Primary Breakup

Primary breakup is described in a simplified way assuming that we have got exact and axisymmetric hollow cones (case study 1), a hollow cylinder (case study 2) and a full cone (case study 3). These "perfect" breakup descriptions deviate from asymmetric, fluctuating "real breakup" and therefore only inaccurately represent reality. One step to clarify primary breakup conditions can be a high speed video analysis of the melt sheet formation (case studies 1 and 2) and of the melt jet breakup at varying operating conditions (and material systems).

c) Secondary Breakup

Secondary breakup, cooling and solidification of single drops is well documented in literature, which is also represented in our model. Although swarm properties, coalescence or surface adsorption (satelliting) are not considered in this model, a good overview of secondary breakup is given.

d) Spheroidisation, Cooling and Solidification, Oxidation

To achieve a first access to spheroidisation processes, an old model [RAO1973] was adapted for our purposes. This is only a first step to a better understanding of droplet spheroidisation during atomization and a much deeper insight into the problem is necessary. Nevertheless, a reasonable time scale for the process was achieved and influences of materials' data and droplet size as well as dynamic flow conditions in the spray were implemented. Further work could include e.g. high speed video analysis of droplets in gas flow or a stochastic analysis of the shape of particles produced at varying atomization conditions.

Cooling process was analyzed by an existing model and the results fit well to those of other researchers, while the solidification process was simplified by neglecting microscopic phenomena inside the particle during the solidification process. For these purposes, concepts discussed e.g. by Delplanque et al. [DEL2000] or Grant and Cantor [GRA2000] can be included in our model.

A further drawback of our model is the fact that oxidation processes are not included – these are very complex and strongly depending on the chosen gas/alloy material system, but also on operating conditions. Of course, we have to be aware that oxidation also influences the cooling and solidification process (a solid oxide on the droplet surface works as a barrier for heat exchange), but furthermore the breakup process and the spheroidisation are affected by oxide layers on the melt droplet surface. Additionally, the oxide layer has got strong influences on powder applications and it cannot be ignored. The available literature on this topic is rare and strongly related to specific material systems. Again, powders produced by the three twin fluid atomization systems discussed here have to be analyzed, and a physical model with a broad view on the different aspects of atomization has to be established.

e) Melt Superheat

In our model, the influence of the melt superheat is only considered as a matter of cooling time, while the effects of the temperature on melt properties such as surface tension or viscosity are not analyzed in detail here. Some aspects of these influences are discussed in [STR1996] or [OUY2007]. In a future version of this model, the temperature dependent melt property variations can possibly be included into the model.

f) Gas Properties

Gas properties – also as a function of temperature – are well included in our calculations. As a drawback, heat transfer is only calculated from the metal to the gas, while gas temperature is kept constant. Two phase coupling in heat exchange is an important next step to improve our model.
Furthermore, geometrical boundary conditions of the nozzle surroundings (chiller chamber, cooling gas flow) were not defined, so the present approach is incomplete. At the stage of primary breakup, this influence can clearly be neglected, while it becomes more and more important with increasing distance from nozzle exit (cooling, spheroidisation, solidification). To include these aspects into our calculations, the whole atomizer geometry has to be defined up to the stage of solidification.

5. References

[ALI2008] Aliseda, A., Hopfinger, E. J., Lasheras, J. C., Kremer, D. M., Berchielli, A., & Connolly, E. K. (2008). Atomization of viscous and non-Newtonian liquids by a coaxial, high-speed gas jet. Experiments and droplet size modeling. International Journal of Multiphase Flow, 34(2), 161-175.

[ALL1991] Aller, A. J., & Losada, A. (1991). Models in the Metal Powders Atomization. Powder Metallurgy Science & Technology, 2(2), 13-37.

[AND1955] Anderson, A. R. (1955). Characteristics of free supersonic jets exhausting into quiescent air. Journal of Jet Propulsion, 25(1), 13-15.

[APC2015] http://advancedpowders.com (2016-12-25)

[ARA1985] Arai, T., & Hashimoto, H. (1986). Disintegration of a thin liquid sheet in a cocurrent gas stream. International Journal of Turbo and Jet-Engines, 3(4), 301-306.

[BAS1989] Baszczuk, C. M., & Quimby, B. A. (1989). Method and apparatus for making metal powder . Patent US4810288.

[BAT1989] Battezzati, L., & Greer, A. L. (1989). The viscosity of liquid metals and alloys. Acta Metallurgica, 37(7), 1791-1802.

[BER99] Bergmann, D., Heck, U., Fritsching, U., & Bauckhage, K. (1999). Particle Size Distribution Width in Gas Atomization of Molten Metals. Advances in Powder Metallurgy and Particulate Materials, 1(1/3), 1-57.

[BIC1990] Bich, E., Millat, J., & Vogel, E. (1990). The viscosity and thermal conductivity of pure monatomic gases from their normal boiling point up to 5000 K in the limit of zero density and at 0.101325 MPa. Journal of physical and chemical reference data, 19(6), 1289-1305.

[BRA1973a] Bradley, D. (1973). On the atomization of liquids by high-velocity gases. Journal of Physics D: Applied Physics, 6(14), 1724.

[BRA1973b] Bradley, D. (1973). On the atomization of a liquid by high-velocity gases: II. Journal of Physics D: Applied Physics, 6(18), 2267.

[BRO1990] Brooks, R. G., Leatham, A., & Coombs, J. (1990). Deposition of metallic products using relatively cold solid particles. Patent US4926923

[DEL2000] Delplanque, J. P., Lavernia, E. J., & Rangel, R. H. (2000). Analysis of In-Flight Oxidation During Reactive Spray Atomization and Deposition Processing of Aluminum. Journal of Heat Transfer, 122(1), 126-133.

[DOM1963] Dombrowski, N., & Johns, W. R. (1963). The aerodynamic instability and disintegration of viscous liquid sheets. Chemical Engineering Science, 18(3), 203-214.

[DOP2008] Dopler, M. (2008). Process for production of particles of free-flowing material and spraying unit therefor. Patent EP1930071.

[EGR2010] Egry, I., Ricci, E., Novakovic, R., & Ozawa, S. (2010). Surface tension of liquid metals and alloys—recent developments. Advances in colloid and interface science, 159(2), 198-212.

[EUS1998] Eustathopoulos, N., Drevet, B., & Ricci, E. (1998). Temperature coefficient of surface tension for pure liquid metals. Journal of crystal growth, 191(1), 268-274.

[FAE1995] Faeth, G. M., Hsiang, L. P., & Wu, P. K. (1995). Structure and breakup properties of sprays. International Journal of Multiphase Flow, 21, 99-127.

[FRI97] Fritsching, U., Heck, U., & Bauckhage, K. (1997). The Gas-Flowfield in the Atomization Region of a Free-Fall-Atomizer. International Journal of Fluid Mechanics Research, 24(4-6), 893-902

[FUN2006] Funada, T., Joseph, D. D., Saitoh, M., & Yamashita, S. (2006). Liquid jet in a high Mach number air stream. International journal of multiphase flow, 32(1), 20-50.

[GIO1999] Giordanengo, B., Benazzi, N., Vinckel, J., Gasser, J. G., & Roubi, L. (1999). Thermal conductivity of liquid metals and metallic alloys. Journal of non-crystalline solids, 250, 377-383.

[GOR1959] Gordon, G. D. (1959). Mechanism and speed of breakup of drops. Journal of Applied Physics, 30(11), 1759-1761.

[GRA1991] Graf, W., Pötschke, J., Sibum, H., & Weiglin, W. (1991). Die Herstellung gasverdüster Metallpulver. Metall, 45(4), 348-354.

[GRA1993] Grant, P. S., Cantor, B., & Katgerman, L. (1993). Modelling of droplet dynamic and thermal histories during spray forming—I. Individual droplet behaviour. Acta Metallurgica et Materialia, 41(11), 3097-3108.

[GRA2012] Gratzer, P. (2012). Modellierung der Oberflächeneigenschaften von Aluminiumpulver. Bachelor-Thesis, University of Leoben

[GRE1961] Gretzinger, J., & Marshall, W. R. (1961). Characteristics of pneumatic atomization. AIChE Journal, 7(2), 312-318.

[HAL1917] Hall, E. J. (1917). Process for Disintegrating Metal. Patent US1659291.

[HAL1919] Hall, E. J. (1919). Nozzle Intended to use in disintegrating apparatus. Patent US1545253.

[HEC1998] Heck, U. (1998). Zur Zerstäubung in Freifalldüsen. VDI-Verlag, Düsseldorf. ISBN 3183348071

[HEC2000] Heck, U., Fritsching, U., & Bauckhage, K. (2000). Gas flow effects on twin-fluid atomization of liquid metals. Atomization and Sprays, 10(1).

[HEL1970] Hellmann, P. & Backström, S. (1970). Verfahren und Vorrichtung zur Herstellung eines Pulvers durch Versprühen eines geschmolzenen Materials, Patent DE2057862.

[JOS1999] Joseph, D. D., Belanger, J., & Beavers, G. S. (1999). Breakup of a liquid drop suddenly exposed to a high-speed airstream. International Journal of Multiphase Flow, 25(6), 1263-1303.

[KLA1984] Klar, E. (1984). Metals handbook: Powder metallurgy. Metals Park, Ohio. ISBN 9780871701541

[KOR1984] Koria, S. C., & Lange, K. W. (1984). An experimental study on the behaviour of an underexpanded supersonic gas jet. Archiv für das Eisenhüttenwesen 55(9), 427-432.

[KOW1996] Kowalewski, T. A. (1996). On the separation of droplets from a liquid jet. Fluid Dynamics Research, 17(3), 121-145.

[KUL1991] Kull, H. J. (1991). Theory of the Rayleigh-Taylor instability. Physics Reports 206 No.5, 197-325

[KUT1971] Kutkin, A. I., Fishman, B. D., & Valov, M. E. (1971). Investigation of the industrial melt atomization process by the technique of high-speed motion picture photography. Powder Metallurgy and Metal Ceramics, 10(2), 98-102.

[LAW1985] Lawley, A., & Doherty, R. D. (1985). The Particle Metallurgy/Rapid Solidification Interface: Atomization Models and Mechanisms. Advanced High-Temperature Alloys: Processing and Properties, 65-71.

[LAW1992] Lawley, A. (1992). Atomization: the production of metal powders. Metal Powder Industries Federation, Princeton, New Jersey. ISBN 1878954156

[LEF1980] Lefebvre, A. H. (1980). Airblast atomization. Progress in Energy and Combustion Science, 6(3), 233-261.

[LI1992] Li, H. S., & Kelly, R. E. (1992). The instability of a liquid jet in a compressible airstream. Physics of Fluids A: Fluid Dynamics, 4(10), 2162-2168.

[LIA1993] Liang, X., & Lavernia, E. J. (1993). Solidification and microstructure evolution during spray atomization and deposition of Ni3Al. Materials Science and Engineering: A, 161(2), 221-235.

[LIN1998] Lin, S. P., & Reitz, R. D. (1998). Drop and spray formation from a liquid jet. Annual Review of Fluid Mechanics, 30(1), 85-105.

[LIN2007] Linka, S. (2003). Untersuchung der Eigenschaften von Schlacken und Schmelzen in technischen Feuerungen. Abschlussbericht zum Forschungsvorhaben AiF 12597 N, Ruhr-Universität Bochum, Bochum, Germany.

[LIU2000] Liu, H. (2000). Science and Engineering of Droplets: Fundamentals and Applications. William Andrew 1edition, ISBN 9780815514360

[LUB1970] Lubanska, H. (1970). Correlation of spray ring data for gas atomization of liquid metals. JOM, 22(2), 45-49.

[MAD2007] Madsen, J. (2006). Computational and experimental study of sprays from the breakup of water sheets. PhD-Thesis, Aalborg University.

[MAR1873] Marriott, W. (1873). Improvements in the manufacture of salts and oxides of lead, and in apparatus therefor. British Patent 3322.

[MAR2002] Markus, S., Fritsching, U., & Bauckhage, K. (2002). Jet break up of liquid metal in twin fluid atomisation. Materials Science and Engineering: A, 326(1), 122-133.

[MAT2005] Mates, S. P., & Settles, G. S. (2005). A study of liquid metal atomization using close-coupled nozzles, Part 1: Gas dynamic behavior. Atomization and Sprays, 15(1).

[MEH1988] Mehrotra, S. P. (1988). Mathematical Modelling of Gas Atomization Process for Metal Powder Production.--I. Powder Metall. Int., 13(2), 80-84.

[MUR2000] Murakami, E., & Papamoschou, D. (2000). Mixing layer characteristics of coaxial supersonic jets. In 6th Aeroacoustics Conference and Exhibit (p. 2060).

[NAI1971] Naida, Y. I. (1971). Deformation and disintegration of liquid particles by a gas stream. Soviet Powder Metallurgy and Metal Ceramics, 10(3), 187-190.

[OHN1936] Ohnesorge, W. V. (1936). Die Bildung von Tropfen an Düsen und die Auflösung flüssiger Strahlen. ZAMM-Journal of Applied Mathematics and Mechanics/Zeitschrift für Angewandte Mathematik und Mechanik, 16(6), 355-358.

[ORO1987] O'Rourke, P. J., & Amsden, A. A. (1987). The TAB method for numerical calculation of spray droplet breakup (No. LA-UR-87-2105-Rev.; CONF-871142-1-Rev.). Los Alamos National Lab., NM (USA).

[OUY2007] Ouyang, H. W., Xin, C. H. E. N., & Huang, B. Y. (2007). Influence of melt superheat on breakup process of close-coupled gas atomization. Transactions of Nonferrous Metals Society of China, 17(5), 967-973.

[RAO1972] Rao, P., & Tallmadge, J. A. (1971). Change of shape of metal droplets in quench atomization. Proceedings of the 1971 Powder Metallurgy Conference, MPIF1972, NY, 251-266

[RAO1973] Rao, P. (1973). Shape and other Properties of Gas Atomized Powders. Ph.D. Thesis, Drexel University

[RAO1981] Rao, K. P., & Mehrotra, S. P. (1980). Effect of process variables on atomization of metals and alloys. Modern Developments in Powder Metallurgy,, 12, 113-130.

[RAY1878] Rayleigh, L. (1878). On the instability of jets. Proceedings of the London mathematical society, 1(1), 4-13.

[REI1978] Reitz, R. D. (1978). Atomization and other breakup regimes of a liquid jet. Ph.D. Thesis, Princeton University

[REI1986] Reitz, R. D., & Bracco, F. V. (1986). Mechanisms of breakup of round liquid jets. Encyclopedia of fluid mechanics, 3, 233-249.

[ROD2005] Rodd, L. E., Scott, T. P., Cooper-White, J. J., & McKinley, G. H. (2004). Capillary break-up rheometry of low-viscosity elastic fluids. Appl. Rheol. 15 (2005) 12-27

[SCHL1956] Schlichting, H. (1956). Grenzschicht-Theorie. Braun-Verlag, Karlsruhe, ISBN 9783540329855

[SCHN2003] Schneider, B. M. (2003). Experimentelle Untersuchungen zur Spraystruktur in transienten, verdampfenden und nicht verdampfenden Brennstoffstrahlen unter Hochdruck. Ph.D.-Thesis, ETH Zürich

[SCHR2003] Schreithofer, Chr. (2003). Strömungsverhalten des Hüllgasstrahls in Zerstäuberdüsen bei der Verdüsung von Metallschmelzen. Master Thesis, University of Leoben

[SEE1973] See, J. B., Runkle, J. C., & King, T. B. (1973). The disintegration of liquid lead streams by nitrogen jets. Metallurgical Transactions, 4(11), 2669-2673.

[SEE1978] See, J. B., & Johnston, G. H. (1978). Interactions between nitrogen jets and liquid lead and tin streams. Powder Technology, 21(1), 119-133.

[SEN1999] Senecal, P. K., Schmidt, D. P., Nouar, I., Rutland, C. J., Reitz, R. D., & Corradini, M. L. (1999). Modeling high-speed viscous liquid sheet atomization. International Journal of Multiphase Flow, 25(6), 1073-1097.

[SIZ1991] Sizov, A. M. (1991). Dipersion of Melts by Supersonic Gas Jets. Metallurgija Publ. Moskau. Translated by IWT Bremen.

[SLA1981] Schlackenatlas. Verein Dt. Eisenhüttenleute. Verlag Stahleisen, Düsseldorf. ISBN 9783514002289

[STE2004] Steindl, Franz (2004). Modellversuche zur Mikrogranulation von Hochofenschlacke. Master Thesis, University of Leoben

[STR1996] Straus, J. T., & Miller, S. (1996). Effect of melt superheat on powder characteristics produced by close-coupled gas atomization. Advances in Powder Metallurgy and Particulate Materials -I 996. 55-66

[SUT1893] Sutherland, W. (1893). LII. The viscosity of gases and molecular force. The London, Edinburgh, and Dublin Philosophical Magazine and Journal of Science, 36(223), 507-531.

[TOR2000] Tornberg, C. (2000). Verfahren und Vorrichtung zur Herstellung von Metallpulver durch Gasverdüsung. Patent EP1022078.

[UNA1986] Ünal, A., & Robertson, D. G. C. (1986). Pilot plant gas atomizer for rapidly solidified metal powders.

[UNA1987] Ünal, A. (1987). Effect of processing variables on particle size in gas atomization of rapidly solidified aluminium powders. Materials Science and Technology, 3(12), 1029-1039.

[UNA1988] Ünal, A. (1988). Influence of nozzle geometry in gas atomisation of rapidly solidified aluminium alloys. Materials science and technology, 4(10), 909-915.

[UNA1989a] Ünal, A. (1989). Liquid break-up in gas atomization of fine aluminum powders. Metallurgical Transactions B, 20(1), 61-69.

[UNA1989b] Ünal, A. (1989). Flow separation and liquid rundown in a gas-atomization process. Metallurgical Transactions B, 20, 613-622.

[UNA1990] Ünal, A. (1990). Production of rapidly solidified aluminium alloy powders by gas atomisation and their applications. Powder metallurgy, 33(1), 53-64.

[UNA1998] Ünal, A., Leon, D. D., Gurganus, T., & Hildeman, G. J. (1998). Production of aluminum and aluminum-alloy powder. ASM handbook, 7, 148-159.

[VAR1977] Vargaftik, N. B., & Yakush, L. V. (1977). Temperature dependence of thermal conductivity of helium. Journal of Engineering Physics and Thermophysics, 32(5), 530-532.

[VDI2006] VDI-Wärmeatlas 10. Auflage, Springer Berlin Heidelberg, 2005. ISBN 9783642199806

[VIL2007] Villermaux, E. (2007). Fragmentation. Annu. Rev. Fluid Mech., 39, 419-446.

[WAL1969] Wallis, G. B. (1969). One-dimensional two-phase flow. McGraw-Hill Companies, University of Michigan. ISBN 9780070679429

[WEN1984] Wentzell, J. M. (1984). Method of an apparatus for making metal powder. Patent US4610719.

[WIG1964] Wigg, L. D. (1964). Drop Size Prediction for Twin Fluid Atomizers. J. Inst. Fuel, 27, 500-505.

[YUL1982] Yule, A. J., Seng, C. A., Felton, P. G., Ungut, A., & Chigier, N. A. (1982). A study of vaporizing fuel sprays by laser techniques. Combustion and Flame, 44(1), 71-84.

[YUL1994] Yule, A. J., & Dunkley, J. J. (1994). Atomization of melts for powder production and spray deposition (No. 11). Oxford University Press, USA. ISBN 9780198562586

[ZHO1992] Zhou, Z. W., & Lin, S. P. (1992). Absolute and convective instability of a compressible jet. Physics of Fluids A: Fluid Dynamics, 4(2), 277-282.

6. Appendix – Material Properties

A) Gas Properties

a) Dynamic Viscosity of Gases:

The dynamic viscosity of gases is strongly depending on temperature and can be calculated using Sutherland's law [SUT1893], the necessary coefficients can be taken from table 6.1.

$$\eta_{gas}(T) = \eta_{gas,0} * \left(\frac{T}{T_0}\right)^{\frac{3}{2}} * \frac{T_0+S}{T+S} \qquad (6.1)$$

η_{gas} = dynamic viscosity at temperature T [Pa·s]
$\eta_{gas,0}$ = dynamic viscosity at reference temperature T_0
T= gas temperature [K]
T_0= reference temperature [K]
S= Sutherland constant [K]

Table 6.1: Sutherland Constants for Different Gases

	η_0 x 10^5	T_0	S
	[kg/ms]	[K]	[K]
air	1,716	273,15	110,4
nitrogen	1,781	300,55	111
oxygen	2,018	292,25	127
argon	2,125	273,15	144,4
helium	1,864	273,15	97,4

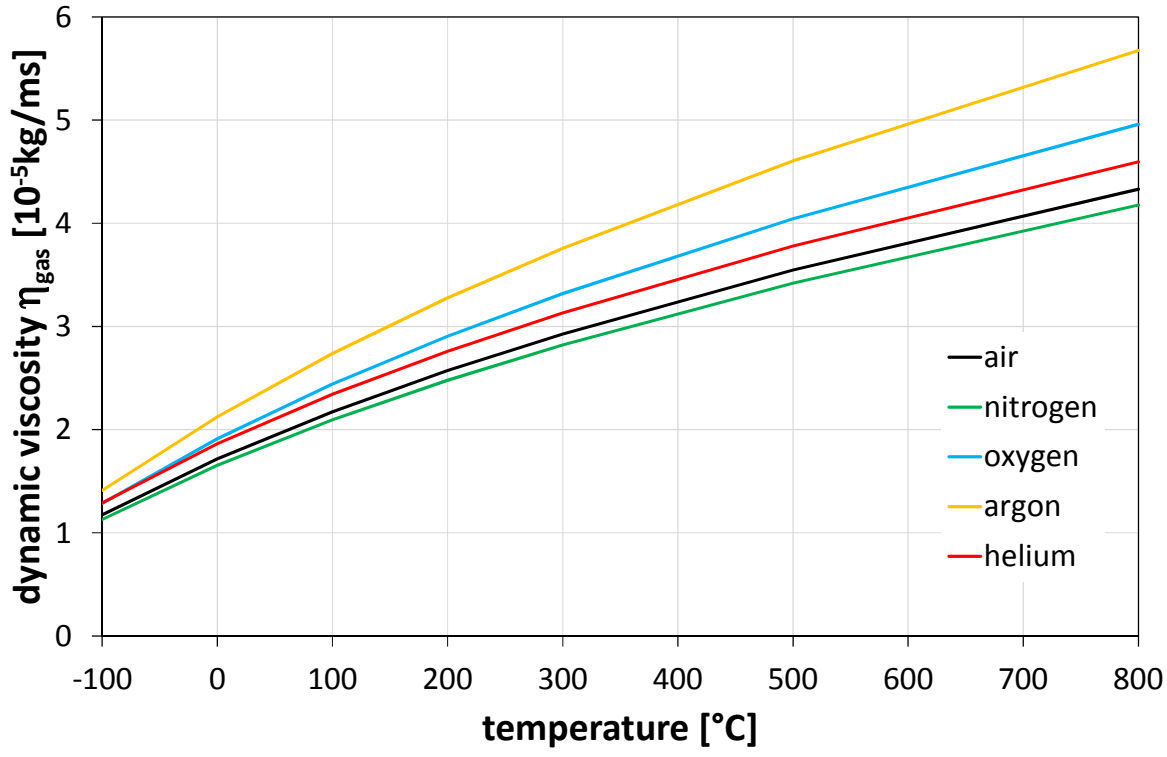

Figure 6.1: Dynamic viscosity of gases as a function of temperature [SUT1893]

b) Gas Density:

Gas density is calculated using ideal gas equation – the deviations from real gas conditions at pressures and temperatures used here (< 100 bar, > -50 °C) can be neglected. The necessary parameters are taken from table 6.2 [VDI2006].

$$\frac{p}{\rho} = R_m * T \qquad (6.2)$$

Table 6.2: Molar Mass, Specific Gas Constants, Gas Densities at 0°C, 1 bar Absolute Pressure

GAS	M	R_m	ρ_{gas} (0°C, 1bar)	a (0°C, 1bar)	κ
	[g/mol]	[J/kgK]	[kg/m^3]	[m/s]	[-]
air	28,96	287,2	1,293	331,5	1,402
nitrogen	28,01	296,8	1,25	337	1,4
oxygen	32,00	259,8	1,429	315	1,4
helium	4,003	2077,1	0,1785	970	1,67
argon	39,95	208,1	1,784	301	1,67

c) Heat Capacities of Gases:

Heat capacities can be calculated with the following relation, factors A, B, C, D, E taken from table 6.3 [VDI2006]:

$$c_{p,gas}(T) = A + B * T[K] + C * T[K]^2 + D * T[K]^3 + \frac{E}{T[K]^2} \qquad (6.3)$$

Tab. 6.3: Factors A, B, C, D, E for the calculation of gas heat capacity

gas	A	B	C	D	E
air	1070,3	-0,564	0,001507	-0,000001102	-0,000000014
nitrogen	1049,9	-0,158	0,000439	0,000000660	-0,000000229
oxygen	885,4	0,071	0,000277	-0,000000143	-0,000000004
helium	5193,1	0	0	0	0
argon	520,3	0	0	0	0

For noble gases, heat capacity c_p is not depending on temperature; for the others, c_p is slightly increasing. For our purposes, working with a constant heat capacity $c_{p,500°C}$ is exact enough (deviation < 8%). See also figure 6.2.

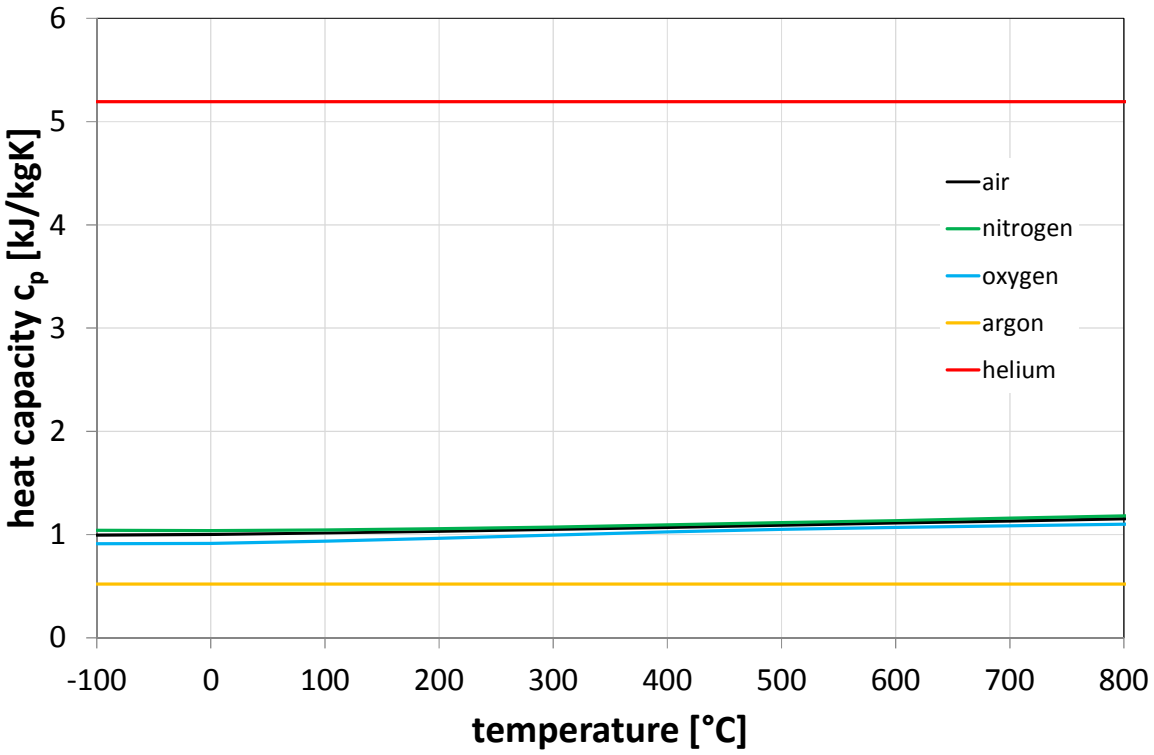

Figure 6.2: Heat capacity of gases as a function of gas temperature

d) Thermal Conductivity of Gases:

Conductivity of gases is strongly depending on gas temperature and can be taken from fig. 6.3. The implementation into our model was done by applying a polynomic fit on the available data (equations 6.4 – 6.8). Data for air, nitrogen and oxygen is taken from [VDI2006], for Helium, data is taken from [VAR1977] and for Argon from [BIC1989].

$$\lambda_{air} = -1{,}54352970904557 * 10^{-8} * T[°C]^2 + 0{,}0000715239175672185 * T[°C] + 0{,}0242546733 \quad (6.4)$$

$$\lambda_{N2} = 7{,}83816389940339 * 10^{-18} T[°C]^5 - 3{,}42516226965961 * 10^{-14} T[°C]^4 + 5{,}33618380863331 * 10^{-11} T[°C]^3 - 4{,}14129527558329 * 10^{-8} T[°C]^2 + 0{,}000073674273457663 * C4 + 0{,}0240455544 \quad (6.5)$$

$$\lambda_{O2} = -1{,}42498156963512 * 10^{-8} * T[°C]^2 + 0{,}0000749773898720715 * T[°C] + 0{,}0237965186 \quad (6.6)$$

$$\lambda_{He} = 0{,}718 * 10^{-11} * T[K]^3 - 0{,}618 * 10^{-7} * T[K]^2 + 0{,}000362 * T[K] + 0{,}0476 \quad (6.7)$$

$$\lambda_{Ar} = -7{,}31081669004475 * 10^{-15}T[°C]^4 + 2{,}34005744235021 * 10^{-11}T[°C]^3 - 3{,}25851985991544 * 10^{-8}T[°C]^2 + 0{,}0000513238265226914 * C4 + 0{,}0164093194 \quad (6.8)$$

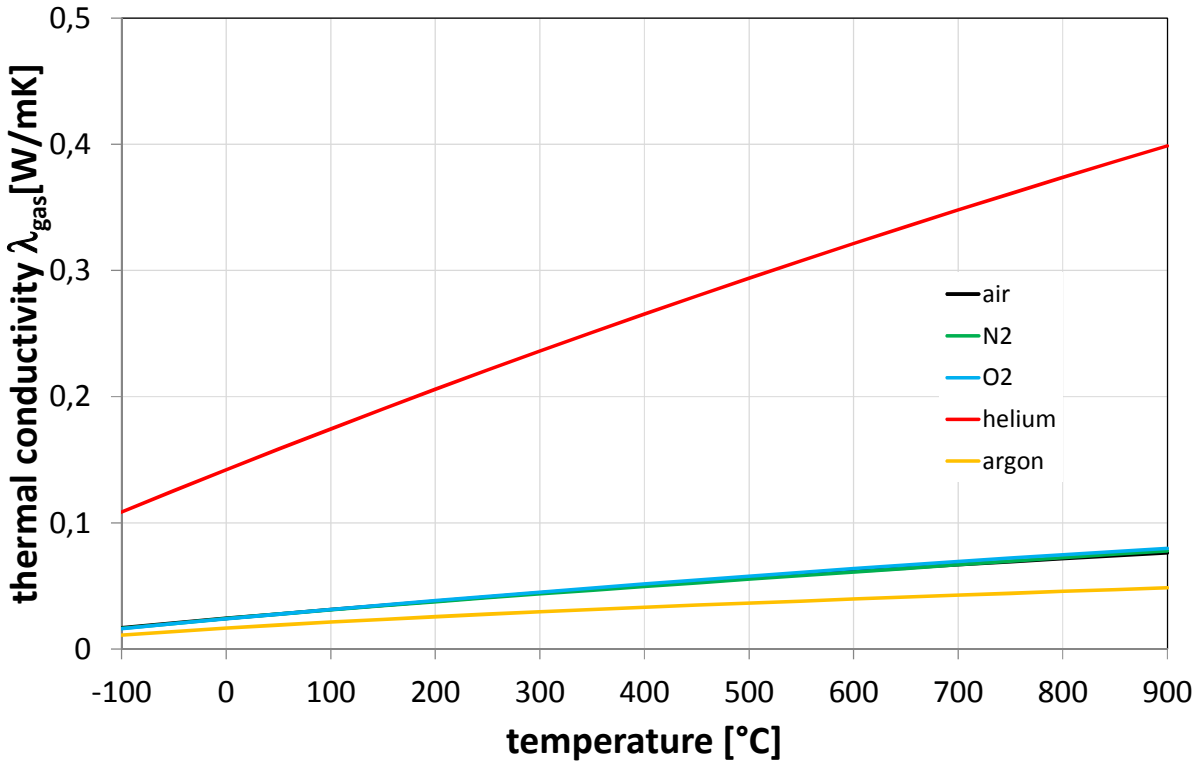

Figure 6.3: Thermal conductivity of gases

e) Sonic Velocity of Gases:

Again, we simplify assuming that the gases used here are ideal. Hence, sonic velocity can be calculated using the following relation:

$$a_{gas} = \sqrt{\kappa \frac{p_{gas}}{\varrho_{gas}}} = \sqrt{\kappa R_m T} \quad (6.9)$$

Values for κ and R_m can be taken from table 6.2.

B) Melt Properties

Melt properties are strongly depending on the exact composition. High purity materials (99,999%) may have e.g. surface tensions or thermal conductivities much higher (factor up to 10) than materials of standard composition (e.g. 99,8% purity), while the influence of alloys on melt properties cannot be discussed here at all. Secondly, melt properties are strongly depending on temperature. As an example, it is well known that viscosity is decreasing when melt temperature is increasing. Surface tension is slightly decreasing, when temperature rises, while thermal conductivities are slightly increasing with temperature. It is also interesting to see

that properties such as thermal conductivity, density or heat capacity of melts in the solid phase are quite different to those in the liquid phase.

To ease our calculations here (and also to make them comparable to other publications), constant values for all melt properties were chosen (see table 6.4). For comparison and further understanding, the theoretical calculations were also performed with slag – the properties of the slag we used at different temperatures can also be taken from table 6.4. Influences on liquid metals' and alloys' viscosity are described in [BAT1989]. Many numbers for density, heat capacity and thermal conductivity can be found in [VDI2006]. More information on thermal conductivity is provided in [GIO1999]. Surface tension is discussed in [EGR2010] and [EUS1998]. Further information on slag properties can be taken from [SLA1981] and [LIN2007].

Table 6.4: Liquid properties of the materials used in this study

LIQUID		**water**	**tin**	**aluminium**	**copper**	**iron**	**slag**
molar mass m_{Mol}	[g/mol]	18,02	118,69	26,98	63,54	55,874	*62**
melting point T_{sol}	[°C]	0	232	660	1083	1536	*1150***
evaporating point T_{evap}	[°C]	100	2270	2060	2600	3200	
heat of fusion Δh_{fus}	[kJ/kg]	333,5	61	397	210	250	300
solid state:							
density ρ_{solid}	[kg/m^3]	926	7278	2700	8960	7870	
heat capacity $c_{p,solid}$	[J/kgK]	4180	235	1040	450	385	
thermal conductivity λ_{solid}	[W/mK]	2,3	64	230	350	50	
melt state:							
Density ρ_{melt}	[kg/m^3]	1000	6940	2375	8020	6980	2650
thermal conductivity λ_{melt}	[W/mK]	0,6	28	95	155	35	1,2
heat capacity $c_{p,melt}$	[J/kgK]	4180	240	1300	550	834	840
surface tension σ	[N/m]	0,072	0,5	0,9	1,34	1,87	0,46
dynamic viscosity η_{melt}	[Pas]	0,00089	0,0015	0,0013	0,004	0,0055	***
kinematic viscosity ν_{melt}	[m^2/s]	8,90E-07	2,16E-07	5,47E-07	4,99E-07	7,88E-07	***

* composition of this slag: CaO 50%, SiO_2 40%, Al_2O_3 10%

** softening temperature

*** slag viscosity:

T_{slag} [°C]	η_{melt} [Pas]	ν_{melt} [m^2/s]
1400	0,9	0,000340
1500	0,4	0,000151
1800	0,1	0,000038